JM PERSPECTIVES

The Cahn–Hilliard–Navier–Stokes framework for multiphase fluid flows: laminar, turbulent and active

Nadia Bihari Padhan[1,2] and Rahul Pandit[1] (ORCID)

[1]Centre for Condensed Matter Theory, Department of Physics, Indian Institute of Science, Bangalore, India

[2]Institute of Scientific Computing, TU Dresden, 01069 Dresden, Germany

Corresponding author: Rahul Pandit, rahul@iisc.ac.in

The Cahn–Hilliard–Navier–Stokes (CHNS) partial differential equations (PDEs) provide a powerful framework for the study of the statistical mechanics and fluid dynamics of multiphase fluids. We provide an introduction to the equilibrium and non-equilibrium statistical mechanics of systems in which coexisting phases, distinguished from each other by scalar order parameters, are separated by an interface. We then introduce the coupled CHNS PDEs for two immiscible fluids and generalisations for (i) coexisting phases with different viscosities, (ii) CHNS with gravity, (iii) three-component fluids and (iv) the CHNS for active fluids. We discuss mathematical issues of the regularity of solutions of the CHNS PDEs. Finally we provide a survey of the rich variety of results that have been obtained by numerical studies of CHNS-type PDEs for diverse systems, including bubbles in turbulent flows, antibubbles, droplet and liquid-lens mergers, turbulence in the active-CHNS model and its generalisation that can lead to a self-propelled droplet.

Key words: active matter, breakup/coalescence, multiphase flow

1. Introduction

Multiphase flows (see, e.g., Brennen 2005; Prosperetti & Tryggvason 2007; Balachandar & Eaton 2010) abound in nature. They occur on astrophysical, atmospheric, industrial, laboratory and cellular scales. Examples include the circumgalactic medium (Sharma *et al.* 2012; Faucher-Giguere & Oh 2023), clouds (see, e.g., Shaw 2003; Bodenschatz *et al.* 2010; Devenish *et al.* 2012), flows with droplets and bubbles (see, e.g., Johnson & Sadhal 1985; Stone 1994; Magnaudet & Eames 2000; Mercado *et al.* 2010; Anna 2016; Magnaudet & Mercier 2020; Mathai, Lohse & Sun 2020; Pandey, Ramadugu & Perlekar 2020;

Pal *et al.* 2022; Pandey, Mitra & Perlekar 2023), aerosols that transmit pathogens (see, e.g., Bourouiba 2021) and biomolecular condensates (see, e.g., Banani *et al.* 2017; Gouveia *et al.* 2022). An examination of these examples reveals that the term multiphase is used to mean different things in different settings. For example, the important overview by Balachandar & Eaton (2010) begins by noting the following: '. . . Dispersed multiphase flows are distinguished from other kinds of multiphase flows, such as free-surface flows. In dispersed multiphase flows, the evolution of the interface between the phases is considered of secondary importance. Processes such as droplet or bubble breakup and agglomeration do indeed alter the interface between the phases. However, in the context of dispersed multiphase flows, one accounts for the interface between the dispersed and carrier phases in terms of particle-size spectra without considering the detailed evolution of the interface.' In contrast, we restrict ourselves to systems in which the different phases coexist in thermodynamic equilibrium and where it is necessary to account for the surface tension and the breakup or coalescence of droplets of these phases. To understand such multiphase flows, we must combine theoretical methods from fluid dynamics and statistical mechanics.

The fundamental equations governing the dynamics of a viscous fluid, now known as the Navier–Stokes (NS) equations, were first introduced by Navier in 1822 (Navier 1823). Over the following decades, these equations were refined and rigorously formulated by Stokes and others (Stokes 1901; Leray 1934; Batchelor 1967; Doering & Gibbon 1995; Galdi 2000; Foias *et al.* 2001; Robinson 2020; Farwig 2021), leading to the modern form used today. For a detailed historical developments of this equation, see Darrigol (2005) and Bistafa (2018). The Cahn–Hilliard (CH) equation, which is 67 years old (see, e.g., Cahn & Hilliard 1958, 1959; Cahn 1961; Lifshitz & Slyozov 1961; Lothe & Pound 1962; Hohenberg & Halperin 1977; Gunton, San Miguel & Sahni 1983; Chaikin, Lubensky & Witten 1995; Bray 2002; Onuki 2002; Badalassi, Ceniceros & Banerjee 2003; Berti *et al.* 2005; Puri & Wadhawan 2009; Perlekar *et al.* 2014), plays a central role in the theory of two-phase mixtures, interfaces, phase separation, domain growth and coarsening in the wake of a quench from a high-temperature single-phase regime to a low-temperature two-phase region (Bray 2002; Puri 2004). The CH equation, initially formulated to describe phase separation in binary alloys (see, e.g., Lebowitz & Kalos 1976; Binder *et al.* 1979; Puri & Wadhawan 2009), has been applied, with suitable adaptations, to a wide range of phenomena, including self-assembly in diblock copolymers (Hill & Millett 2017) and tumour-growth modelling (Hilhorst *et al.* 2015; Ebenbeck, Garcke & Nürnberg 2020; Garcke, Lam & Signori 2021). For a comprehensive review of the applications of the CH equation, see Kim *et al.* (2016). If the two phases under consideration are immiscible fluids, it is natural to combine the above two equations to obtain the Cahn–Hilliard–Navier–Stokes (CHNS) equations that provide a powerful mathematical framework for the study of two-fluid flows, be they laminar or turbulent. The CHNS approach and its generalisations have (i) found extensive applications, across diverse length and time scales, e.g. in droplet formation in the atmosphere and the manipulation of microscale droplets in microfluidic devices, (ii) led to new insights into a variety of multiphase flows and (iii) provided a convenient and efficient numerical scheme for direct numerical simulations (DNSs) of such flows. We provide on overview of this rich and rapidly developing field.

The CHNS framework, also known as the diffuse-interface or the phase-field method, is related to Model H that is used in dynamic critical phenomena (see, e.g., Hohenberg & Halperin 1977; Gurtin, Polignone & Vinals 1996; Anderson, McFadden & Wheeler 1998; Puri & Wadhawan 2009). It has a rich history that dates back to the pioneering studies of Fixman and of Kawasaki (see, e.g., Fixman 1967; Kawasaki 1970), who developed coupled
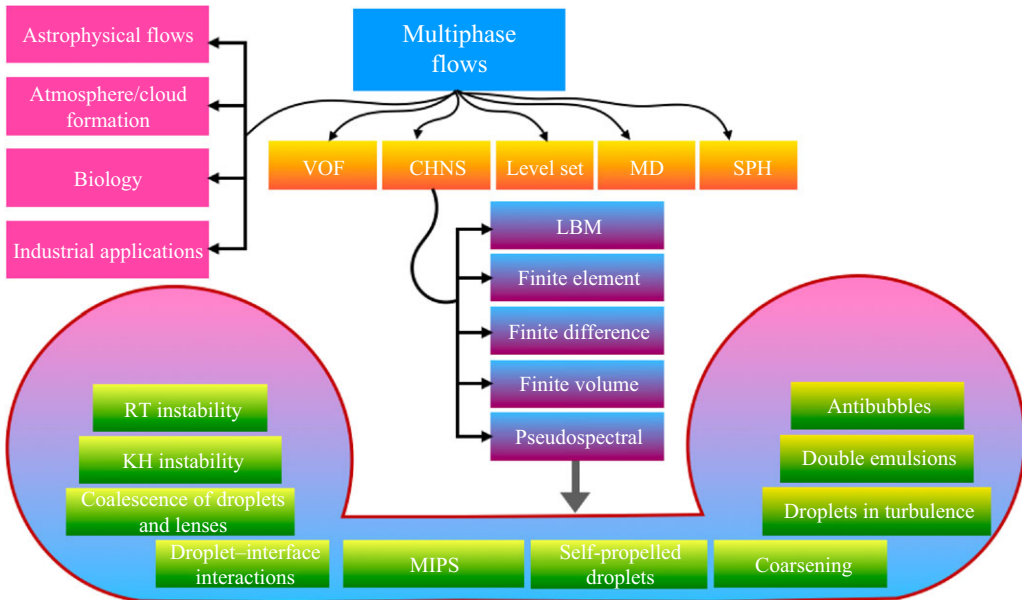
Figure 1. A schematic overview of multiphase flows, their wide-ranging applications, the mathematical and numerical models employed for studying them; we include the CHNS and phase-field models, various numerical methods that are used to solve the CHNS model, and the broad spectrum of applications of the CHNS model. Here, VOF, volume of fluids; MD, molecular dynamics; SPH, smoothed particles hydrodynamics; LBM, Lattice–Boltzmann method; RT, Rayleigh–Taylor; KH, Kelvin–Helmholtz; MIPS, motility-induced phase separation.

hydrodynamical equations for studying the behaviour of binary-fluid mixtures. Since then, the CHNS framework has evolved into a powerful tool for modelling a wide range of complex multiphase flows. It uses diffuse interfaces with a smooth transition region instead of a sharp boundary, so the CHNS model provides a convenient representation of the dynamics of fluid–fluid interfaces (see, e.g., Lowengrub, Rätz & Voigt 2009; Kim 2012). This approach enables us to study a variety of phenomena, including droplet formation, coalescence and breakup, as well as phase separation and mixing. In figure 1, we present a schematic overview of multiphase flows, their wide-ranging applications, and the mathematical and numerical models employed for studying these systems. This diagram includes the CHNS or phase-field model, various numerical methods that are used to solve the CHNS partial differential equations (PDEs), and the broad spectrum of applications of the CHNS model. Below, we briefly outline the key differences and advantages of the CHNS method in comparison with other approaches.

(i) Molecular dynamics – MD provides a microscopic perspective on and treatment of phase separation and interfacial dynamics (see, e.g., Singh & Puri 2015*a*; Li 2023); MD becomes computationally costly and challenging when dealing with large interfacial fluctuations and turbulence in macroscopic multiphase systems. Although MD has been used successfully for studying problems like droplet coalescence, it lacks the ability to model large-scale hydrodynamic effects efficiently. See Heinen *et al.* (2022) for a comparative study of MD and phase-field simulations for problems related to the coalescence of droplets.

(ii) Volume of fluid – VOF is a widely used numerical technique for tracking and locating free surfaces in multiphase flows (see, e.g., Lafaurie *et al.* 1994;

Popinet & Zaleski 1999; Yokoi 2007; Tryggvason, Scardovelli & Zaleski 2011; Mohan & Tomar 2024). It is particularly effective for simulating fluid flows with interfaces between different fluids. The VOF models the interface as a sharp boundary, which can introduce numerical challenges when handling complex topological changes. However, in reality, interfaces are not infinitely sharp, but they have a finite thickness, especially in systems undergoing phase separation. In contrast, the phase-field (i.e. CHNS) framework represents the interface as a diffuse region rather than a sharp boundary. This approach naturally accommodates topological changes, such as droplet coalescence or breakup, without requiring complex interface-tracking algorithms. Both methods have been successfully applied in the study of antibubble dynamics by Pal *et al.* (2022). A comprehensive comparison of these methods for various multiphase flows can be found in Mirjalili, Ivey & Mani (2019).

(iii) Smoothed particle hydrodynamics – SPH is a mesh-free, particle-based method that is well-suited for simulating free-surface flows and multiphase interactions (see, e.g., Colagrossi & Landrini 2003; Violeau & Rogers 2016; Wang *et al.* 2016; Díaz-Damacillo *et al.* 2023). The SPH is well-suited for studies of certain types of free-surface flows, but it can be computationally intensive because it requires the tracking of individual particles and, in some cases, stabilisation techniques. The SPH typically uses additional formulations to capture, accurately, interfacial dynamics, such as surface tension (see Jeske *et al.* 2023).

(iv) Level-set method – this represents interfaces as sharp boundaries using a level-set function. This approach is effective for tracking evolving interfaces, particularly in cases where the topology changes, such as in droplet merging and splitting (see, e.g., Sethian & Smereka 2003; Yuan *et al.* 2018; Valle, Trias & Castro 2020). A detailed comparative study via numerical simulations of both level-set and phase-field methods is given in Zhu *et al.* (2021), where the authors write '. . . In the rising process of the bubble, the tracking efficiency of the phase field method is higher than that of the level-set method. The phase field method is easier to capture the subtle changes of the bubble, and has higher calculation efficiency and accuracy, and has better simulated calculation results.'

The remaining part of this paper is organised as follows. In §2 we begin with a discussion of the statistical mechanics of systems in which two coexisting phases, distinguished from each other by a scalar order parameter ϕ, are separated by an interface. Our discussion leads naturally to the time-dependent Ginzburg–Landau (TDGL) PDE, when ϕ is not conserved, and the CH PDE, if ϕ is conserved. In §3 we define the models that we use when the coexisting phases are fluids; in the simple case of two immiscible fluids we have the CHNS equations; we give its generalisations for (i) coexisting phases with different viscosities, (ii) CHNS with gravity, (iii) three-component fluids (CHNS3) and (iv) CHNS for active fluids. Section 4 gives an overview of the numerical schemes that are used to study these models; we include details of pseudospectral DNSs and the volume-penalisation method that we use in our work; furthermore, we contrast the CHNS diffuse-interface approach with schemes that track the spatiotemporal evolution of sharp interfaces. Section 5 discusses mathematical issues of the regularity of solutions of the CHNS PDEs. Section 6 contains a survey of the types of results that have been obtained by numerical studies of CHNS-type PDEs. In §7 we present results for a variety of challenging problems for which we have to go beyond the binary-fluid CHNS. Section 8 summarises the CHNS framework for multiphase flows and discusses and new challenges in this area.

2. Overview: statistical mechanics of interfaces

This section contains a short outline of the statistical mechanics of systems with interfaces. We include material that is required for the development of CH models and their generalisations. Section 2.1 is devoted to the equilibrium statistical mechanics of systems with interfaces; in particular, it uses the Ising and lattice-gas models to explore interfacial statistical mechanics. In § 2.2 we turn to a discussion of time-dependent phenomena, especially in the context of the kinetic Ising model. This leads naturally to the discussion, in § 2.2.1, of TDGL theory, for a non-conserved order parameters, and, in § 2.2.2, the CH equation for a conserved order parameter.

2.1. *Equilibrium statistical mechanics*

Interfaces separate coexisting phases. In equilibrium, all thermodynamic properties of interfaces follow from the intensive interfacial free energy f_I, which is precisely the interfacial tension $\sigma_{\alpha,\beta}$ between coexisting bulk phases α and β. For pedagogical reasons, we illustrate this by considering the ferromagnetic, spin-half, Ising model, which is used to model magnets that are anisotropic (in spin space). This Ising model, which can be mapped onto a simple lattice-gas model for a fluid that can have two coexisting bulk phases (see below), has the Hamiltonian

$$\mathcal{H} = -J \sum_{\langle i,j \rangle} S_i S_j - h \sum_i S_i. \tag{2.1}$$

The spins $S_i = \pm 1$ occupy the $N \sim L^d$ sites i of a d-dimensional hypercubic lattice, with side L, in a region Ω; the exchange interaction J couples spins on nearest-neighbour pairs of sites $\langle i,j \rangle$; a ferromagnetic interaction ($J > 0$) favours spin alignment, i.e. spins of the same sign on nearest-neighbour sites; the external magnetic field h favours $S_i = sgn(h)$ and it distinguishes between the two phases: up-spin $\uparrow$ (with $S_i = +1$, $\forall i$, at zero temperature $T = 0$) and down-spin $\downarrow$ (with $S_i = -1$, $\forall i$, at $T = 0$). If we are interested only in bulk statistical physics, it is convenient to use periodic boundary conditions (PBCs) in all d directions.

The transformation $n_i = (1 + S_i)/2$, yields the lattice gas variables $n_i = 0$ or 1 and defines the lattice-gas model, whose low- and high-density phases are the analogues of the $\downarrow$ and $\uparrow$ phases in the ferromagnetic Ising model and in which the chemical potential is the counterpart of h in the Ising model (see, e.g., Griffiths 1972; Goldenfeld 2018). (A similar transformation relates the Ising-model Hamiltonian to a lattice model for a binary alloy.) Just as a positive (negative) external field h favours the up-spin $\uparrow$ (down-spin $\downarrow$) phase, a large and positive (negative) values of the chemical potential favour the high-density (low-density) phase in the lattice-gas model (see table 1).

The intensive bulk free energy f_B of the Ising model, which is a function of the temperature T, h and J, is defined as follows:

$$f_B(T, h, J) = \lim_{N \to \infty} \frac{1}{N} \left[F(T, h, J, \Omega) \right];$$
$$F(T, h, J, \Omega)] = -k_B T \ln[\mathcal{Z}];$$
$$\mathcal{Z} = \sum_{\{S_i = \pm 1\}} \exp[-\mathcal{H}/(k_B T)]; \tag{2.2}$$

where, k_B, F and $\mathcal{Z}$ are, respectively, the Boltzmann constant, the total free energy and the partition function and the sum is over all the spin states. Note that F depends on Ω

System	↑ Phase	↓ Phase	Phase Transition
Ising ferromagnet	Ferromagnetic up	Ferromagnetic down	Spin flip
Liquid–gas	High-density (liquid)	Low-density (gas)	Condensation
Binary (A–B) mixture	A-rich	B-rich	Phase-separation
Active fluid	High-density	Low-density	Active phase-separation

Table 1. Correspondences between Ising ferromagnetic systems, with lattice-gas or binary-mixture counterparts, and their phases and phase transitions; here, ↑ and ↓ represent the up-spin and down-spin phases of an Ising ferromagnet (see the text). Rows 2–4 mention equilibrium phases and transitions; the last row mentions non-equilibrium active fluids which can exhibit active phase-separation (see § 7.6).

and, therefore, on BCs; by contrast, f_B does not depend on Ω, the BCs, and boundary couplings and fields because we have taken the thermodynamic limit $N \to \infty$. If the thermodynamic limit exists (as it does for the Ising model we consider), then: (i) f_B is a convex-up function of its arguments, which guarantees continuity of f_B with respect to T, h and J; (ii) $\partial f_B / \partial T$, $\partial f_B / \partial h$ and $\partial f / \partial J$ exist almost everywhere (f_B has slope discontinuities at first-order phase boundaries); and (iii) $\partial f_B / \partial T$, $\partial f_B / \partial h$ and $\partial f / \partial J$ are, respectively, monotone, non-increasing functions of T, h and J. Bulk thermodynamic functions follow from derivatives of f_B; e.g. the magnetisation per site

$$M = \sum_i \langle S_i \rangle / N = -\partial f_B / \partial h, \tag{2.3}$$

where the angular brackets denote the thermal average. When the second derivatives of f_B exist, they lead to stability conditions such as the positivity of the specific heat at constant h, to wit, $C_h \equiv -k_B T \partial^2 f_B / \partial T^2 \geqslant 0$.

This magnetisation $M \in [-1, 1]$ is the order parameter, which is positive (negative) in the up-spin (down-spin) phase; its lattice-gas counterpart is the density $\rho = \sum_i \langle n_i \rangle / N \in [0, 1]$. For dimension $d > 1$, the Ising-model phase diagram in the $h/J - k_B T/J$ plane (henceforth, we set $k_B = 1$ and $J = 1$) shows a first-order phase boundary, $h = 0$ for $T < T_c$, where T_c is the critical or Curie temperature at which this model exhibits a continuous phase transition from the ferromagnetic to the paramagnetic phase (figure 2a). Along the first-order boundary, the ↑ and ↓ phases coexist. In the $T-M$ counterpart (figure 2b) of the $h-T$ phase diagram, two-phase coexistence occurs everywhere below the coexistence curve in the peach-shaded region: the system undergoes macroscopic phase separation, forming distinct ↑ and ↓ phases, rather than a fully mixed state; in equilibrium, these coexisting phases are separated by an interface (see below). If we use the Ising-model–lattice-gas correspondence (table 1), we see that its binary-mixture counterpart is the coexistence of immiscible fluids, below the critical temperature above which the two fluids mix.

We do not concentrate on the critical properties of the Ising model here; but we do mention critical-point behaviours occasionally. Therefore, we note that, in the vicinity of the critical point at $h = 0$ and $T = T_c$, thermodynamic functions display power-law forms, with universal exponents and scaling functions (see, e.g., Chaikin *et al.* 1995; Kardar 2007; Goldenfeld 2018). For example, at $h = 0$ and $(T - T_c)/T_C \ll 1$, $M \sim [(T_c - T)/T_c]^\beta$, for $T \lesssim T_c$; and the specific heat $C_h \sim [(T_c - T)/T_c]^{-\alpha}$ diverges; β and α are universal critical exponents that depend on d and the number of components n of the order parameter (for the Ising model we have a scalar order parameter and $n = 1$). If we were to obtain order-parameter correlation functions and, therefrom, the correlation length ξ, then we would find the divergence $\xi \sim [(T_c - T)/T_c]^{-\nu}$. At such a critical point,
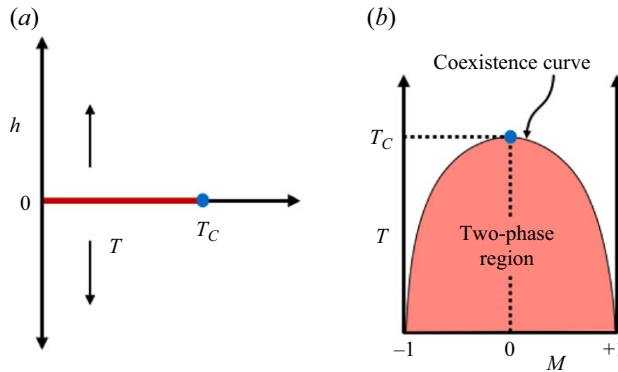
Figure 2. Schematic phase diagrams for the d-dimensional Ising model (2.1) in the magnetic-field h and temperature T plane (*a*) and the T and magnetisation M plane (*b*). There is a first-order phase boundary (brown line), $h = 0$ for $T < T_c$, that ends in a critical point at $h = 0$, $T = T_c$ (blue point); along the first-order boundary, the $\uparrow$ and $\downarrow$ phases coexist. In the $T-M$ phase diagram, two-phase coexistence occurs in the peach-shaded region everywhere below the coexistence curve (black), atop which is the critical point.

only two exponents are independent; the others can be related by scaling laws that are linear relations between these exponents (see, e.g., Chaikin *et al.* 1995; Kardar 2007; Goldenfeld 2018). For the $d = 2$ Ising model, $\alpha = 0$ because C_h has a logarithmic divergence at $h = 0$ and $T = T_c$, $\beta = 1/8$, and $\nu = 1$.

To define the intensive interfacial free energy f_I (per unit area of the interface), we must distinguish between BCs, for the Ising Hamiltonian (2.1), that yield a $(d-1)-$dimensional interface between coexisting bulk phases and those that do not. We illustrate two such BCs, $++$ and $-+$, via the schematic diagrams for $d = 2$ in figure 3. We use periodic BCs in $(d-1)$ directions; in the remaining direction, denoted by x, we have two $(d-1)$-dimensional surfaces at $x = -L/2$ and $x = +L/2$; the $++$ BC does not yield an interface; by contrast, the $-+$ BC yields an interface with $N_I \sim L^{(d-1)}$ the number of sites in the $T = 0$ interface. (The precise value of x at the interface location depends on whether we work in the fixed-h or fixed-M ensemble; in the former, the interface can lie anywhere between $x = -L/2$ and $x = +L/2$, whereas, in the latter, the position of the interface is such that the proportion of the $\uparrow$ and $\downarrow$ regions yields the fixed magnetisation M.) Here,

$$f_I(T, h, J) = \lim_{N_I \to \infty; N \to \infty} \frac{1}{N_I} \left[F^{-+} - F^{++} \right], \tag{2.4}$$

where F^{++} and F^{-+} are, respectively, the total free energies of the Ising model with $++$ and $+-$ BCs (figure 3). (Note that the free-energy contributions from the two surfaces cancel when we subtract F^{++} from F^{-+} in (2.4).) We have mentioned above that bulk statistical mechanics and phase diagrams follows from f_B and its derivatives; similarly, interfacial statistical mechanics and interfacial phase diagrams follow from f_I and its derivatives. If the order parameter has more than one component, e.g. if $n = 2$ as in the XY model or a superfluid, then f_I has to be replaced by the helicity modulus Υ, because the interface is not sharp (see, e.g., Fisher, Barber & Jasnow 1973); in such cases, $-+$ BCs lead to a correction to the total free energy that scales as $L^{(d-2)}$. We restrict ourselves to scalar order parameters that have $n = 1$. Furthermore, f_I gives us the strict definition of the interfacial (or surface) tension (see, e.g., Rottman & Wortis 1984). Both f_I and surface tension have the same physical units: f_I is typically given in energy per unit area, whereas the surface tension is specified as a force per unit length, both of which are dimensionally equivalent. In particular, if $T \to T_c$ from below, the coexisting phases
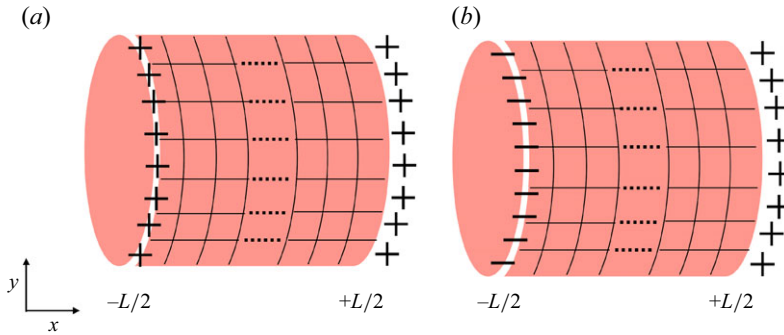
Figure 3. Schematic diagrams for (*a*) $++$ and (*b*) $-+$ BCs for the *d*-dimensional Ising model (2.1); $d = 2$ in this illustration. In $d - 1$ directions (*y* here) we use periodic BCs.

come together at the critical point (the consolute point in a binary-fluid mixture) and the interfacial free energy vanishes as $f_I \sim [(T_c - T)/T_c]^\mu$, with the exponent $\mu = 2\nu$.

It is important to distinguish between surface and interfacial free energies. The former is associated with a geometrically imposed surface (say on the $(1,0,0, \ldots)$ face of the hypercubic lattice we consider). The intensive surface free energy is (see, e.g., Fisher & Caginalp 1977; Caginalp & Fisher 1979; Rottman & Wortis 1984)

$$f_s(T, h, J) = \lim_{N_s \to \infty; N \to \infty} \frac{1}{2N_s} \left[F^{++} - N f_B \right], \tag{2.5}$$

where $N_s \sim L^{(d-1)}$ is the number of sites in the geometrically imposed surface (or surfaces); for the $++$ BC in figure 3, there are two surfaces at $x = -L/2$ and $x = +L/2$, so we have a factor of 2 in (2.5). Geometrically imposed surfaces do not fluctuate, but interfaces do, because of thermal or other (e.g. turbulent) fluctuations.

It is well known that the *d*-dimensional Ising model can be solved exactly (i.e. f_B can be obtained analytically) only if (i) $d = 1$ or (i) $d = 2$ and $h = 0$ (see, e.g., Onsager 1944; Huang 2008; Thompson 2015; Baxter 2016). In other dimensions, we must either use approximations, such as mean-field theory, or numerical simulations, such as the Monte Carlo method (see, e.g., Plischke & Bergersen 1994; Chaikin *et al.* 1995; Gould *et al.* 1996; Kardar 2007; Goldenfeld 2018). For $d = 2$, a variety of elegant results can be obtained for f_I; these are of relevance to equilibrium crystal shapes (see Rottman & Wortis 1984).

We give a brief introduction to mean-field theory because it leads directly to our discussion of the CH system. We consider a generalisation of the Hamiltonian (2.1) in which the magnetic field h is replaced by a site-dependent magnetic field h_i, so the second term becomes $\sum_i h_i S_i$. In its most rudimentary form, mean-field theory (known as Curie–Weiss theory for our Ising-model example) uses

$$S_i S_j = (S_i - \langle S_i \rangle)(S_j - \langle S_j \rangle) + S_i \langle S_j \rangle + S_i \langle S_j \rangle - \langle S_i \rangle \langle S_j \rangle;$$
$$S_i S_j \simeq + S_i \langle S_j \rangle + S_i \langle S_j \rangle - \langle S_i \rangle \langle S_j \rangle. \tag{2.6}$$

The second equation follows from the first one if we neglect $(S_i - \langle S_i \rangle)(S_j - \langle S_j \rangle)$ because it is quadratic in deviations from the equilibrium values of the site magnetisations $M_i \equiv \langle S_i \rangle$. We now substitute the second row of (2.6) into the Hamiltonian (2.1); this yields a mean-field Hamiltonian H_{MF} in which a spin at site i experiences an effective magnetic field $h_i^{eff} = h_i + J \sum_{j \in [nni]} M_j$, where $[nni]$ indicates all the nearest-neighbour sites of i. The single-site magnetisation for $\mathcal{H}_{MF}$ follows simply and we get the Curie–Weiss self-consistency equations

$$M_i = \tanh\left[\frac{(h_i + J\sum_{j\in[nni]} M_j)}{(k_B T)}\right], \tag{2.7}$$

which can have many solutions. The variational formulation of this mean-field theory (see, e.g., Falk 1970; Girardeau & Mazo 1973; Plischke & Bergersen 1994) implies that we must select the solution that leads to the global minimum of the variational free energy

$$\mathcal{F}_{CW}(\{\mathcal{M}_i\}) = -\sum_i h_i \mathcal{M}_i - J\sum_{<i,j>}(\mathcal{M}_i \mathcal{M}_j)$$
$$+ \frac{k_B T}{2}\sum_i\left[(1+\mathcal{M}_i)\ln\frac{(1+\mathcal{M}_i)}{2} + (1-\mathcal{M}_i)\ln\frac{(1-\mathcal{M}_i)}{2}\right], \tag{2.8}$$

where $\mathcal{M}_i$ are the variational parameters and the subscript CW stands for Curie–Weiss. Note that $\mathcal{F}(\{\mathcal{M}_i\})$ is not the equilibrium free energy, so it might not be a convex function of its arguments. If we minimise $\mathcal{F}(\{\mathcal{M}_i\})$ by setting $\partial\mathcal{F}(\{\mathcal{M}_i\})/\partial\mathcal{M}_i = 0$, we recover the self-consistency equations (2.7). At the global minimum of $\mathcal{F}(\{\mathcal{M}_i\})$, the equilibrium value of $\mathcal{M}_i$ is $\mathcal{M}_{i,eq}$; when we substitute this value of $\mathcal{M}_i$ in $\mathcal{F}(\{\mathcal{M}_i\})$, we obtain the mean-field expression for the equilibrium free energy, which satisfies all the convexity properties mentioned earlier.

If the variational parameters $\mathcal{M}_i$ vary slowly in space, say over a length scale ℓ, with $a/\ell \ll 1$, where a is the lattice spacing of the hypercubic lattice, then we can make the following continuum approximation:

$$\mathcal{M}_i \to \phi(\mathbf{r}); \quad h_i \to h(\mathbf{r}); \quad \sum_i \to \frac{1}{a^d}\int d\mathbf{r};$$
$$-J\sum_{<i,j>}(\mathcal{M}_i\mathcal{M}_j) \to \left[-\frac{qJ}{2a^d}\int d\mathbf{r}[\phi(\mathbf{r})]^2 + \frac{J}{2a^{(d-2)}}\int d\mathbf{r}[\nabla\phi(\mathbf{r})]^2\right]$$
$$+ O((a/\ell)^4), \tag{2.9}$$

where $q = 2d$ is the nearest-neighbour coordination number for the d-dimensional hypercubic lattice and ϕ is a scalar order parameter. We now use (2.9) to obtain the continuum limit of the variational free energy functional (2.8),

$$a^d\mathcal{F}_{CW}(\phi, \nabla\phi) = \int d\mathbf{r}\left[-h(\mathbf{r})\phi(\mathbf{r}) - \frac{qJ}{2}[\phi(\mathbf{r})]^2 + \frac{Ja^2}{2}[\nabla\phi(\mathbf{r})]^2 + \frac{k_B T}{2}V_{CW}(\phi)\right],$$
$$V_{CW}(\phi) \equiv \left[(1+\phi)\ln\frac{(1+\phi)}{2} + (1-\phi)\ln\frac{(1-\phi)}{2}\right], \tag{2.10}$$

where, in the Curie–Weiss approximation, the first three terms in (2.10) yield the energy contribution and the fourth term the entropy contribution (see, e.g., Puri 2004); furthermore, $\phi \in [-1, 1]$.

If we expand $V_{CW}(\phi)$ to $O(\phi^4)$ and set $a = 1$, we obtain the Landau–Ginzburg (LG) variational free-energy functional (see, e.g., Kadanoff *et al.* 1967; Chaikin *et al.* 1995; Kardar 2007; Landau & Lifshitz 2013; Goldenfeld 2018),

$$\mathcal{F}_{LG}(\phi, \nabla\phi) = \int d\mathbf{r}\left[g(\phi) + \frac{\sigma}{2}[\nabla\phi]^2\right],$$
$$g(\phi) \equiv \left[-h\phi + \frac{k_B}{2}(T - T_c^{CW})\phi^2 + \frac{k_B T}{12}\phi^4 + O(\phi^6)\right], \tag{2.11}$$
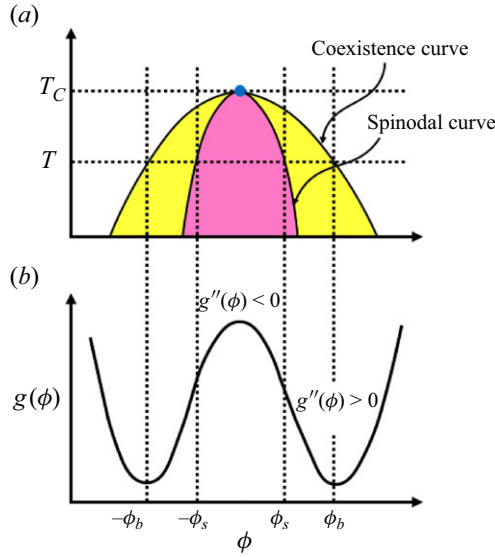
Figure 4. Schematic plots of (*a*) the variational free energy $g(\phi)$ (see (2.11)) versus the order parameter ϕ, for magnetic field $h = 0$ and temperature $T < T_c$, with two equally deep minima at $\phi = \pm\phi_b$, the LG equilibrium values; (*b*) the LG phase diagram in the $T - \phi$ plane showing the coexistence curve (also called the binodal), below which the phases coexist, and the spinodal curve, which is the locus of points at which $d^2g(\phi)/d\phi^2 = 0$.

where we suppress the **r** argument of h and ϕ, the Curie–Weiss critical temperature $T_c^{CW} \equiv qJ$, and $\sigma \equiv J$ is the bare surface-tension cost for large gradients in the scalar-order-parameter field ϕ. If we consider uniform ordering, then minimisation of g via $\partial g(\phi)/\partial \phi = 0$ yields the mean-field-theory phases, transitions, and exponents for this Ising model. We present a schematic plot of $g(\phi)$ in figure 4(*a*) for $T < T_c^{CW}$ and $h = 0$. Note that g displays two, equally deep quadratic minima at

$$\phi_b \equiv \sqrt{\frac{3(T_c^{CW} - T)}{T}} \quad \text{and} \quad -\phi_b, \tag{2.12}$$

so the $\uparrow$ and $\downarrow$ phases coexist along the first-order phase boundary $h = 0$, $0 \leqslant T < T_c^{CW}$, whose counterpart in the $T - \phi$ phase is the coexistence curve shown in figure 4(*b*). If $T \to T_c^{CW}$ from below, with $h = 0$, these minima merge at $T = T_c^{CW}$, the coefficient of the quadratic term vanishes and elementary steps yield the mean-field order-parameter exponent $\beta_{MF} = 1/2$ and interfacial-free-energy exponent $\mu_{MF} = 2\nu_{MF} = 1$. The interfacial free energy vanishes for $T > T_c$, for there are no coexisting phases and, therefore, no interface; and $g(\phi)$ has only one quadratic minimum if $T > T_c^{CW}$ and $h = 0$.

To study non-uniform order-parameter configurations (see, e.g., Pandit & Wortis 1982; Bray 2002; Puri 2004; Puri & Wadhawan 2009), we must minimise $\mathcal{F}_{CW}$ or $\mathcal{F}_{LG}$. We illustrate this for $\mathcal{F}_{LG}$ below by considering BCs (cf. figure 3) that yield an interface for $T < T_c^{CW}$ and $h = 0$:

$$\delta\mathcal{F}_{LG}/\delta\phi = 0;$$
$$\Rightarrow \left[-\sigma\nabla^2\phi + k_B(T - T_c^{CW})\phi + \frac{k_BT}{3}\phi^3 \right] = h(\mathbf{r}). \tag{2.13}$$

If we assume that ϕ varies only in the x direction and that $h(\mathbf{r}) = 0$, we obtain the following ordinary differential equation, which must be solved with the BCs given in the second row:

$$\sigma \, d^2\phi/dx^2 = k_B(T - T_c^{CW})\phi + \frac{k_B T}{3}\phi^3;$$
$$\text{BCs} \quad \phi(x) = \pm\phi_b \quad \text{at} \quad x = \pm\infty. \tag{2.14}$$

This has the following well-known solution (see, e.g., Pandit & Wortis 1982; Puri 2004; Puri & Wadhawan 2009):

$$\phi(x) = \phi_b \tanh\left[(x - x_0)/\xi_{MF}\right];$$
$$\xi_{MF} = \sqrt{\frac{\sigma}{2k_B(T_c^{CW} - T)}}; \tag{2.15}$$

here, x_0 is the point at which this interfacial (or kink) profile goes through zero and ξ is the width of the interface. If we portray the solutions of (2.14) in the phase space $[d\phi/dx, \phi]$, the bulk phases correspond to hyperbolic fixed points at $d\phi/dx = 0$, $\phi = \pm\phi_b$ and the interfacial profile is a heteroclinic trajectory that goes from one of these fixed points to the other (see Pandit & Wortis 1982). The mean-field free energy $f_{I,MF}$ (surface tension) for the kink solution follows by subtracting $\mathcal{F}_{LG}$ without an interface from its value with an interface,

$$L^{(d-1)} f_{I,MF}(\phi, \nabla\phi) = \int_{-\infty}^{\infty} dx \left[\Delta g(\phi) + \frac{\sigma}{2}[d\phi/dx]^2 \right],$$
$$\Delta g(\phi) \equiv \left[\frac{k_B}{2}(T - T_c^{CW})[\phi^2 - \phi_b^2] + \frac{k_B T}{12}[\phi^4 - \phi_b^4] \right]. \tag{2.16}$$

If we multiply the first equation in (2.13) by $d\phi/dx$ and integrate, we obtain (see, e.g., Puri & Wadhawan 2009) for details)

$$\frac{k_B}{2}\phi^2 + \frac{k_B}{12}\phi^4 + \frac{\sigma}{2}[d\phi/dx]^2 = \frac{k_B}{2}(T_c^{CW} - T)\phi_b^2 + \frac{k_B}{12}\phi_b^4,$$
$$\text{whence} \quad f_{I,MF} = \int_{-\infty}^{\infty} dx [d\phi/dx]^2. \tag{2.17}$$

Note that as T approaches T_c^{CW} from below, $\phi_b \to 0$, so $f_{I,MF}$ vanishes as $\sim (T_c^{CW} - T)^{\mu_{MF}}$, with $\mu_{MF} = 2\nu_{MF} = 1$, where ν_{MF} is the exponent that characterises the divergence of ξ_{MF} (see (2.15)). To go beyond this mean-field treatment, we must include the thermal fluctuations that are neglected by mean-field theory and which modify the mean-field values of critical exponents for $d \leqslant 4$ (see, e.g., Plischke & Bergersen 1994; Chaikin *et al.* 1995; Amit & Martin-Mayor 2005; Kardar 2007; Goldenfeld 2018; Ma 2018; Zinn-Justin 2021).

In most of this paper, we concentrate on physical parameter ranges in which systems are far from critical points. Therefore, we continue to use the LG framework outlined above and PDEs such as (2.13) with no noise terms that account for thermal fluctuations. If turbulence is present in the flows we consider, then turbulent fluctuations overpower thermal fluctuations; the latter are normally not required in studies of turbulent flows. For studies that suggest the inclusion of thermal noise in dissipation-range fluid turbulence see Betchov (1977) and Bandak *et al.* (2022).

We can also use the above inhomogeneous mean-field theory for the following:
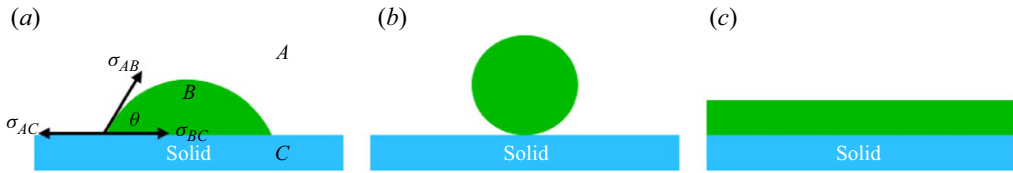
(*a*) (*b*) (*c*)

Figure 5. Schematic diagram of a droplet on a solid substrate for (*a*) partial wetting, (*b*) complete drying and (*c*) complete wetting. The white, green and blue regions indicate the three phases A, B and C (the last of which is a solid substrate); the surface tensions between the coexisting phases are σ_{AB}, σ_{AC} and σ_{BC}; the contact angle θ is given by the Young–Dupré equation $\sigma_{AC} = \sigma_{BC} + \sigma_{AB} \cos(\theta)$; in (*a*) $0 < \theta < \pi$, (*b*) $\theta = \pi$ and (*c*) $\theta = 0$.

(i) to study the wetting transition on an attractive substrate, which we illustrate by the schematic diagram in figure 5 (see, e.g., Cahn (1977), Pandit & Wortis (1982) and Pandit, Schick & Wortis (1982) for a detailed treatment of this problem);

(ii) to study curvature corrections to the surface tension (see Fisher & Wortis 1984 for details) at a curved interface; the dominant contribution at a curved interface yields Laplace's result (see, e.g., Fisher & Wortis 1984; Rowlinson & Widom 2013) for the pressure difference ΔP between the interior (say A) and exterior (say B) phases that are separated by a curved interface with surface tension σ_{AB} and radius of curvature R_{AB}:

$$\Delta P = \frac{2\sigma_{AB}}{R_{AB}}. \tag{2.18}$$

2.2. *Kinetic Ising models*

We turn now to a brief description of some time-dependent phenomena in multiphase systems. For pedagogical reasons, we have used the Ising model to illustrate various aspects of the equilibrium statistical mechanics of systems with interfaces. We adopt a similar strategy here by beginning with the kinetic Ising model (see, e.g., Kawasaki 1970; Puri 2004; Puri & Wadhawan 2009), employing a mean-field approximation, taking a continuum limit and obtaining, therefrom, TDGL descriptions for the spatiotemporal evolution of the order parameter in two cases, *viz.*, when it is (i) not conserved and (ii) conserved. Case (ii) yields the CH equation. Our discussion follows that of Puri & Wadhawan (2009), which the reader should consult for details.

The Ising-model Hamiltonian (2.1) contains only one component (say the z component in spin space), so it does not have intrinsic dynamics. We assume instead that the spins in this model are in contact with a heat bath (provided, e.g. by coupling to phonons in a crystalline solid) that leads to stochastic flipping of these spins. To study time-dependent phenomena we use, therefore, master equations for the conditional probability $P(\{S_i^0\}, 0; \{S_i\}, t)$ that the spin at site i is in the state S_i at time t, given that its $t = 0$ state was S_i^0; henceforth, for notational convenience, we suppress the arguments $\{S_i^0\}$, 0. (The braces indicate that we consider all the N spins in the $d-$dimensional hypercubic lattice). We give two such master equations:

(i) for the Glauber model (see Glauber (1963), indicated by the subscript G in (2.19)), in which the total magnetisation $\sum_i S_i$ is not conserved because we consider single-spin flips;

(ii) for the Kawasaki model (see Kawasaki 1966, 1970), indicated by the subscript K in (2.28), in which the total magnetisation is conserved because we consider exchanges of nearest-neighbour spins.

2.2.1. *Non-conserved order parameter: TDGL theory*

The master equation for the Glauber model is

$$\frac{dP_G(\{S_i\}, t)}{dt} = -\sum_{j=1}^{N} w_G(S_1, \ldots, S_j, \ldots, S_N | S_1, \ldots, -S_j, \ldots, S_N) P_G(\{S_i\}, t)$$
$$+ \sum_{j=1}^{N} w_G(S_1, \ldots, -S_j, \ldots, S_N | S_1, \ldots, S_j, \ldots, S_N) P_G(\{S_i'\}, t);$$
(2.19)

on the right-hand side the first and second terms arise, respectively, from the loss and gain of probability. The loss is associated with the spin flip $S_j \to -S_j$; the gain is because of the flip $S_j' \to -S_j'$, in a state $\{S_i'\}$ with $S_i' = S_i \ \forall \ i \neq j$ and $S_j' = -S_j$. The master equation (2.19) has the long-time ($t \to \infty$) equilibrium solution

$$P_{eq}(\{S_i\}) = \frac{1}{\mathcal{Z}} \exp\left[\frac{-\mathcal{H}}{k_B T}\right]$$
(2.20)

if the transition matrix $w_G(\{S_i\} | \{S_i'\})$ satisfies the condition of detailed balance (see, e.g., Van Kampen 1981; Martinelli 1999; Puri & Wadhawan 2009)

$$w_G(\{S_i\} | \{S_i'\}) P_{eq}(\{S_i\}) = w_G(\{S_i'\} | \{S_i\}) P_{eq}(\{S_i'\}).$$
(2.21)

This condition does not specify $w_G(\{S_i\} | \{S_i'\})$ completely; one convenient choice is the Suzuki–Kubo form (see, e.g., Suzuki & Kubo 1968; Puri & Wadhawan 2009)

$$w_G(\{S_i\} | \{S_i'\}) = \frac{1}{2\tau_G}\left[1 - \tanh\left(\frac{\Delta\mathcal{H}}{2k_B T}\right)\right],$$
(2.22)

where τ_G is the relaxation time scale and $\Delta\mathcal{H}$ is the change in the energy because of the spin flip. If we substitute (2.22) in the master equation (2.19) and then calculate the mean value of the magnetisation at site i,

$$\langle S_i \rangle = \sum_{\{S_j\}} S_i P_G(\{S_j\}, t),$$
(2.23)

standard calculations yield (see, e.g., Puri & Wadhawan 2009)

$$\tau_G \frac{d}{dt}\langle S_i \rangle = -\langle S_i \rangle + \left\langle \tanh\left[\frac{(h_i + J\sum_{j\in[nni]} S_j)}{(k_B T)}\right]\right\rangle.$$
(2.24)

This equation can be solved analytically only if $d = 1$ and $h_i = 0 \ \forall i$ (see, e.g., Glauber 1963; Siggia 1977; Pandit, Forgacs & Rujan 1981). For $d > 1$, we must either use approximations, such as mean-field theory, or finite-size calculations, numerical simulations or renormalisation groups (see, e.g., Pandit *et al.* 1981; Münkel 1993; Chaikin *et al.* 1995; Kardar 2007; Täuber 2013; Goldenfeld 2018; Ma 2018). We follow Puri & Wadhawan (2009) and use following the mean-field approach, which builds on the Curie–Weiss approximation (2.7) for the equilibrium magnetisation M_i. A direct expansion of the second term on the right-hand side of (2.29) yields moments, of all orders, of the spins S_i. In the mean-field dynamical model we use the approximation

$$\tau_G \frac{d}{dt}\langle S_i \rangle \simeq -\langle S_i \rangle + \tanh\left[\frac{(h_i + J\sum_{j\in[nni]}\langle S_j \rangle)}{(k_B T)}\right],$$
(2.25)

whose steady-state solution yields the Curie–Weiss self-consistency equation for the mean-field magnetisation given in (2.7). If we now take the continuum limit (2.9), we get

$$\tau_G \frac{\partial \phi}{\partial t} = -\frac{\delta \mathcal{F}_{CW}}{\delta \phi}, \tag{2.26}$$

and, if we make a small-ϕ expansion (valid, strictly speaking, near the Curie–Weiss critical point), we obtain the TDGL equation

$$\frac{\partial \phi}{\partial t} = -D \frac{\delta \mathcal{F}_{LG}}{\delta \phi}, \tag{2.27}$$

where we measure time in units of τ_G (so we set $\tau_G = 1$). The TDGL equation (2.27) is often postulated phenomenologically and its right-hand side includes a Gaussian white-noise term $\theta(\mathbf{r}, t)$ with zero-mean and a variance $2Dk_BT$ that satisfies the fluctuation-dissipation theorem; this is referred to as Model A in the critical-dynamics literature (see, e.g., Hohenberg & Halperin 1977; Puri & Wadhawan 2009; Täuber 2013; Ma 2018). This noise term plays an important role in the calculation of critical exponents, in general, and the dynamic critical exponent z, in particular, which characterises the critical-point divergence of the correlation time $\tau_c \sim \xi^z$. At the simplest mean-field level, Model A yields $z_{MF}^A = 2$.

2.2.2. *Conserved order parameter: CH theory*
The master equation for the Kawasaki model is (see Kawasaki 1966, 1970; Puri & Wadhawan 2009)

$$
\begin{aligned}
\frac{\mathrm{d}P_K(\{S_i\}, t)}{\mathrm{d}t} \\
= -\sum_{j=1}^N \sum_{k \in [nnj]} w_K(S_1, \ldots, S_j, S_k, \ldots, S_N | S_1, \ldots, S_k, S_j, \ldots, S_N) P_K(\{S_i\}, t) \\
+ \sum_{j=1}^N \sum_{k \in [nnj]} w_K(S_1, \ldots, S_k, S_j, \ldots, S_N | S_1, \ldots, S_j, S_k, \ldots, S_N) P_K(\{S_i'\}, t),
\end{aligned}
\tag{2.28}
$$

where the subscript K stands for Kawasaki, we set $h = 0$ in the Hamiltonian (2.1), and we work in the ensemble with fixed total magnetisation $M_{tot} = \sum_i S_i$. Note that (2.28) accounts for nearest-neighbour spin exchanges $S_j \leftrightarrow S_k$ that conserve M_{tot}. If we proceed as we did in the Glauber case, with the Suzuki–Kubo form (2.22) for the transition matrix w_K, we obtain (see, e.g., Puri & Wadhawan (2009) for details)

$$
\begin{aligned}
\tau_K \frac{\mathrm{d}}{\mathrm{d}t} \langle S_i \rangle = -2d\langle S_i \rangle + \sum_{j \in [nni]} \langle S_j \rangle \\
+ \sum_{k \in [nni]} \left\langle (1 - S_i S_k) \tanh\left[\frac{J\left(\sum_{j \in [nni; \neq k]} S_j - \sum_{j \in [nni; \neq i]} S_j\right)}{(k_BT)} \right] \right\rangle.
\end{aligned}
\tag{2.29}
$$

The dynamical analogue of the Curie–Weiss approximation, followed by a continuum approximation, and an expansion in powers of ϕ, yields the CH equation (see Cahn & Hilliard 1958, 1959; Cahn 1961; Puri & Wadhawan 2009)

$$\frac{\partial \phi}{\partial t} = D\nabla^2 \left[\frac{\delta \mathcal{F}_{LG}}{\delta \phi} \right], \tag{2.30}$$

where we set $\tau_K = 1$; note that $\int \mathrm{d}\mathbf{r}\phi$ is conserved by this CH equation (2.30), which is often postulated phenomenologically (see, e.g., Hohenberg & Halperin 1977; Puri & Wadhawan 2009; Täuber 2013; Ma 2018) and which has been used extensively in studies of phase separation, nucleation, and spinodal decomposition. If the right-hand side of the CH equation (2.30) includes a ϕ-conserving Gaussian white-noise term $\theta(\mathbf{r}, t)$ with zero-mean and with a variance that satisfies the fluctuation-dissipation theorem, it is known as Model B or the Cahn–Hilliard–Cook equation. This noise term plays an important role in the calculation of critical exponents. For Model B, at the simplest level, (2.30) yields $z_{MF}^B = 4$, which should be contrasted with the Model-A result $z_{MF}^A = 2$.

Before we proceed to our discussion of the CHNS PDEs, we summarise below the types of time-dependent phenomena that can be studied by using the TDGL and CH equations.

(i) Space and time dependent correlation functions, e.g.

$$C(\mathbf{r}, t) \equiv \langle \phi(\mathbf{R}, t_0)\phi(\mathbf{R} + \mathbf{r}, t_0 + t) \rangle_{t_0, \mathbf{R}} - \langle \phi(\mathbf{R}, t_0) \rangle_{t_0, \mathbf{R}}^2, \tag{2.31}$$

which can be used to study critical dynamics (see, e.g., Hohenberg & Halperin 1977; Täuber 2013) and the kinetics of phase separation (see, e.g., Bray 2002; Puri 2004; Puri & Wadhawan 2009).

(ii) Consider the schematic plot of $g(\phi)$, which appears in (2.11) for $\mathcal{F}_{LG}$, in figure 4(b) (we set $h = 0$) and the associated schematic phase diagram shown in figure 4(a). The early stages of phase separation can occur via nucleation, or droplet-type fluctuations, and spinodal decomposition, or small-amplitude long-wavelength fluctuations (see, e.g., Oki *et al.* (1977), Gunton *et al.* (1983) and, in particular, figure 3 in Gunton *et al.* (1983), which has been reproduced from Oki *et al.* (1977)). At the level of LG theory, the loci of points along which $g''(\phi) = 0$ is the spinodal curve that provides a clear boundary between the regions with nucleation-dominated ($g''(\phi) > 0$) growth and spinodal decomposition ($g''(\phi) < 0$) in figure 4(a). If we go beyond mean-field or LG theory and consider the early stages of phase separation, the sharp spinodal curve is replaced by a crossover regime across which the phase-separating system moves from nucleation-dominated to spinodal-decomposition-initiated growth (see, e.g., Oki *et al.* 1977; Gunton *et al.* 1983).

(iii) Late stages of phase separation. Here, we must distinguish Lifshitz–Slyozov and Lifshitz–Allen–Cahn scaling laws, for conserved and non-conserved ϕ, respectively; the former (latter) leads to domain growth in time t that is characterised by the power-law growth of the length $\mathcal{L}(t) \sim t^{1/3}$ $\mathcal{L}(t) \sim t^{1/2}$ as discussed, e.g., in Lifshitz & Slyozov (1961), Lifshitz (1962), Fogedby & Mouritsen (1988), Bray (2002), Puri (2004) and Puri & Wadhawan (2009). Hydrodynamical effects can modify the domain-growth power-law exponent (see, e.g., Bray 2002; Puri 2004; Puri & Wadhawan 2009).

3. Cahn–Hilliard–Navier–Stokes models

Henceforth, we will not consider critical phenomena in the CHNS system and its generalisations. We will concentrate on turbulence in these systems, well below the transition temperature T_c, and the effects it has on the suppression of phase separation (also called coarsening arrest) or droplet motion in turbulent binary- or ternary-fluid flows,

the coalescence of droplets or lenses, and turbulence and self-propelled droplets in active-CHNS models. Therefore, it will be convenient to work at a fixed temperature below T_c and use a LG free-energy functional in which parameters are scaled in such a way that the minima of F_{LG} are at $\phi_b = \pm 1$ in the two-fluid case. For related derivations of the CHNS model and reviews of diffuse-interface models (see, e.g., Gurtin *et al.* 1996 and Anderson *et al.* 1998). We define below the CHNS models that we consider. Sections 3.1 and 7.1 cover, respectively, binary- and ternary-fluid systems. In §7.1.1 describes the Boussinesq approximation for the ternary-fluid case. We then turn to active models: in §7.6 we introduce the active Model H and in §7.7 a generalisation that allows us to study the self-propulsion of an active droplet.

3.1. *Binary-fluid CHNS*

(i) For the binary-fluid case (see, e.g., Guo *et al.* 2021; Borcia *et al.* 2022) we use the following free-energy functional for our CHNS equations:

$$\mathcal{F}[\phi, \nabla\phi] = \int_\Omega d\Omega \left[\mathcal{V}(\phi) + \frac{3}{4}\sigma\epsilon|\nabla\phi|^2 \right], \quad (3.1)$$

where $\mathcal{V}(\phi)$ is the potential, σ is the bare interfacial tension and ϵ is the width of the interface. The following two forms of $\mathcal{V}(\phi)$ are used in the CHNS literature:

(*a*) Curie–Weiss-type potential,

$$\mathcal{V}_{CW}(\phi) = \frac{a}{2}\left[(1+\phi)\ln(1+\phi) + (1-\phi)\ln(1-\phi)\right] - \frac{b}{2}\phi^2; \quad (3.2)$$

this potential has the virtue that $\phi \in [-1, 1]$. (In some studies $\mathcal{V}_{CW}$ is called the Flory–Huggins logarithmic potential (see, e.g., Giorgini & Temam 2020), as in the theory of polymer solutions (see, e.g., Rubinstein & Colby 2003).)

(*b*) LG-type ϕ^4 potential,

$$\mathcal{V}_{LG}(\phi) = \frac{3}{16}\frac{\sigma}{\epsilon}(\phi^2 - 1)^2; \quad (3.3)$$

this parametrisation has the virtue that the global minima of $\mathcal{V}_{LG}(\phi)$ are at $\phi_b = \pm 1$. However, now $\phi \in [-\infty, \infty]$. We use $\mathcal{V}_{LG}(\phi)$ in most of our CHNS studies.

(ii) If we allow the shear viscosity η and the density ρ to depend on ϕ, so that the two coexisting phases have different viscosities (η_1 and η_2) and densities (ρ_1 and ρ_2), far away from interfaces, the incompressible CHNS equations can be written as follows:

$$\rho(\phi)(\partial_t \boldsymbol{u} + (\boldsymbol{u}\cdot\nabla)\boldsymbol{u}) = -\nabla P + \nabla\cdot\left[\eta(\phi)(\nabla\boldsymbol{u} + \nabla\boldsymbol{u}^T)\right]$$
$$- \phi\nabla\mu + \rho(\phi)\boldsymbol{g} - \alpha\boldsymbol{u} + \boldsymbol{f}^{ext};$$
$$\nabla\cdot\boldsymbol{u} = 0;$$
$$\partial_t\phi + (\boldsymbol{u}\cdot\nabla)\phi = M\nabla^2\mu;$$
$$\mu = \frac{\delta\mathcal{F}}{\delta\phi};$$
$$\eta(\phi) = \eta_1\left(\frac{1+\phi}{2}\right) + \eta_2\left(\frac{1-\phi}{2}\right);$$
$$\rho(\phi) = \rho_1\left(\frac{1+\phi}{2}\right) + \rho_2\left(\frac{1-\phi}{2}\right). \quad (3.4)$$

Dimensionless numbers	Formulae
Reynolds number	$Re = U_0 L_0 / \nu$
Peclet number	$Pe = U_0 L_0 / \nu$
Bond number	$Bo = \mathcal{A} \rho L_0^2 g / \sigma$
Ohnesorge number	$Oh = \nu \sqrt{\frac{\rho}{\sigma L_0}}$
Capillary number	$Ca = \rho \nu U_0 / \sigma$
Weber number	$We = \rho U_0^2 L_0 / \sigma$
Cahn number	$Cn = \epsilon / L_0$

Table 2. Important dimensionless numbers for the binary-fluid CHNS system.

Here, $\boldsymbol{g}$, $\boldsymbol{f}^{ext}$ and α are, respectively, the acceleration because of gravity, an external forcing, and the coefficient of friction (which is required typically in two-dimensional (2-D) settings, e.g. to account for bottom friction).

(iii) Boussinesq approximation. If the density difference between the two phases is not too large, in the NS part of the above equations we can use the Boussinesq approximation (see, e.g., Celani *et al.* 2009; Boffetta *et al.* 2010; Lee & Kim 2013*a*,*b*; Shah, Saeed & Yuan 2017; Khan & Shah 2019; Zanella *et al.* 2020; Forbes, Turner & Walters 2022; Huang & Yang 2022). Furthermore, this approximation holds only when the vorticity is not too strong; otherwise, non-Boussinesq effects, such as interfacial instabilities, can emerge even at low Atwood numbers (see, e.g., Ramadugu, Perlekar & Govindarajan 2022). In this Boussinesq approximation the NS equations can be written as follows:

$$\partial_t \boldsymbol{u} + (\boldsymbol{u} \cdot \nabla)\boldsymbol{u} = -\frac{1}{\rho_0} \nabla P + \nu \nabla^2 \boldsymbol{u} - \frac{1}{\rho_0}(\phi \nabla \mu) + \frac{[\rho(\phi) - \rho_0]}{\rho_0} \boldsymbol{g} - \alpha \boldsymbol{u},$$
$$\nabla \cdot \boldsymbol{u} = 0, \tag{3.5}$$

where the mean density is $\rho_0 = (\rho_1 + \rho_2)/2$. This approximation neglects density differences except in the term with gravity. We can write

$$\frac{(\rho(\phi) - \rho_0)}{\rho_0} = -\frac{\Delta \rho}{\rho_0} \phi \equiv -\mathcal{A}\phi, \tag{3.6}$$

with the Atwood number $\mathcal{A} \ll 1$.

In table 2 we give the important dimensionless parameters that govern the states of the binary-fluid CHNS system. The larger the Reynolds number Re, the more the inertia-induced turbulence, which can lead, e.g., to coarsening arrest (§ 6.3). The Bond number Bo plays a crucial role in gravity-driven flows that include the evolution of antibubbles (§ 6.4) or a bubble passing through a liquid–liquid interface (§ 7.4); the Ohnesorge number Oh is important in the coalescence of droplets or liquid lenses (§ 7.5); and the Weber (We) and Capillary (Ca) numbers affect interface-induced low-Re turbulence (§ 6.5). The Cahn number governs the thickness of the interface. Other dimensionless numbers must be introduced as we increase the complexity of the multiphase system; e.g., in three-phase flows, density, surface-tension and viscosity ratios are relevant (§ 7.2), and the activity parameter is important in active CHNS systems (§§ 7.8 and 7.9).

4. Numerical methods

Various numerical methods have been employed successfully to simulate multiphase flows using phase-field methods, in general, and the CHNS equations, in particular. To capture

the underlying physics, it is crucial to resolve interfaces accurately and to track their evolution. Common numerical discretisation techniques include the finite element method (see, e.g., Elliott & French 1987; Barrett *et al.* 1999, 2001; Vey & Voigt 2007; Lowengrub *et al.* 2009), finite difference methods (see, e.g., Furihata 2001; Kim & Kang 2009; Teigen *et al.* 2011) and the LBM (see, e.g., Benzi & Succi 1990; Benzi, Succi & Vergassola 1992; Shan & Chen 1993, 1994; Chen & Doolen 1998; Scarbolo & Soldati 2013; Timm *et al.* 2016), each one of which offers distinct advantages that depend on both the complexity of the problem and the computational demands of the numerical simulation. In this article, we adopt DNSs that are based on the pseudospectral approach (see, e.g., Canuto, Hussaini & Quarteroni 1988).

Direct numerical simulations play an important role in obtaining solutions of the CHNS equations. Interfaces are diffuse in CHNS systems, so we do not have to impose BCs on complicated interfaces that evolve in time. A DNS must, of course, accurately resolve all relevant scales of motion, given initial and BCs. Such DNSs can achieve a high level of accuracy by retaining the governing equations in their complete (rather than reduced) forms. However, DNSs can be computationally expensive, particularly at high Reynolds numbers and for coupled hydrodynamical equations, such as the CHNS equations, which contain many nonlinear terms. In §§ 4.1 and 4.2 we give, respectively, overviews of the pseudsoectral and volume-penalisation methods that we use in our direct numerical simulations of CHNS models.

4.1. *Pseudospectral method*

The pseudospectral method, a widely used numerical technique for solving hydrodynamical PDEs, was pioneered over 50 years ago by Patterson Jr & Orszag (1971) and has been used, *inter alia*, to study fluid turbulence (see, e.g., McWilliams 1984; Canuto *et al.* 1988; Pandit, Perlekar & Ray 2009; Celani, Musacchio & Vincenzi 2010; San & Staples 2012; Buaria & Sreenivasan 2022, 2023), magnetohydrodynamic (MHD) turbulence (see, e.g., Basu *et al.* 1998; Müller & Biskamp 2000; Verma 2004; Gómez, Mininni & Dmitruk 2005; Sahoo *et al.* 2011, 2020; Dritschel & Tobias 2012; Yadav, Miura & Pandit 2022), CHNS turbulence (see, e.g., Scarbolo & Soldati 2013; Perlekar *et al.* 2014; Pal *et al.* 2016; Pandit *et al.* 2017; Vela-Martín & Avila 2021; Pal *et al.* 2022; Vela-Martín & Avila 2022), the coalescence of droplets and liquid lenses (see, e.g., Padhan & Pandit 2023*b*); Soligo, Roccon & Soldati 2019), elastic turbulence in polymer solutions (see, e.g., Berti *et al.* 2008; Gupta & Pandit 2017; Plan, Vincenzi & Gibbon 2017; Singh *et al.* 2024) and active turbulence and active droplets (see, e.g., Gao & Li 2017; Rana & Perlekar 2020; Mukherjee *et al.* 2021, 2023; Li & Koch 2022; Gibbon *et al.* 2023; Kiran *et al.* 2023; Padhan & Pandit 2023*a*; Puggioni Leonardo & Stefano 2023; Backofen *et al.* 2024).

We employ the Fourier pseudospectral method, which is known for its accuracy and efficiency in comparison with other numerical methods (see, e.g., Orszag & Pao 1975; Canuto *et al.* 1988); in its most common form, this method uses plane waves as basis functions. We solve the coupled CHNS equations in a periodic domain $\mathcal{D} \equiv l^d$, with l the length of the side of (typically) d-dimensional hypercubic domain. To illustrate this method, we simplify (3.4) by making the following two key assumptions: all fluids have identical densities (i.e. $\rho_1 = \rho_2 = \rho_0 = 1$) and identical viscosities (i.e. $\eta_1 = \eta_2 = \eta$). The equations are given below for two dimensions and three dimensions.

4.1.1. *Equations in two dimensions*

In two dimensions, we solve the CHNS equations in its vorticity–stream function form (see, e.g., Boffetta & Ecke 2012; Pal *et al.* 2016; Padhan & Pandit 2023*a*),

$$\partial_t \omega + (\boldsymbol{u} \cdot \nabla)\omega = \nu\nabla^2\omega - \alpha\omega - [\nabla \times (\phi\nabla\mu)] \cdot \hat{e}_z + f^\omega;$$
$$\nabla \cdot \boldsymbol{u} = 0; \quad \omega = (\nabla \times \boldsymbol{u}) \cdot \hat{e}_z;$$
$$\partial_t \phi + (\boldsymbol{u} \cdot \nabla)\phi = M\nabla^2\mu; \quad \mu = -\frac{3}{2}\sigma\epsilon\nabla^2\phi + \frac{3}{4}\frac{\sigma}{\epsilon}(\phi^3 - \phi). \tag{4.1}$$

4.1.2. *Equations in three dimensions*
In three dimensions, we use

$$\partial_t \boldsymbol{u} + (\boldsymbol{u} \cdot \nabla)\boldsymbol{u} = -\nabla P + \nu\nabla^2\boldsymbol{u} - \phi\nabla\mu - \alpha\boldsymbol{u} + \boldsymbol{f}^{ext};$$
$$\nabla \cdot \boldsymbol{u} = 0;$$
$$\partial_t \phi + (\boldsymbol{u} \cdot \nabla)\phi = M\nabla^2\mu; \quad \mu = -\frac{3}{2}\sigma\epsilon\nabla^2\phi + \frac{3}{4}\frac{\sigma}{\epsilon}(\phi^3 - \phi). \tag{4.2}$$

Here $\nu = \eta/\rho_0$ is the kinematic viscosity. In most three-dimensional (3-D) applications, $\alpha = 0$.

Our representation of the phase fields, velocity fields, vorticity fields and pressure fields utilises the (truncated) Fourier projection onto a grid of N^d points, which are expressed as follows (carets denote spatial Fourier transform):

$$\phi(\boldsymbol{x}, t) = \sum_{|k|<N} \hat{\phi}(\boldsymbol{k}, t)\exp(i\boldsymbol{k} \cdot \boldsymbol{x}); \tag{4.3}$$

$$\boldsymbol{u}(\boldsymbol{x}, t) = \sum_{|k|<N} \hat{\boldsymbol{u}}(\boldsymbol{k}, t)\exp(i\boldsymbol{k} \cdot \boldsymbol{x}); \tag{4.4}$$

$$\boldsymbol{\omega}(\boldsymbol{x}, t) = \sum_{|k|<N} \hat{\boldsymbol{\omega}}(\boldsymbol{k}, t)\exp(i\boldsymbol{k} \cdot \boldsymbol{x}); \tag{4.5}$$

$$P(\boldsymbol{x}, t) = \sum_{|k|<N} \hat{P}(\boldsymbol{k}, t)\exp(i\boldsymbol{k} \cdot \boldsymbol{x}). \tag{4.6}$$

There are N^d wavenumbers: $\boldsymbol{k} \equiv k_0\boldsymbol{n} = k_0 \sum_{i=1}^d n_i\hat{e}_i$, where $k_0 = 2\pi/l$ is the lowest wavenumber and n_i are integers with values ranging from $(-(N/2)+1)$ to $N/2$. In each direction, the largest wavenumber is $k_{max} = k_0 N/2$. (The spectral representation mentioned above aligns with representing the fields in physical space on an N^d grid with uniform spacing $\Delta x = l/N = \pi/k_{max}$.) We write, below, the CHNS equations in terms of the above Fourier modes.

4.1.3. *Two-dimensional CHNS equations in Fourier space*
We write (4.1) in Fourier space as follows:

$$\partial_t \hat{\omega}(\boldsymbol{k}, t) = -\widehat{(\boldsymbol{u} \cdot \nabla\omega)}(\boldsymbol{k}, t) - \nu k^2\hat{\omega}(\boldsymbol{k}, t) - i\boldsymbol{k} \times \widehat{(\phi\nabla\mu)}(\boldsymbol{k}, t) - \alpha\hat{\omega}(\boldsymbol{k}, t); \tag{4.7}$$

$$i\boldsymbol{k} \cdot \hat{\boldsymbol{u}}(\boldsymbol{k}, t) = 0; \quad \hat{\omega}(\boldsymbol{k}, t) = i\boldsymbol{k} \times \hat{\boldsymbol{u}}(\boldsymbol{k}, t); \tag{4.8}$$

$$\hat{\psi}(\boldsymbol{k}, t) = \frac{\hat{\omega}(\boldsymbol{k}, t)}{k^2}; \tag{4.9}$$

$$\partial_t \hat{\phi}(\boldsymbol{k}, t) = -\widehat{(\boldsymbol{u} \cdot \nabla\phi)}(\boldsymbol{k}, t) - Mk^2\hat{\mu}(\boldsymbol{k}, t); \tag{4.10}$$

$$\mu(\boldsymbol{k}, t) = \frac{3}{2}\sigma\epsilon k^2\hat{\phi}(\boldsymbol{k}, t) + \frac{3}{4}\frac{\sigma}{\epsilon}[\hat{\phi^3}(\boldsymbol{k}, t) - \hat{\phi}(\boldsymbol{k}, t)]. \tag{4.11}$$

4.1.4. *Three-dimensional CHNS equations in Fourier space*

We write (4.2) in Fourier space as follows:

$$\partial_t \hat{\boldsymbol{u}}(\boldsymbol{k}, t) = \mathbb{P}(\boldsymbol{k}) \cdot \left[-\widehat{(\boldsymbol{u} \cdot \nabla \boldsymbol{u})}(\boldsymbol{k}, t) - \widehat{(\phi \nabla \mu)}(\boldsymbol{k}, t) \right] - \nu k^2 \hat{\boldsymbol{u}}(\boldsymbol{k}, t) - \alpha \hat{\boldsymbol{u}}(\boldsymbol{k}, t); \quad (4.12)$$

$$i\boldsymbol{k} \cdot \hat{\boldsymbol{u}}(\boldsymbol{k}, t) = 0; \quad (4.13)$$

$$\partial_t \hat{\phi}(\boldsymbol{k}, t) = -\widehat{(\boldsymbol{u} \cdot \nabla \phi)}(\boldsymbol{k}, t) - Mk^2 \hat{\mu}(\boldsymbol{k}, t); \quad (4.14)$$

$$\mu(\boldsymbol{k}, t) = \frac{3}{2}\sigma \epsilon k^2 \hat{\phi}(\boldsymbol{k}, t) + \frac{3}{4}\frac{\sigma}{\epsilon}[\hat{\phi}^3(\boldsymbol{k}, t) - \hat{\phi}(\boldsymbol{k}, t)]; \quad (4.15)$$

where $\mathbb{P}$ is the transverse projection operator with components

$$\mathbb{P}_{ij}(\boldsymbol{k}) = \left(\delta_{ij} - \frac{k_i k_j}{k^2} \right). \quad (4.16)$$

To perform Fourier transforms, we utilise the FFTW library (Frigo & Johnson 1998), which employs the Cooley–Tukey fast-Fourier-transform algorithm (see Cooley & Tukey 1965). The nonlinear terms such as $\boldsymbol{u} \cdot \nabla \boldsymbol{u}$, $\boldsymbol{u} \cdot \nabla \phi$ and $\mu \nabla \phi$ lead to convolution sums that require N^{2d} operations; and the cubic nonlinear term ϕ^3 requires N^{3d} operations in Fourier space. To bypass the high computational cost of these operations, we use the pseudospectral method in which we evaluate these nonlinear terms as follows. First, we transform the fields back to real space; and then we perform the multiplications in real space and transform them back to Fourier space again. This procedure improves greatly the computational efficiency of the pseudospectral method compared with the ordinary spectral methods. However, the Fourier pseudospectral method leads to aliasing errors while evaluating the nonlinear terms, which we remove by using the 1/2-dealiasing scheme (see, e.g., Patterson Jr & Orszag 1971; Hou & Li 2007; Padhan & Pandit 2023a), because of the cubic nonlinearity.

The computational cost of such a pseudospectral DNS (see, e.g., Moin & Mahesh 1998) increases with the number of grid points, which must increase in turn to resolve small-scale structures. For statistically homogeneous and isotropic turbulence in three dimensions, the standard estimate (based on Kolmogorov 1941 phenomenology) is $N \sim Re^{9/4}$, where Re is the Reynolds number. A DNS of turbulence in the CHNS PDEs the grid spacing Δx must be small enough to capture both the (Kolmogorv) dissipation scale and the widths of interfaces.

For the time integration of (4.7)–(4.15) we use a semi-implicit exponential time-differentiating Runge–Kutta2 (ETDRK2) approach, which treats the linear terms implicitly with their exact solutions as described in Cox & Matthews 2002). This method, which combines the ETD method with the RK2 method, offers several advantages over other numerical techniques, including enhanced accuracy, efficiency, stability and ease of implementation. We write the CHNS equations (4.7), (4.10) and (4.11) in the following general form:

$$\frac{\mathrm{d}q_1(t)}{\mathrm{d}t} = \lambda_1 q_1(t) + \mathcal{G}(q_1, q_2); \quad (4.17)$$

$$\frac{\mathrm{d}q_2(t)}{\mathrm{d}t} = \lambda_2 q_2(t) + \mathcal{H}(q_1, q_2); \quad (4.18)$$

here,

$$q_1(t) \equiv \hat{\omega}(\boldsymbol{k}, t); \qquad \lambda_1 \equiv (-\nu k^2 - \alpha);$$

$$q_2(t) \equiv \hat{\phi}(\boldsymbol{k}, t); \qquad \lambda_2 \equiv \left(-\frac{3}{2} M \sigma \epsilon k^4 + \frac{3}{4} \frac{\sigma}{\epsilon} M k^2 \right);$$

$$\mathcal{G}(q_1, q_2) \equiv -\widehat{(\boldsymbol{u} \cdot \nabla \boldsymbol{\omega})}(\boldsymbol{k}, t) + i\boldsymbol{k} \times \widehat{(\mu \nabla \phi)}(\boldsymbol{k}, t);$$

$$\mathcal{H}(q_1, q_2) \equiv -\widehat{(\boldsymbol{u} \cdot \nabla \phi)}(\boldsymbol{k}, t) - \frac{3}{4} \frac{\sigma}{\epsilon} M k^2 \hat{\phi}(\boldsymbol{k}, t). \tag{4.19}$$

In the ETDRK2 algorithm, (4.17) and (4.18) have the solution

$$a_1^n = q_1^n \exp(\lambda_1 \Delta t) + \mathcal{G}(q_1^n, q_2^n) \left(\frac{\exp(\lambda_1 \Delta t) - 1}{\lambda_1} \right); \tag{4.20}$$

$$a_2^n = q_2^n \exp(\lambda_2 \Delta t) + \mathcal{H}(q_1^n, q_2^n) \left(\frac{\exp(\lambda_2 \Delta t) - 1}{\lambda_2} \right); \tag{4.21}$$

$$q_1^{n+1} = a_1^n + \left[\mathcal{G}(a_1^n, a_2^n) - \mathcal{G}(q_1^n, q_2^n) \right] \left(\frac{\exp(\lambda_1 \Delta t) - 1 - \lambda_1 \Delta t}{\lambda_1^2 \Delta t} \right); \tag{4.22}$$

$$q_2^{n+1} = a_2^n + \left[\mathcal{H}(a_1^n, a_2^n) - \mathcal{H}(q_1^n, q_2^n) \right] \left(\frac{\exp(\lambda_2 \Delta t) - 1 - \lambda_2 \Delta t}{\lambda_2^2 \Delta t} \right); \tag{4.23}$$

for simplicity, we use $q_1^{n+1} \equiv q_1(t + \Delta t)$ and $q_1^n \equiv q_1(t)$.

4.2. *Volume-penalised CHNS*

Fluid–structure interactions play a crucial role in multiphase flows, where solid boundaries or immersed objects influence phase separation, interfacial dynamics and transport properties (see, e.g., HUAT 2015; Zheng *et al.* 2021; Hester *et al.* 2023; Pavuluri *et al.* 2023; Treeratanaphitak & Abukhdeir 2023; Hou *et al.* 2024). These interactions are challenging in computational fluid dynamics because of the enforcement of BCs at the fluid–solid interface (see, e.g., Mokbel, Abels & Aland 2018; Pramanik, Verstappen & Onck 2024). The numerical implementation of these BCs is especially difficult when the immersed solid is in motion. The immersed boundary method has been used widely in computational fluid dynamics to handle such interactions (see, e.g., Mittal & Iaccarino 2005; Mittal & Seo 2023). The volume penalisation method (VPM) is a type of immersed boundary method that is simple and versatile in modelling objects in fluid flows; it is gaining in popularity, given its ease of implementation (see, e.g., Kolomenskiy & Schneider 2009; Kadoch *et al.* 2012; Morales *et al.* 2014; Engels *et al.* 2016, 2022; Hester, Vasil & Burns 2021; Sinhababu & Bhattacharya 2022; Mittal & Seo 2023; Puggioni Leonardo & Stefano 2023). Without imposing explicit BCs, the VPM uses an extra force as a penalisation term in the classical NS equations; the modified equation is known as the Brinkman model (see, e.g., Angot, Bruneau & Fabrie 1999). The VPM approximates solid boundaries in a fluid by applying rapid linear damping within a fictitious solid region. This approach allows for the simulation of complex, moving objects within general numerical solvers without the need for specialised algorithms or boundary-conforming grids. The VPM treats solids as porous media that are characterised by negligible permeability, resulting in the velocity of the adjacent fluid becoming zero at the fluid–solid interface. This method can be easily incorporated into a DNS solver that employs periodic BCs. The VPM has been successfully implemented in the NS equations, passive scalar equations,

MHD equations, CH equations and the Toner–Tu–Swift–Hohenberg equations (see, e.g., Kadoch *et al.* 2012; Morales *et al.* 2014; Engels *et al.* 2016, 2022; Sinhababu, Bhattacharya & Ayyalasomayajula 2021; Puggioni Leonardo & Stefano 2023). We extend the VPM method to the CHNS equations as follows (for illustration we use the 2-D CHNS system):

$$\partial_t \omega + (\boldsymbol{u} \cdot \nabla)\omega = \nu \nabla^2 \omega - \alpha\omega - [\nabla \times (\phi \nabla \mu)] \cdot \hat{e}_z + f^\omega - \nabla \times \left[\frac{\chi}{\eta_p}\boldsymbol{u}\right];$$

$$\nabla \cdot \boldsymbol{u} = 0; \quad \omega = (\nabla \times \boldsymbol{u}) \cdot \hat{e}_z;$$

$$\partial_t \phi + [(1 - \chi)\boldsymbol{u}] \cdot \nabla\phi = \nabla \cdot ([M(1 - \chi) + M_p\chi]\nabla\mu). \tag{4.24}$$

Here, η_p and M_p are the penalisation parameters (or permeabilities) associated with the velocity and ϕ fields, respectively. Here χ is the mask function to distinguish solid and fluid regions, which is defined as follows:

$$\chi(\boldsymbol{x}) = \begin{cases} 1 & \text{for } \boldsymbol{x} \in \Omega_s; \\ 0 & \text{for } \boldsymbol{x} \in \Omega_f; \end{cases} \tag{4.25}$$

where Ω_s and Ω_f are the volumes representing solid and fluid regions. The term $[M(1 - \chi) + M_p\chi]$ takes into account the no-flux BCs at the solid–fluid interface $\nabla\phi \cdot \hat{n}|_{\Omega_f} = 0$; $\hat{n}$ is the unit vector that is normal to the solid wall.

5. Mathematical challenges

The Euler PDEs for an inviscid fluid (see, e.g., Euler 1761; Darrigol & Frisch 2008; Gibbon 2008) predate their viscous version by 61 years. Given analytic initial data, solutions of the incompressible 2-D Euler equation, do not exhibit a finite-time singularity; however, it is still not known if any solutions of the 3-D Euler equations develop a singularity in a finite time, if we start with analytic initial data (see, e.g., Majda, Bertozzi & Ogawa 2002; Bardos & Titi 2007; Gibbon 2008; Drivas & Elgindi 2023); there has been some recent progress on a possible finite-time singularity for the 3-D axisymmetric Euler equation (see Luo & Hou 2014; Hertel, Besse & Frisch 2022; Kolluru, Sharma & Pandit 2022). For the NS PDEs global regularity of solutions, with analytic initial data, can be proved in two dimensions but not in three dimensions (see, e.g., Constantin & Foiaş 1988; Doering & Gibbon 1995; Galdi 2000; Doering 2009; Robinson, Rodrigo & Sadowski 2016; Lemarié-Rieusset 2018; Robinson 2020). The proof of regularity (or lack thereof), for all time, of solutions of the 3-D NS PDEs is one of the Clay Millennium Prize Problems (for domains without boundary; see, e.g., Robinson 2020).

Since its introduction by Cahn & Hilliard 1958), the CH PDE has been used extensively in multiphase statistical mechanics, nucleation, spinodal decomposition and the late stages of phase separation (see, e.g., Cahn 1961; Lifshitz & Slyozov 1961; Lothe & Pound 1962; Hohenberg & Halperin 1977; Gunton *et al.* 1983; Chaikin *et al.* 1995; Anderson *et al.* 1998; Bray 2002; Onuki 2002; Badalassi *et al.* 2003; Berti *et al.* 2005; Puri & Wadhawan 2009; Perlekar *et al.* 2014). The well-posedness of the CH PDE has been considered in several works, such as Elliott & Songmu (1986), Elliott & Mikelić (1991), Dlotko (1994), Liu, Qi & Yin (2006), Miranville (2019) and Wu (2021), to which we refer the reader.

The important questions for the CHNS PDEs concern the smoothness, or lack thereof, of the contours of ϕ within fluid interfaces and their interplay with the regularity of the solutions of the NS part of this system. We turn now to a brief overview of mathematical results for the regularity of solutions of the CHNS PDEs.

Several results are available in two dimensions; for the 2-D CHNS system see, e.g., Abels (2009*a*,*b*) and Gal & Grasselli (2010). In particular, Gal & Grasselli (2010) have

shown that, in a bounded domain or with periodic BCs, and with suitably smooth initial data, this system possesses a global attractor $\mathfrak{A}$; the existence of an exponential attractor $\mathcal{E}$ has also been established, whence it is concluded (see Gal & Grasselli 2010) that the fractal dimension of $\mathfrak{A}$ is finite; this dimension can be estimated. Furthermore, it has been demonstrated that each trajectory converges to a single equilibrium.

As we have mentioned above, the regularity of solutions of the 3-D NS equations continues to be a major open challenge (see, e.g., Constantin & Foiaş 1988; Doering & Gibbon 1995; Galdi 2000; Doering 2009; Robinson *et al.* 2016; Lemarié-Rieusset 2018; Robinson 2020). The coupling to the 3-D CH equations brings with it the difficulties associated with the smoothness of contours of ϕ, which could, for example, lead to finite-time singularities in arbitrarily large spatial derivatives of ϕ. Such issues have been addressed by Gibbon *et al.* (2016*b*, 2018), who adopt an approach related to the Beale–Kato–Majda (BKM) strategy (see Beale, Kato & Majda 1984) for the incompressible 3-D Euler equations. In particular, BKM showed that, if

$$\mathcal{I}_\omega(T^*) = \int_0^{T^*} \|\boldsymbol{\omega}\|_\infty \, \mathrm{d}\tau, \tag{5.1}$$

where the subscript ∞ indicates the L^∞-norm (also called the sup- or maximum norm), is finite, then the solution is regular up until time T^*; by contrast, if $\mathcal{I}_\omega(T^*)$ becomes infinite at T^*, then the solution loses regularity or, in common parlance, it blows up. To monitor such blow up, it suffices to consider (5.1) alone; specifically, if it is finite, high-order spatial derivatives of the velocity cannot develop singularities. Similarly, for the 3-D CHNS system it has been shown that (see Gibbon *et al.* 2016*b*, 2018) it is possible to obtain a BKM-type regularity criterion by using the energy of the CHNS system

$$E(t) = \int_V \left[\frac{\Lambda}{2} |\nabla\phi|^2 + \frac{\Lambda}{4\epsilon^2} (\phi^2 - 1)^2 + \frac{1}{2} |\boldsymbol{u}|^2 \right] \mathrm{d}V, \tag{5.2}$$

which comprises a combination of squares of L^2-norms, whose L^∞ version, the maximal energy, is

$$E_\infty(t) = \frac{1}{2} \Lambda \|\nabla\phi\|_\infty^2 + \frac{\Lambda}{4\epsilon^2} \left(\|\phi\|_\infty^2 - 1 \right)^2 + \frac{1}{2} \|\boldsymbol{u}\|_\infty^2; \tag{5.3}$$

with the coefficient $\Lambda = (3/4)\sigma\epsilon$. Gibbon *et al.* (2016*b*, 2018) have proved that

$$\mathcal{I}_E(T^*) = \int_0^{T^*} E_\infty(\tau) \, \mathrm{d}\tau \tag{5.4}$$

controls the regularity of solutions of the 3-D CHNS PDEs exactly as $\mathcal{I}(T^*)_\omega$ does for the 3-D Euler equations (see Beale *et al.* 1984). Although we have used the *LG* form of (2.11) here, these results also follow for the *CW* form of (2.10). Furthermore, Gibbon *et al.* (2016*b*, 2018) have examined the time dependence of scaled L^{2m}-norms of the vorticity and gradients of ϕ and compared them with their counterparts for the NS and related equations (see Donzis *et al.* 2013; Gibbon *et al.* 2014, 2016*a*).

Several other groups (see, e.g., Giorgini, Miranville & Temam 2019; Giorgini & Temam 2020; Giorgini 2021) have considered weak and strong solutions of the CHNS system (they refer to it as the Navier–Stokes–Cahn–Hilliard system), in bounded smooth domains in two dimensions and three dimensions, with a concentration-dependent viscosity and both *LG* and *CW* forms of (2.11) and (2.10) for the variational free energy. In two dimensions and three dimensions, they have proved the existence of global weak solutions and the existence of strong solutions with bounded and strictly positive density. Furthermore

(see Giorgini *et al.* 2019; Giorgini & Temam 2020; Giorgini 2021), the strong solutions are local in time (in three dimensions) and global in time (in two dimensions).

6. Illustrative CHNS-based DNS studies of multiphase flows

We now present illustrative examples of the use of the CHNS framework for studies of a variety of multiphase flows. We begin with the RT and KH instabilities in the binary-fluid CHNS system in §§ 6.1 and 6.2, respectively. Then, in § 6.3 we describe how the CHNS framework can be used to study phase separation, and its turbulence-induced suppression, in binary-fluid mixtures. Section 6.4 discusses the spatiotemporal evolution of antibubbles. In § 6.5 we show how interfacial fluctuations in a binary mixture of immiscible fluids can lead to turbulence at low Reynolds numbers.

6.1. *Rayleigh–Taylor instability: CHNS (two dimensions)*

We illustrate how the CHNS framework can be used to simulate the gravity-induced RT instability (see, e.g., Drazin 2002; Charru 2011; Livescu, Wei & Petersen 2011), which occurs when a dense fluid is positioned, initially, above a less dense one (see, e.g., Tryggvason 1988; Youngs 1992; Young *et al.* 2001; Kadau *et al.* 2004; Celani *et al.* 2009; Livescu *et al.* 2011; Lee & Kim 2013; Khomenko *et al.* 2014; Gibbon *et al.* 2016; Talat *et al.* 2018; Gonzalez-Gutiérrez & de Andrea González 2019; Khan & Shah 2019; Lherm *et al.* 2021; Garoosi & Mahdi 2022; Lherm *et al.* 2022; Pandya & Shkoller 2023). The CHNS framework has been shown to be useful in studying RT instabilities in immiscible fluids (see, e.g., Celani *et al.* 2009; Lee & Kim 2013; Gibbon *et al.* 2016*b*). We demonstrate this by an illustrative pseudospectral DNS of the 2-D CHNS equations, with the Boussinesq approximation (3.5)–(3.6), in a 2-D rectangular box $(L_x, L_y) = (2\pi, 4\pi)$; we incorporate impenetrable boundaries in the y-direction by using the volume-penalisation method, withsix grid points on both the top and bottom boundaries for penalisation. The initial conditions we use are as follows:

$$\phi(x, y, t=0) = \tanh\left[\frac{y - L_y/2 - h_0\cos(mx)}{\epsilon/2}\right]; \tag{6.1}$$
$$\omega(x, y, t=0) = 0;$$

where h_0 is the amplitude of the perturbation we impose on top of a flat interface at $L_y/2$. In figure 6(*a,b*), we present pseudocolour plots of ϕ and ω; these show how the RT instability develops in time (which increases from left to right); the top phase (in red) has a higher density than the bottom phase (in blue); and the Atwood number is $\mathcal{A} = 0.6$. We can quantify the temporal growth of the RT instability by computing the normalised square of the vertical velocity

$$\frac{\langle u_y^2(t)\rangle}{U_0^2} \equiv \frac{2}{L_xL_y} \int_0^{L_x} dx \int_{\frac{L_y}{4}}^{\frac{3L_y}{4}} u_y^2(t)dy, \tag{6.2}$$

with $U_0 = gh_0^2/\nu$ the natural velocity scale for this problem, which is shown in the red semi-log plot in figure 6(*c*). The blue semi-log plot in figure 6(*c*) shows the maximum scaled height $h(t)/h_0$ of the interface (the maximal deviation of the $\phi = 0$ contour line from the $t = 0$ interface position $L_y/2$). The linear regions in both semi-log plots in figure 6(*c*) are consistent with the exponential growth of the RT instability at early times.

For a CHNS-based study of the RT instability in three dimensions, we refer the reader to Gibbon *et al.* (2016*b*). This DNS study was designed to obtain $E_\infty(t)$ (5.3) by obtaining large-m estimates for the L^m norm of the energy $E(t)$ (5.2); and the results, based on
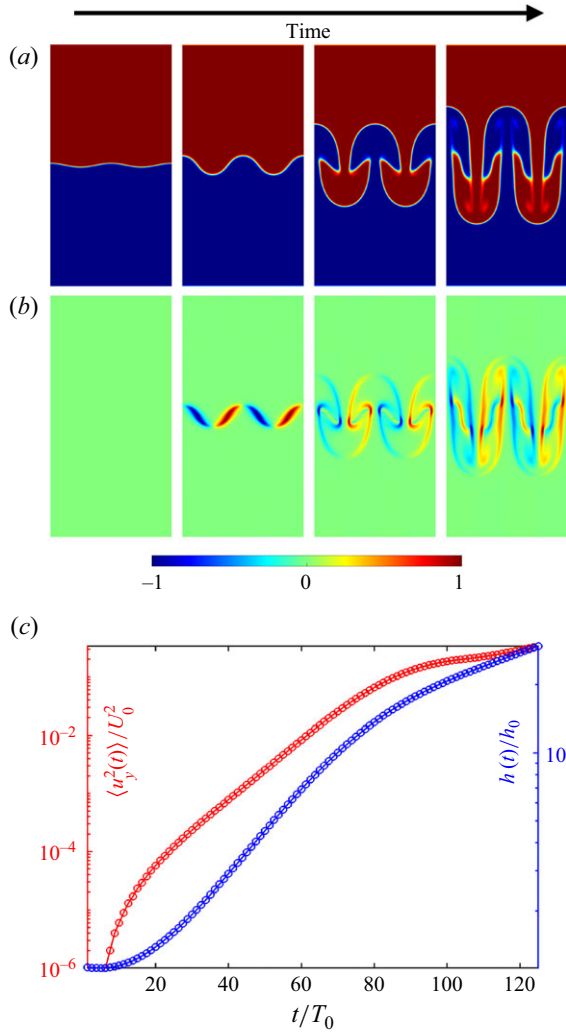
Figure 6. Rayleigh–Taylor instability in the 2-D CHNS system: pseudocolour plots of (*a*) the ϕ field and (*b*) the corresponding vorticity field at different times (increasing from left to right). (*c*) Semi-log plots versus the scaled time T/T_0 of $[\langle u_y^2(t)\rangle]/[U_0^2]$ (red) and the maximum scaled height $h(t)/h_0$ (blue) (see the text). The simulation box size is $(L_x, L_y) = (2\pi, 4\pi)$ with 512×1024 grid points; $\nu = 0.01$, $\alpha = 0$, $\sigma = 0.1$, $g = 1$, $\mathcal{A} = 0.6$, $\rho_0 = 1$, $h_0 = 0.1$ and $m = 2$. The characteristic velocity and time scales are $U_0 = gh_0^2/\nu$ and $T_0 \equiv h_0/U_0 = \nu/gh_0$. The simulation box is periodic in the x-direction; BCs in the y-direction are implemented by the volume-penalisation method (see the text).

the BKM-type criterion (5.4), were consistent with no finite-time singularity, given the resolution of the DNS runs.

6.2. *Kelvin–Helmholtz instability: CHNS (two dimensions)*

If there is a significant difference in the velocities of two fluid layers, which are separated by an interface, then this interface becomes unstable because of the well-known KH instability (see, e.g., Aref & Siggia 1981; Drazin 2002; Cushman-Roisin 2005; Charru 2011; Yilmaz *et al.* 2011; Lee & Kim 2015; Tian & Chen 2016; Hoshoudy & Cavus 2018; Budiana *et al.* 2020; Zhou, Dong & Li 2020; Delamere *et al.* 2021; Jia *et al.* 2023;
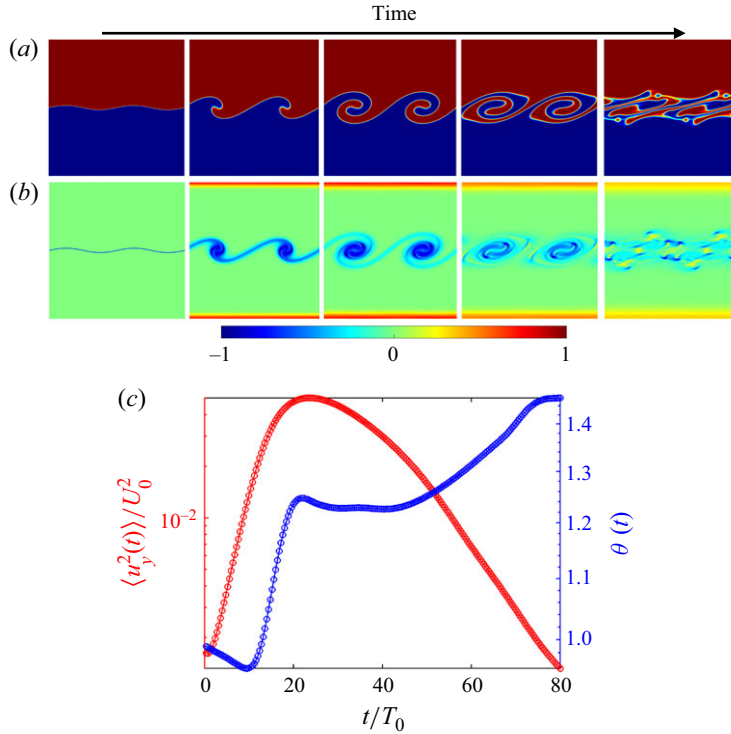
Figure 7. Our DNS of the KH instability in the 2-D CHNS system: pseudocolour plots of (*a*) the ϕ field and (*b*) the corresponding vorticity field at different simulation times (increasing from left to right); the vorticity field is normalised by its absolute maximum value. (*c*) Plots versus the scaled time t/T_0 of $[\langle u_y^2(t)\rangle]/[U_0^2]$ (red semi-log plot), where $T_0 \equiv h_0/U_0$, and $\theta(t)$ (blue linear plot) (see (6.4) and (6.5)). The simulation box size is $(L_x, L_y) = (2\pi, 2\pi)$ with 1024×1024 grid points; and $U_0 = 2$, $h_0 = 0.1$, $\nu = 0.01$, $\alpha = 0.01$, $\sigma = 0.05$, $g = 1$, $\mathcal{A} = 0.01$, $\rho_0 = 1$. The simulation box is periodic in the x-direction and we use volume penalization in the y-direction to incorporate solid boundaries; we incorporate impenetrable boundaries in the y-direction by using the volume-penalisation method, with 6 grid points on both the top and bottom boundaries for penalisation.

Kumar *et al.* 2023) that plays an important role in various marine, geophysical, solar and astrophysical processes (see, e.g., Mishin & Tomozov 2016; Gregg *et al.* 2018). The CHNS framework has been used to study KH instabilities in binary and ternary fluids (see Lee & Kim 2015). To illustrate how this is done, we perform a pseudospectral DNS of the CHNS equations within the Boussinesq approximation (3.5)–(3.6) in a 2-D box $(L_x, L_y) = (2\pi, 2\pi)$. Our simulation box is periodic in the x-direction and we incorporate solid boundaries in the y-direction by using the volume-penalisation method, where we consider six grid points on both the top and bottom sides for penalisation. We use the following stably stratified initial conditions, so that there is no RT instability:

$$\phi(x, y, 0) = \tanh\left[\frac{y - L_y/2 - h_0 \sin(2x)}{\epsilon/2}\right];$$
$$u_x(x, y, 0) = U_0\phi(x, y, 0);$$
$$u_y(x, y, 0) = 0. \tag{6.3}$$

In figures 7(*a*) and 7(*b*), we portray the ϕ and vorticity fields, respectively, via pseudocolour plots. We also quantify the temporal growth of the KH instability by computing the normalised square of the vertical velocity

$$\frac{\langle u_y^2(t) \rangle}{U_0^2} \equiv \frac{2}{L_x L_y} \int_0^{L_x} \mathrm{d}x \int_{\frac{L_y}{4}}^{\frac{3L_y}{4}} u_y^2(t) \mathrm{d}y, \tag{6.4}$$

which we plot versus the scaled time t/T_0 in figure 7(c) (red semi-log plot), where $T_0 \equiv h_0/U_0$; the limits on the integral over y are chosen to exclude the effects of the boundaries. The initial increase in $\langle u_y^2(t) \rangle / U_0^2$ signals the KH instability; this ratio decreases eventually because, in our DNS, the shear is present only in the initial condition. We also calculate the momentum thickness (Aref & Siggia 1981)

$$\theta(t) = \int_{\frac{L_y}{4}}^{\frac{3L_y}{4}} \mathrm{d}y \frac{\sqrt{\langle u_x^2(y, t) \rangle_x}}{\sqrt{\langle u_x^2(L_y/2, t) \rangle_x}}; \tag{6.5}$$

a linear plot of $\theta(t)$ versus the scaled time t/T_0 is shown in figure 7(c) (blue line).

6.3. *Phase separation in the binary-fluid CHNS*

A homogeneous binary-fluid mixture spontaneously phase separates into domains of pure phases when the system is quenched from a high temperature to a low temperature, which lies below the critical temperature T_c (see, e.g., Chaikin *et al.* 1995; Bray 2002; Puri & Wadhawan 2009); in equilibrium, pure phases are separated by an interface. If the order parameter is conserved, the early stages of phase separation proceed via nucleation or spinodal decomposition; thereafter, the system approaches the state with complete phase separation via the coarsening of domains of the pure phases (see § 2.2.2).

The CHNS framework has been used for studying the coarsening of phase-separating binary-fluid mixtures in both two and three dimensions (see, e.g., Berti *et al.* 2005; Perlekar, Pal & Pandit 2017; Wang *et al.* 2019). To study the coarsening process in a symmetric binary fluid mixture, we define the domain length scale $L(t)$ and integral length scale $L_I(t)$ in terms of the phase-field spectrum $S(k, t)$ and energy spectrum $E(k, t)$, respectively, as follows:

$$L(t) = 2\pi \frac{\sum\limits_k k^{-1} S(k, t)}{\sum\limits_k S(k, t)}; \qquad L_I(t) = 2\pi \frac{\sum\limits_k k^{-1} E(k, t)}{\sum\limits_k E(k, t)};$$

$$S(k, t) = \sum_{k-1/2 < k' < k+1/2} \left[\hat{\phi}(\mathbf{k}', t) \cdot \hat{\phi}(-\mathbf{k}', t) \right];$$

$$E(k, t) = \frac{1}{2} \sum_{k-1/2 < k' < k+1/2} \left[\hat{\boldsymbol{u}}(\mathbf{k}', t) \cdot \hat{\boldsymbol{u}}(-\mathbf{k}', t) \right]. \tag{6.6}$$

The length scale $L(t)$ displays self-similar power-law growth with $L(t) \sim t^\beta$: (i) in the diffusion-dominated regime (governed by the CH equation) $\beta \simeq 1/3$, the well-known Lifshitz–Slyozov exponent (see, e.g., Lifshitz & Slyozov 1961; Bray 2002; Puri & Wadhawan 2009); (ii) in the viscous-hydrodynamic regime, $\beta \simeq 1$ (see Siggia 1979; Perlekar *et al.* 2014); and (iii) in the inertia-dominated regime, $\beta \simeq 2/3$ (Furukawa 2000).

We carry out an illustrative pseudospectral DNS of the CHNS (two dimensions) equations to obtain the scaling exponent $\beta \simeq 2/3$ in the inertial-hydrodynamic regime. We illustrate domain coarsening by the pseudocolour plots of ϕ and ω in figures 8(a) and 8(b). The power-law growth of $L(t)$ and $L_I(t)$, in the low-viscosity inertial regime, is shown in figure 8(c); the growth of both these lengths is consistent with the same power-law
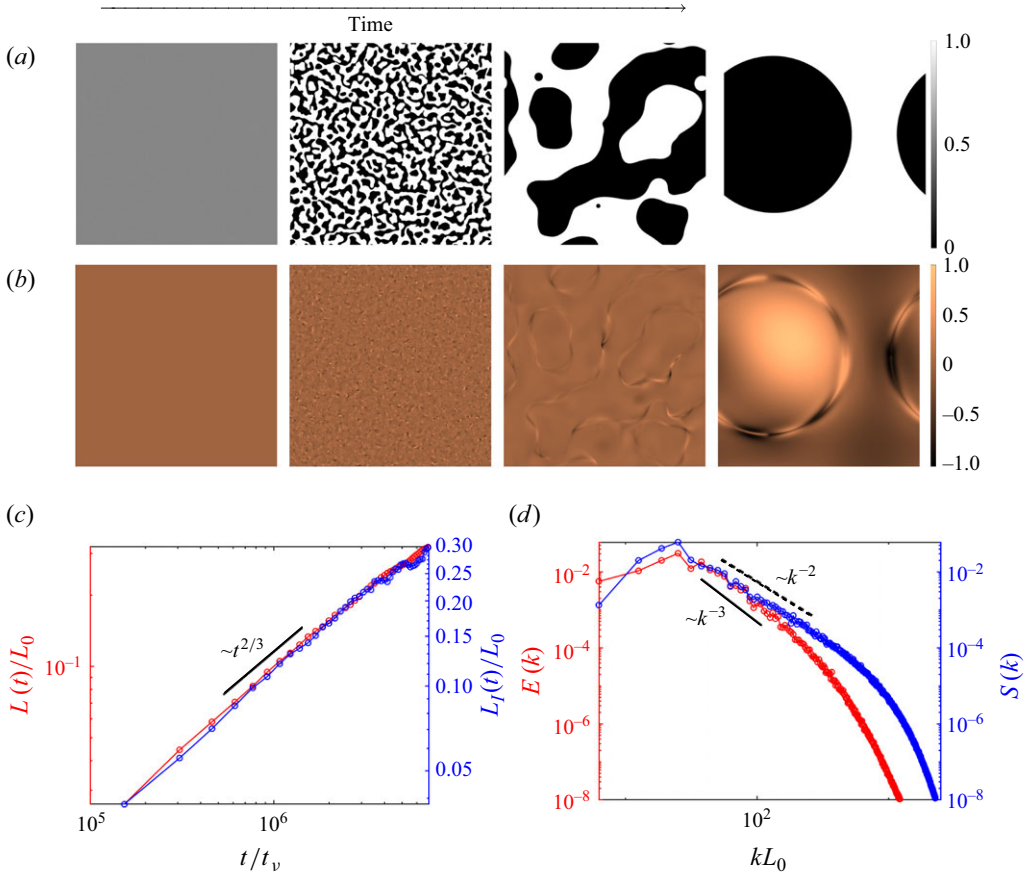
Figure 8. Coarsening in a binary-fluid mixture from our DNS of the 2-D CHNS equations. (*a*) Pseudogreyscale plots of the phase-field $\phi(\mathbf{x}, t)$ at simulation times $t = 0, 0.24, 5.52 (\equiv t_*), 8.88$, increasing from left to right; (*b*) pseudocolour plots of the corresponding vorticity fields $\omega(\mathbf{x}, t)$ (normalised by their absolute maximum for ease of visualisation). (*c*) Log–log plots versus t/t_ν, with $t_\nu = \nu^3/\sigma^2$, of the scaled lengths $L(t)/L_0$ (red) and $L_I(t)/L_0$ (blue), with $L_0 = 2\pi$ the side of the simulation domain. (*d*) The energy spectrum (red line) $E(k, t = t_*)$ and the phase-field spectrum (blue line) $S(k, t = t_*)$ show power-law behaviour with scaling exponents $\sim k^{-3}$ and $\sim k^{-2}$, respectively.

exponent $\beta \simeq 2/3$. We show the energy spectrum and phase-field spectrum in figure 8(*d*); $E(k) \sim k^{-3}$ (consistent with the scaling exponent obtained in 2-D turbulence (Boffetta & Ecke 2012)) and $S(k) \sim k^{-2}$ (consistent with the results obtained by Furukawa (2000)). We solve the 2-D CHNS equations via a pseudospectral DNS in a doubly periodic box of size $2\pi \times 2\pi$ with grid points 1024×1024. The relevant dimensionless numbers are the Reynolds number $Re = u_{rms} L_I/\nu$ and the Ohnesorge number $Oh = \nu(\rho/\sigma L_I)^{1/2}$. The simulation parameters are $\nu = 5 \times 10^{-3}$, $\sigma = 0.4$, $\rho = 1$, $\epsilon = 0.018$ and $M = 10^{-4}$. The dimensionless numbers, calculated at $t = t^*$ (see figure 8), are $Re = 24$ and $Oh = 0.01$.

Fluid turbulence can mix immiscible fluids and lead to the arrest of phase separation, which is also referred to as coarsening arrest. The CHNS PDEs have been used to study such turbulence-induced coarsening arrest in both two dimensions and three dimensions (see, e.g., Perlekar *et al.* 2014, 2017). If parameters are chosen such that the CH equations lead to complete phase separation of the two fluids in the binary mixture, then the inclusion of turbulence, obtained by forcing the coupled CHNS equations, suppresses this phase

separation. This can be characterised by using the lengths and spectra that we have defined in (6.6). In the absence of turbulence, the spectrum $S(k, t)$ displays an inverse cascade to small wavenumbers k as time t increases; this leads to the power-law growth of $L_I(t)$ as $t \to \infty$, with the Lifshitz–Slyozov, viscous-hydrodynamic and inertial-hydrodynamic exponents mentioned above. This inverse cascade and the associated power-law growth of $L_I(t)$ are arrested by turbulence. In particular, it has been shown (see the pseudospectral DNS of Perlekar *et al.* (2017) and the Lattice–Boltzmann study of Perlekar *et al.* (2014) in two dimensions and three dimensions, respectively), which $L_I(t) \sim L_H$ as $t \to \infty$, where the Hinze length scale $L_H \sim \varepsilon_{inj}^{-2/5} \sigma^{3/5}$, with ε_{inj} the energy injection into the NS part of the CHNS system. We will show in § 7.8 that active turbulence, which occurs in the active-CHNS system, also leads to qualitatively similar coarsening arrest.

6.4. *Spatiotemporal evolution of antibubbles*

A shell of a low-density fluid inside a high-density fluid is known as an antibubble. It seems to have been described first by Hughes and Hughes (see, e.g., Hughes & Hughes 1932; Dorbolo *et al.* 2006; Kim & Vogel 2006; Kalelkar 2017; Vitry *et al.* 2019; Pal *et al.* 2022; Zia *et al.* 2022). An antibubble has two surfaces, and a certain volume of fluid is trapped between these two surfaces. Clearly, an antibubble is unstable under gravity: if the fluid in its inner core is denser than that in the outer core, the antibubble rises; and the fluid in the shell forms a bulb at the top while its bottom thins until the shell collapses completely. For experimental investigations of the dynamics of an antibubble, see, for example, Dorbolo *et al.* (2006), Kim & Vogel (2006), Vitry *et al.* (2019) and Zia *et al.* (2022); and for theoretical work consult, for example, Scheid *et al.* (2012), Zou *et al.* (2013), Sob'yanin (2015) and Pal *et al.* (2022). It is important to note that the inherent instability of antibubbles makes experimental studies challenging; in some cases surfactant molecules have to be introduced to obtain some stabilisation of an antibubble. Furthermore, antibubbles have several applications that include sonoporation (see, e.g., Kotopoulis *et al.* 2014), drug delivery (see, e.g., Johansen *et al.* 2015a); Kotopoulis *et al.* 2015) and active leakage detection (see, e.g., Johansen *et al.* 2015b).

It was recognised by Pal *et al.* (2022) that the CHNS system provides an ideal theoretical framework for the elucidation of the spatiotemporal evolution of antibubbles. The initial condition for ϕ is an annulus in two dimensions or a shell in three dimensions of the lighter fluid (shown in red) with the heavier fluid (shown in blue) both inside and outside the shell. The initial outer and inner radii of the shell are, respectively, R_0 and R_1, and h_0 is the initial thickness of the antibubble shell, so it is natural to define the Bond number *Bo* with L_0 replaced by h_0 (see table 2). The spatiotemporal evolution of such an antibubble in the 2-D CHNS system is shown via pseudocolour plots of ϕ in figures 9(*a*) and 9(*c*) at representative times; the associated evolution of the vorticity ω is given, respectively, in figures 9(*b*) and 9(*d*). (These figures have been provided very kindly by N. Pal.) From figures 9(*a*) and 9(*c*) we see that gravity induces a thinning of the bottom of the antibubble while forming a slight dome on the top of it; eventually this makes the antibubble rupture. A similar rupture also occurs for antibubbles in the 3-D CHNS system (see Pal *et al.* 2022 for details). These DNSs yield the scaled rupture time τ_1/τ_g, with $\tau_g \equiv \sqrt{R_0/\mathcal{A}g}$, the velocity v_{rim} of the retracting rim of the collapsing antibubble, and they find that $v_{rim} \sim \sqrt{\sigma}$, in agreement with the theoretical estimate of Sob'yanin (2015) and experiments of Scheid *et al.* (2012) and Zou *et al.* (2013). Furthermore, this CHNS study (Pal *et al.* 2022) obtains the dependence of τ_1/τ_g on the Bond number *Bo* and shows, by obtaining the energy ($E(k)$) and concentration ($S(k)$) spectra, that the rupture of the antibubble leads to some turbulence. Finally Pal *et al.* (2022) provide a comparison of
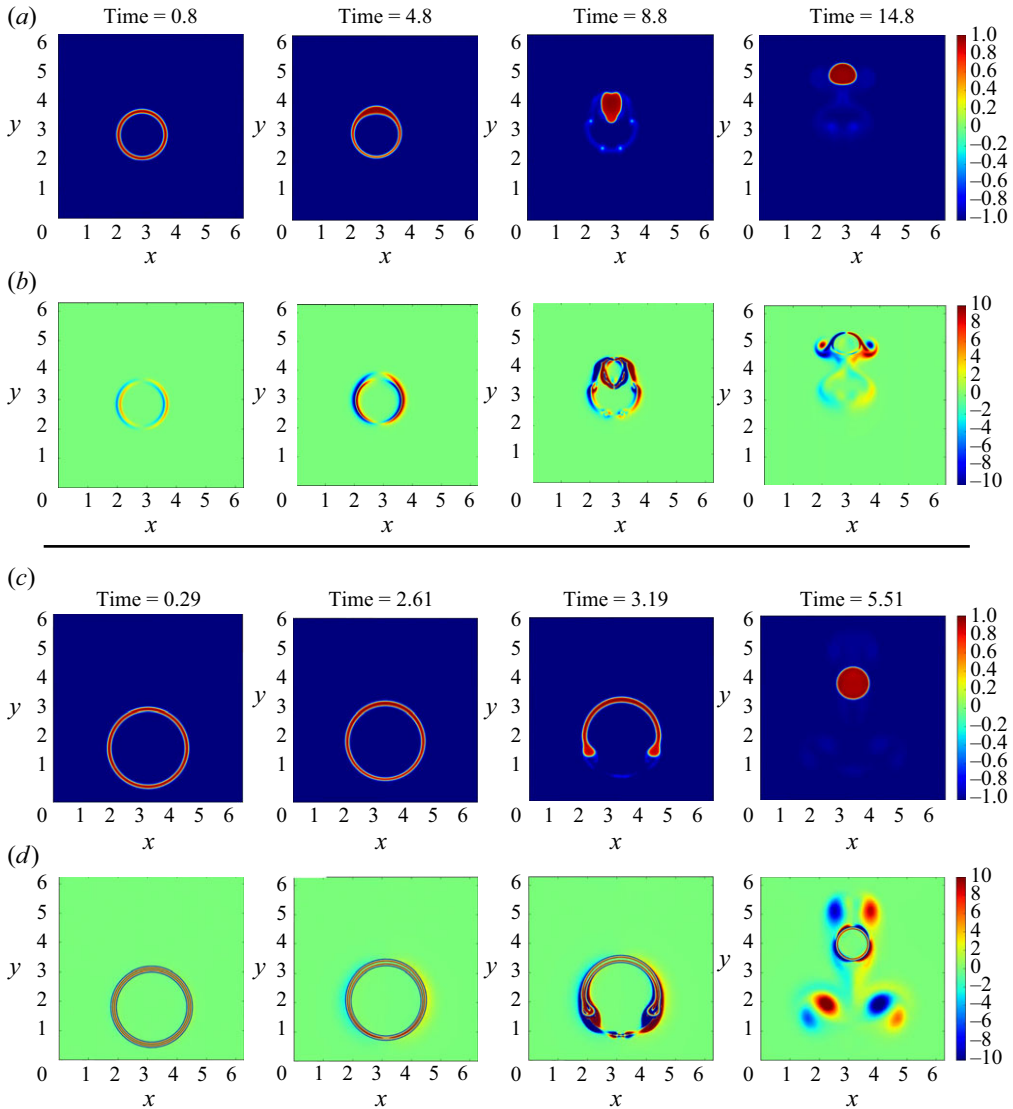
Figure 9. Illustrative pseudocolour plots of (*a*) and (*c*) the field ϕ and the associated plots of the vorticity ω showing the spatiotemporal evolution of antibubbles for low (*a*) and (*b*) and high (*c*) and (*d*) values of R_0 and R_1, the initial outer and inner radii of the shell of the antibubble (see the text and Pal *et al.* (2022) for details). We thank N. Pal for these figures.

the spatiotemporal evolution of antibubbles by using both the CHNS framework and a VOF DNS.

6.5. *Low-Reynolds-number interface-induced turbulence in the CHNS system*

Emergent turbulence-type states have been found at low Reynolds numbers in a variety of systems, for instance, in fluids with polymer additives (see, e.g., Groisman & Steinberg 2000; Majumdar & Sood 2011; Gupta & Pandit 2017; Benzi & Ching 2018; Steinberg 2021; Singh *et al.* 2024) and in dense bacterial suspensions (see, e.g., Wensink *et al.* 2012; Dunkel *et al.* 2013; Bratanov, Jenko & Frey 2015; Linkmann *et al.* 2019; Alert, Casademunt

& Joany 2021; Kiran *et al.* 2023; Mukherjee *et al.* 2023). In the former, this turbulence is driven by an increase in the Weissenberg number, whereas in the latter, it is obtained by increasing the activity of the bacterial suspension. Recently Padhan *et al.* (2024*b*) have demonstrated that low-*Re* turbulence occurs in the 2-D CHNS system if we increase the Weber number *We* or the Capillary number *Ca* (i.e. we decrease the interfacial tension; see table 2) and hence enhance interfacial fluctuations.

To obtain such interface-induced turbulence, Padhan *et al.* (2024*b*) begin with a periodic arrangement of vortices and antivortices, which is referred to as a vortex crystal or a cellular flow. Such cellular flows, imposed by a spatially periodic forcing with an amplitude f_0 and wavenumber k_f, can be disordered via turbulence as shown for 2-D fluid turbulence by Perlekar & Pandit (2010) and for 2-D fluids with polymer additives by Gupta & Pandit (2017) and Plan *et al.* (2017). For the 2-D CHNS system, we follow the discussion of Padhan *et al.* (2024*b*) and examine the dependence of the statistically steady state of the system as we increase the Capillary number *Ca*. The natural length, time, and velocity scales are, respectively, k_f^{-1}, $\nu k_f/f_0$ and $U \equiv f_0/(\nu k_f^2)$.

In figures 10(*a*) and 10(*e*) we plot the scaled total kinetic energy $e(t)/e_0$ versus time t, with $e_0 = U^2$; figures 10(*b*) and 10(*f*) display the corresponding power spectra $|\tilde{e}(f)|$ of $e(t)/e_0$. Figures 10(*c*) and 10(*g*) depict pseudocolour plots of the vorticity ω overlaid with the $\phi = 0$ contour (black lines) at a representative time. In figures 10(*d*) and 10(*h*) we present pseudocolour plots of the energy spectra $\mathcal{E}(k_x, k_y)$ at a representative time; these spectra are not averaged over wavenumber shells because the underlying crystalline state is not isotropic. Figures 10(*a*–*e*) and 10(*f*–*j*) help us to distinguish between states that are temporally periodic ($Ca = 0.17$) from those that are chaotic ($Ca = 0.19$); figures 10(*k*–*o*) and 10(*p*–*t*) aid the identification of the spatial order of the state. If the state is periodic in space, $\mathcal{E}(k_x, k_y)$ shows Bragg peaks in the reciprocal lattice of the vortex crystal (e.g., the strong red peaks in figure 10*h*), where we use the standard terminology of crystal physics. We find a rich variety of states: STPO, spatially and temporally periodic (i.e. a spatiotemporal crystal of the type discussed in Perlekar & Pandit (2010) and Gupta & Pandit (2017)); STPOG, is like STPO, but with a grain boundary separating two crystalline parts; STC denotes spatiotemporal chaos. Here, TPO denotes temporally periodic oscillations. For similar states in studies of turbulence-induced melting of a vortex crystals see Perlekar & Pandit (2010) for fluids and Gupta & Pandit (2017) for fluids with polymer additives. In the latter case, the melting of the vortex crystal can be induced by elastic turbulence at low *Re*; this is akin to the low-*Re* interface-fluctuation-induced melting we discuss here. In particular, the study of Gupta & Pandit (2017) has noted that the boundary between spatially and temporally periodic states and ones that exhibit STC is non-monotonic, i.e. there is re-entrance from one state into another and back. Interface-induced turbulence in the 2-D CHNS system also displays such re-entrance, as a function of *Ca*; Padhan *et al.* (2024*b*) have found the following re-entrant sequence of states: chaotic→temporally periodic→chaotic.

7. Beyond binary-fluid CHNS: challenging problems

We now discuss some illustrative examples that go beyond the use of the binary-fluid CHNS PDEs that we have considered so far. In particular, we consider three-fluid flows, at low and high Reynolds numbers, and the active-CHNS PDEs that have been used, *inter alia*, to model scalar active turbulence. Section 7.1 outlines the CHNS framework for a ternary-fluid mixture; we give the Boussinesq approximation for this case in § 7.1.1. In § 7.2 we describe how the CHNS framework can be used to study phase separation, and its turbulence-induced suppression, in ternary-fluid mixtures. Section 7.3
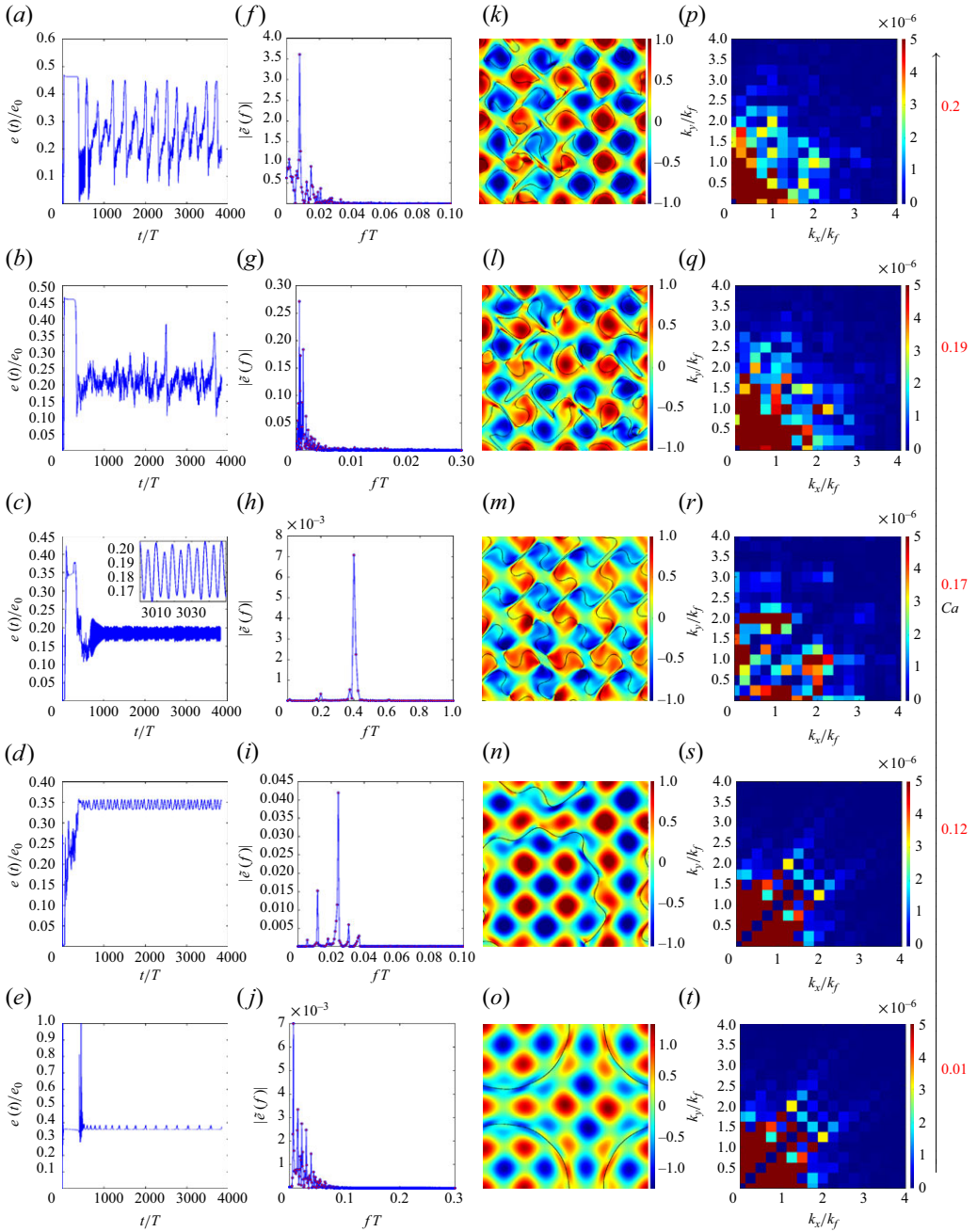
Figure 10. (*a–e*) The scaled total kinetic energy $e(t)/e_0$ versus time t [here, $e_0 = U^2$ and $U = f_0/(\nu k_f^2)$]; (*f–j*) the corresponding power spectra $\tilde{e}(f)$ of $e(t)/e_0$. Pseudocolour plots, at a representative time, of (*k–o*) the vorticity ω overlaid with the $\phi = 0$ contour (black lines) and (*p–t*) the energy spectra $\mathcal{E}(k_x, k_y)$ (see Padhan, Vincenzi & Pandit 2024*b* for details); the capillary number Ca increases from 0.01 in the bottom row to 0.2 in the top row.
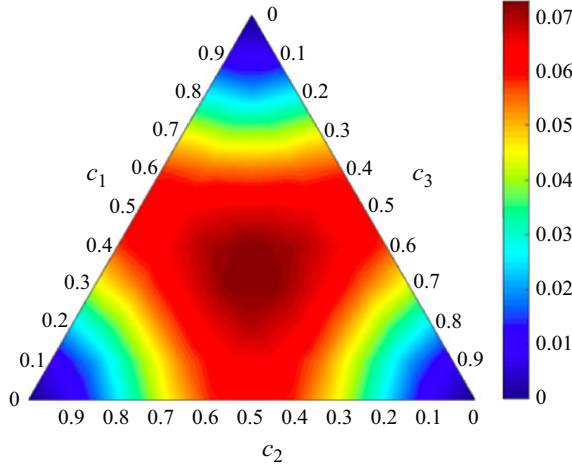
Figure 11. Pseudocolour plot of $F(\{c_i\})$ projected onto a Gibbs triangle for the CHNS3 model (7.1). The three vertices yield the three minima of $F(\{c_i\})$: the top vertex is $(c_1, c_2, c_3) = (1, 0, 0)$; the left-hand vertex is $(c_1, c_2, c_3) = (0, 1, 0)$; the right-hand vertex is $(c_1, c_2, c_3) = (0, 0, 1)$.

contains an examination of the spatiotemporal evolution of droplets and compound droplets in turbulent flows. Section 7.4 discusses the passage of a bubble of one phase through the interface between two other fluid phases. In Section 7.5 we show how the CHNS framework allow us to study the coalescence of liquid lenses and droplets quantitatively. Section 7.6 introduces the active-CHNS model (also called active Model H). Sections 7.8 and 7.9 are devoted, respectively, to turbulence in the active CHNS system and activity-induced droplet propulsion in the generalised active CHNS model (7.24)–(7.29).

7.1. *Ternary-fluid CHNS*

The CHNS3 model for a ternary-fluid mixture uses the following variational free energy in the domain Ω (see, e.g., Boyer & Lapuerta 2006; Kim 2007; Boyer *et al.* 2010; Shek & Kusumaatmaja 2022*a*; Padhan & Pandit 2023*b*):

$$\mathcal{F}(\{c_i, \nabla c_i\}) = \int_\Omega \mathrm{d}\Omega \left[\frac{12}{\epsilon} F(\{c_i\}) + \frac{3\epsilon}{8} \sum_{i=1}^{3} \gamma_i (\nabla c_i)^2 \right], \tag{7.1}$$

where the concentration fields $c_i\,(i = 1, 2, 3)$ are conserved order parameters that satisfy the constraint $\sum_{i=1}^{3} c_i = 1$, ϵ is the thickness of the interface, the variational bulk free energy

$$F(\{c_i\}) = \sum_{i=1}^{3} \gamma_i c_i^2 (1 - c_i)^2, \tag{7.2}$$

and the gradient terms give the surface-tension penalties for interfaces, with

$$\sigma_{ij} = (\gamma_i + \gamma_j)/2 \tag{7.3}$$

the bare surface (or interfacial) tension for the interface between the phases i and j; the equilibrium values of c_i follow from the global minima of $F(\{c_i\})$. In figure 11, we show a pseudocolour plot of $F(\{c_i\})$ projected onto a Gibbs triangle (see, e.g., Kim 2007).

The equilibrium chemical potential of fluid-i is $\mu_i = (\delta\mathcal{F}/\delta c_i) + \beta(c_i)$, with $\beta(c_i)$ the Lagrange multiplier that ensures $\sum_{i=1}^{3} c_i = 1$, whence we get

$$\mu_i = -\frac{3}{4}\epsilon\gamma_i\nabla^2 c_i + \frac{12}{\epsilon}\left[\gamma_i c_i(1-c_i)(1-2c_i)\right.$$
$$\left. -\frac{6\gamma_1\gamma_2\gamma_3(c_1 c_2 c_3)}{\gamma_1\gamma_2 + \gamma_1\gamma_3 + \gamma_2\gamma_3}\right]. \tag{7.4}$$

The incompressible CHNS3 equations can be written as follows (see, e.g., Kim & Lowengrub 2005; Boyer *et al.* 2010; Tóth, Zarifi & Kvamme 2016; Padhan & Pandit 2023*b*):

$$\rho(\{c_i\})(\partial_t \boldsymbol{u} + (\boldsymbol{u} \cdot \nabla)\boldsymbol{u}) = -\nabla P + \nabla \cdot \left[\eta(\{c_i\})(\nabla\boldsymbol{u} + \nabla\boldsymbol{u}^T)\right]$$
$$-\sum_{i=1}^{3} c_i \nabla\mu_i + \rho(\{c_i\})\boldsymbol{g} - \alpha\boldsymbol{u} + \boldsymbol{f}^{ext};$$
$$\nabla \cdot \boldsymbol{u} = 0;$$
$$\partial_t c_i + (\boldsymbol{u}.\nabla)c_i = \frac{M}{\gamma_i}\nabla^2\mu_i, \quad i = 1 \text{ or } 2;$$
$$\eta(\{c_i\}) = \sum_{i=1}^{3} \eta_i c_i;$$
$$\rho(\{c_i\}) = \sum_{i=1}^{3} \rho_i c_i. \tag{7.5}$$

Here, $\boldsymbol{g}$, $\boldsymbol{f}^{ext}$ and α are, respectively, the acceleration because of gravity, an external forcing, and the coefficient of friction. η_i and ρ_i are the viscosity and density of fluid i, respectively. The CHNS3 model becomes the binary-fluid CHNS model for $(c_1, c_2, c_3) = (c, 0, 0)$.

7.1.1. *Boussinesq approximation*
If we use the Boussinesq approximation, the CHNS3 equations can be written as follows:

$$\partial_t \boldsymbol{u} + (\boldsymbol{u} \cdot \nabla)\boldsymbol{u} = -\frac{1}{\rho_0}\nabla P + \nu\nabla^2\boldsymbol{u} - \frac{1}{\rho_0}\sum_{i=1}^{3}(c_i \nabla\mu_i) + \frac{[\rho(\{c_i\}) - \rho_0]}{\rho_0}\boldsymbol{g} - \alpha\boldsymbol{u}, \tag{7.6}$$

$$\nabla \cdot \boldsymbol{u} = 0. \tag{7.7}$$

We write the density in the form

$$\rho(\{c_i\}) = \sum_{i=1}^{3} \rho_i c_i$$
$$= \rho_1 c_1 + \rho_2 c_2 + \rho_3(1 - c_1 - c_2)$$
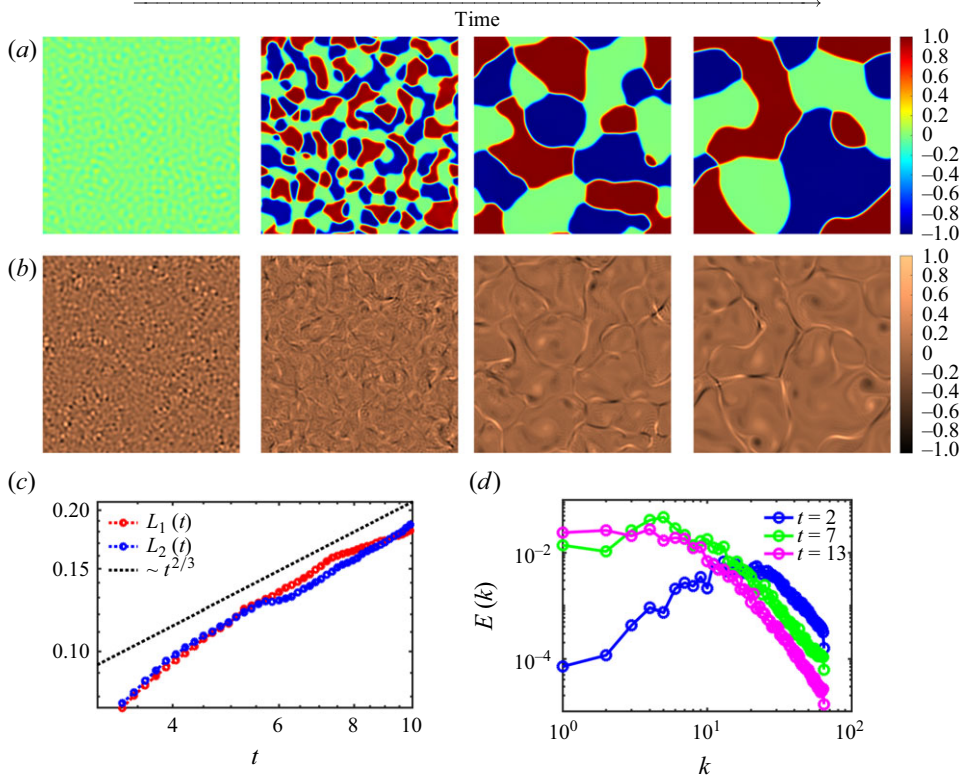$$= \rho_3 + (\rho_1 - \rho_3)c_1 + (\rho_2 - \rho_3)c_2; \tag{7.8}$$

Figure 12. Coarsening in a ternary-fluid mixture from our DNS of the 2-D CHNS3 equations. (*a*) Pseudocolour plots of the phase-fields $c_2 - c_1$ at simulation times $t = 0.8, 2, 7, 13$, increasing from left to right. (*b*) Pseudocolour plots of the corresponding vorticity fields $\omega(\boldsymbol{x}, t)$ (normalised by their absolute maximum for ease of visualisation). (*c*) Log–log plots versus t of the scaled lengths $L_1(t)/L_0$ and $L_2(t)/L_0$, with $L_0 = 2\pi$ the side of the simulation domain. (*d*) The energy spectrum $E(k, t)$ at simulation times $t = 2, 7, 13$. Simulation parameters: viscosity $\nu = 10^{-3}$; grid points 256×256; surface tension coefficients $(\sigma_{12}, \sigma_{23}, \sigma_{13}) = (1, 1, 1)$.

we use $\rho_0 = \rho_3$, so

$$
\frac{[\rho(\{c_i\}) - \rho_0]}{\rho_0} = \left(\frac{\rho_1 - \rho_3}{\rho_0}\right) c_1 + \left(\frac{\rho_2 - \rho_3}{\rho_0}\right) c_2
$$
$$
= \mathcal{A}_1 c_1 + \mathcal{A}_2 c_2, \tag{7.9}
$$

where $\mathcal{A}_1$ and $\mathcal{A}_2$ are the Atwood numbers and $\mathcal{A}_1, A_2 \ll 1$.

7.2. *Phase separation in the ternary-fluid CHNS3*

We turn now to the phase separation of ternary-fluid mixtures that occurs in a variety of settings (see, e.g., Huang, de La Cruz & Swift 1995; Singh *et al.* 2015*a*; Wang *et al.* 2019; Shek & Kusumaatmaja 2022*b*). In figure 12, we show illustrative results for coarsening in such a mixture, from our DNS of the 2-D CHNS3 equations, which we visualise via pseudocolour plots of the difference of the phase-fields $(c_2 - c_1)$ (figure 12*a*) and the corresponding vorticity fields $\omega(\boldsymbol{x}, t)$, normalised by their absolute maximum (figure 12*b*), at simulation times $t = 0.8, 2, 7, 13$, which increase from left to right. We define the following scaled lengths (cf. (6.6) for the two-fluid CHNS):

$$L_1(t) = 2\pi \frac{\sum\limits_{k} S_1(k, t)}{\sum\limits_{k} k S_1(k, t)}; \qquad L_2(t) = 2\pi \frac{\sum\limits_{k} S_2(k, t)}{\sum\limits_{k} k S_2(k, t)}. \tag{7.10}$$

The scaled lengths $L_1(t)/L_0$ and $L_2(t)/L_0$, with $L_0 = 2\pi$, increase with time, in a manner that is consistent with $\sim t^{2/3}$, the power-law growth for the inertia-dominated regime (see the log–log plot in figure 12c). This power-law growth has also been seen in the molecular-dynamics simulations of Singh & Puri (2015a). We expect that such ternary-fluid phase separation will also be suppressed by turbulence in the CHNS3 equations, just as turbulence leads to coarsening arrest in the binary-fluid case (see, e.g., Perlekar *et al.* 2014, 2017), but we must account for additional non-dimensional control parameters such as the ratios of the surface tensions between the three fluid phases that coexist in equilibrium. To the best of our knowledge, a complete study of such turbulence-induced coarsening arrest in three-phase fluid mixtures has not been carried out so far.

7.3. *Spatiotemporal evolution of droplets in turbulent flows*

We follow and generalise, to the case of compound droplets, the investigation of the spatiotemporal evolution of droplets in binary-fluid turbulent flows by Pal *et al.* (2016), who studied the advection of a droplet, initially circular with a diameter d_0, by a turbulent binary-fluid flow for which they used the CHNS system in two dimensions. The droplet was active, insofar as it affected the flow, and was, in turn, deformed by the flow. Pal *et al.* (2016) obtained the acceleration components of the droplet centre of mass and showed that their probability distribution function (PDF) had wide, non-Gaussian tails. They uncovered multifractal fluctuations in the time series of the scaled perimeter (see below) of the droplet. Finally they showed that the droplet fluctuations led to an enhancement of the energy spectrum $E(k)$ for large wave numbers k, and thence to dissipation reduction, as in fluid turbulence with polymer additives (see, e.g., Perlekar, Mitra & Pandit 2006; Perlekar, Mitra & Pandit 2010; Gupta, Perlekar & Pandit 2015). We refer the reader to Pal *et al.* (2016) for the details of their DNS. Our investigations of a compound droplet are motivated by studies of compound droplets in external electric fields (see Santra *et al.* 2020), the examination of the breakup of double-emulsion droplets in linear flows (see Stone & Leal 1990), the numerical and theoretical investigations of the dynamics of a compound vesicle (a lipid bilayer membrane enclosing a fluid with a suspended particle) in a shear flow (see Veerapaneni *et al.* 2011) and a compound vesicle in shear flow (see Sinha & Thaokar 2019). Experiments have also suggested that a compound droplet can be used as a model for a white-blood cell (see Levant & Steinberg 2014). Furthermore, the deformation and breakup of a compound droplet has been studied in a 3-D oscillatory shear flow (see Liu *et al.* 2021) and in a channel flow (see Lanjewar & Ramji 2024).

We now give illustrative results for the turbulent advection of a simple droplet, initially circular with a radius R_0, and for a compound droplet, initially concentric circles with inner and outer radii R_{in} and R_{out}; for the former we employ the binary-fluid CHNS in two dimensions; and for the latter we use the 2-D ternary-fluid CHNS; in both cases we impose periodic BCs, obtain statistically steady turbulence via a Kolmogorov-type forcing with amplitude F_0, as in Pal *et al.* (2016), and a forcing wavenumber k_f that yields an energy spectrum in which the forward-cascade regime is dominant. The pseudocolour plots in figure 13(a) show the phase field ϕ, for a simple droplet, at different representative times, which increase from left to right. For the compound droplet we present pseudocolour plots of $(c_2 - c_1)$ with the radius ratios (b) $R_{in}/R_{out} = 0.5$ (figure 13b,c) $R_{in}/R_{out} = 0.9$ (figure 13c).
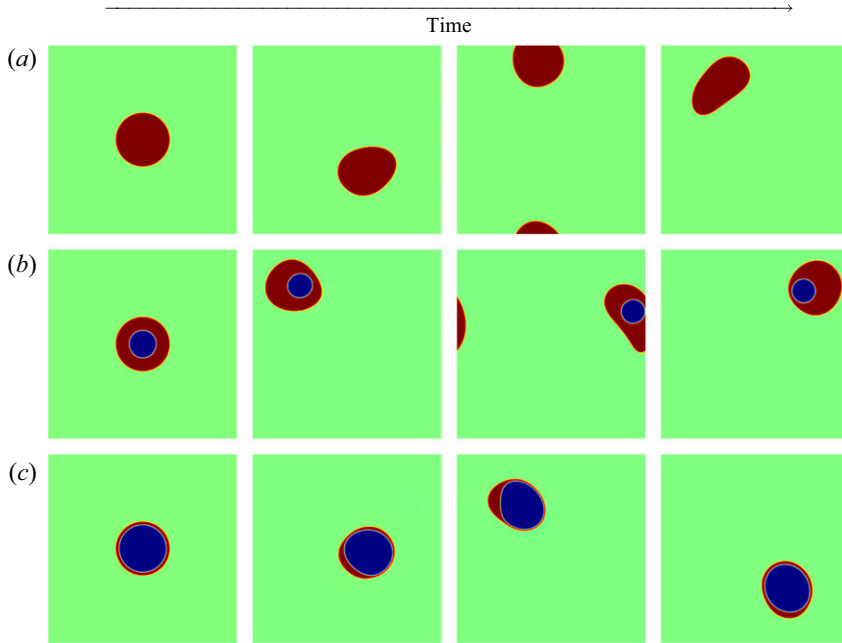
Figure 13. The pseudocolour plots of (*a*) the phase field c_2 for a simple droplet, and the phase field $c_2 - c_1$ for the compound droplets with radius ratios (*b*) $R_{in}/R_{out} = 0.5$ and (*c*) $R_{in}/R_{out} = 0.9$.

To characterise droplet fluctuations, we use the time dependence of the deformation parameter defined in Pal *et al.* (2016),

$$\Gamma(t) = \frac{\mathcal{S}(t)}{\mathcal{S}_0(t)} - 1, \qquad (7.11)$$

with $\mathcal{S}(t)$, the perimeter of the droplet, and $\mathcal{S}_0(t)$, the perimeter of an undeformed droplet. In the binary-fluid case we track the perimeter via the $\phi = 0$ contour; in the ternary-fluid case we use the contours $c_1 = 0.5$ and $c_2 = 0.5$ for the perimeters of the inner and outer droplets, respectively. The strength of the non-dimensionalised forcing is given by the Grashof number $Gr = L^4 F_0/\nu^2$; and the forcing-scale Weber number $We \equiv \rho k_f^{-3} F_0/\sigma$ measures the non-dimensionalised inverse surface tension; these parameters are chosen such that the droplets are not torn asunder during our DNSs. In figure 14(*a*) we plot $\Gamma(t)$ versus time (scaled by the forcing time scale $T = \nu k_f/F_0$) for a simple droplet (red line) and compound droplets with radius ratios $R_{in}/R_{out} = 0.5$ (green line) and $R_{in}/R_{out} = 0.9$ (blue line). In figures 14(*b*) and 14(*c*) we plot, respectively, the PDF of Γ and the multi-fractal spectrum $D(h)$ of the time series $\Gamma(t)$. From figures 14(*a*) and 14(*c*) we clearly see that the temporal fluctuations Γ, its PDF and its multifractal spectrum $D(h)$ are similar for simple droplet interface and outer droplet interface in the compound droplet with a radius ratio $R_{in}/R_{out} = 0.5$. By contrast, all these measures are reduced for the perimeter of the outer droplet interface in a compound droplet with a radius ratio $R_{in}/R_{out} = 0.9$ because the fluctuations of the outer interface are constrained by the presence of the inner droplet.

The energy spectra $E(k)$ for a single-phase turbulent fluid, a binary fluid with a simple droplet and a ternary fluid with a compound droplet (with radius ratios $R_{in}/R_{out} = 0.5$ and $R_{in}/R_{out} = 0.9$) are given in figure 14(*d*). These spectra show that droplet fluctuations, of both single and compound droplets, enhance $E(k)$ at large k, relative to its counterpart for single-fluid turbulence. This enhancement is reminiscent of a similar enhancement of $E(k)$
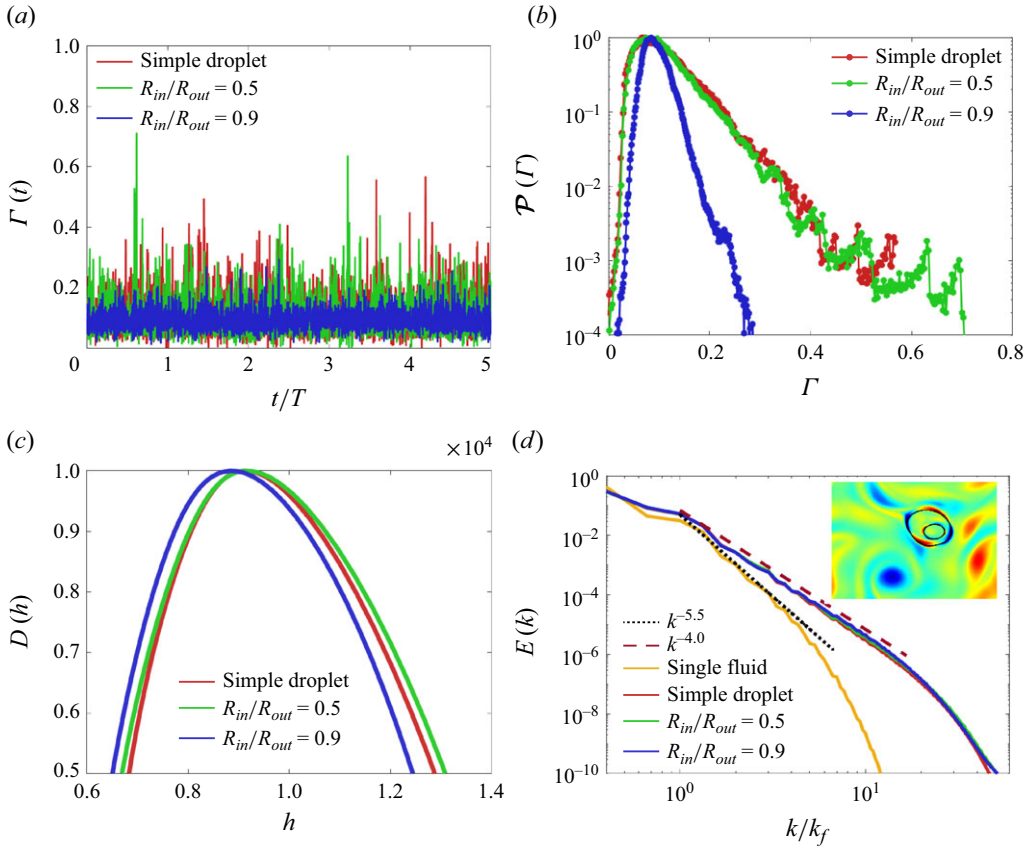
Figure 14. (*a*) Plot versus time of the deformation parameter $\Gamma(t)$ for a simple droplet (red line) and compound droplets with radius ratios $R_{in}/R_{out} = 0.5$ (green line) and $R_{in}/R_{out} = 0.9$ (blue line); the horizontal axis is scaled by the forcing time scale $T = \nu k_f / f_0$. The corresponding (*b*) PDFs of Γ (semi-log plots) and (*c*) the multifractal spectra $D(h)$ of Γ. (*d*) Log–log plots of the energy spectrum $E(k)$ for a single-phase turbulent fluid, a binary fluid with a simple droplet, and a ternary fluid with a compound droplet (with radius ratios $R_{in}/R_{out} = 0.5$ and $R_{in}/R_{out} = 0.9$); the inset shows a pseudocolour plot of the vorticity in the presence of a compound droplet.

in fluid turbulence by polymer additives, where it is associated with dissipation reduction can be understood as a k-dependent correction to the viscosity (see Perlekar *et al.* 2010; Gupta *et al.* 2015). Such a scale-dependent correction to the viscosity also occurs for a single droplet in a turbulent flow as has been discussed by Pal *et al.* (2016).

7.4. *Bubble passing through an interface between two fluids*

How do bubbles or droplets pass through an interface between two fluids? This problem has attracted considerable attention (see, e.g., Manga & Stone 1995; Dietrich *et al.* 2008; Bonhomme *et al.* 2012; Li *et al.* 2014; Natsui *et al.* 2014; Singh & Bart 2015; Feng *et al.* 2016; Prosperetti 2017; Emery, Raghupathi & Kandlikar 2018; Emery & Kandlikar 2019; Kumar, Rohilla & Das 2019; Choi & Park 2021; Chowdhury, Mahapatra & Sen 2022; Rabbani & Ray 2024) in the fluid dynamics, chemical engineering and microfluidics literature. Modern experiments that use high-speed cameras to track the passage of bubbles through fluid–fluid interfaces have led to theoretical and numerical investigations of this problem.
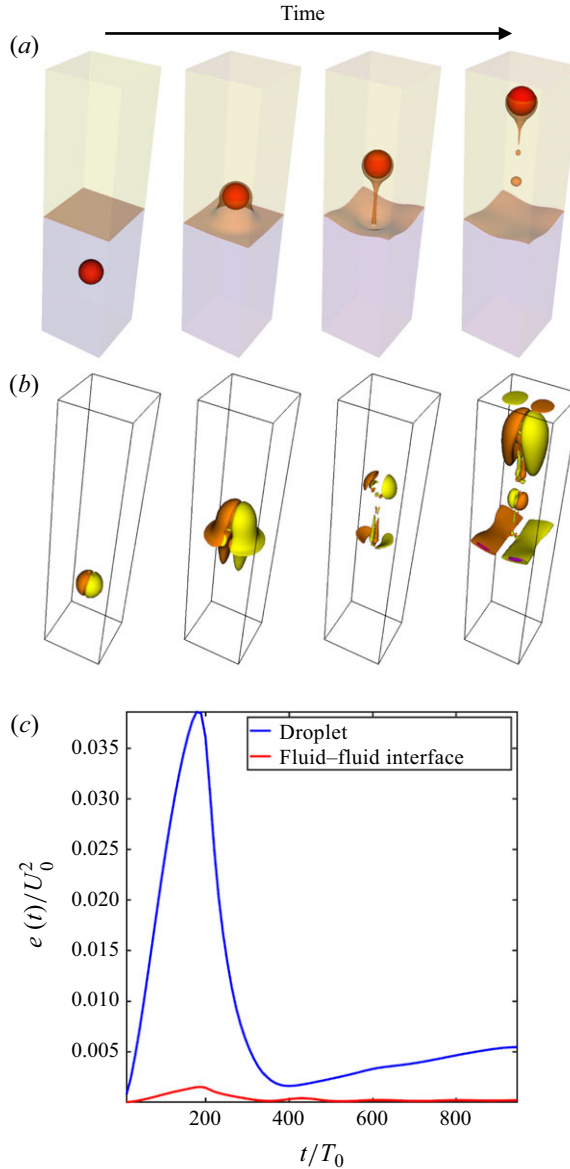
Figure 15. A bubble passing through a fluid–fluid interface. (*a*) The isosurface plot of the (c_1, c_2) fields. (*b*) The isocontour plot of the z component of the vorticity field. (*c*) The kinetic energy time series of the droplet (blue line), where $e(t) = \langle |\boldsymbol{u}(\boldsymbol{x})|^2 \rangle_{\boldsymbol{x} \in (c_1 \geqslant 0.5)}$. The red line shows line shows the kinetic energy time series of the fluid–fluid interface defined as $e(t) = \langle |\boldsymbol{u}(\boldsymbol{x})|^2 \rangle_{\boldsymbol{x} \in (0.1 \leqslant c_2 \leqslant 0.9)}$. We use the characteristic velocity and time scales as $U_0 = g\epsilon^2/\nu$ and $T_0 = \nu/g\epsilon$.

In figure 15 we present our results from an illustrative DNS of a bubble passing through a fluid–fluid interface; for this we employ the three-component 3-D CHNS3 equations (7.7)–(7.9) and choose parameters such that the bubble does go through the interface and does not get trapped there. For such studies it is natural to use the characteristic velocity and time scales $U_0 = g\epsilon^2/\nu$ and $T_0 = \nu/g\epsilon$, an elongated simulation domain $((L_x, L_y, L_z) = (4\pi, \pi, \pi)$, with $512 \times 128 \times 128$ grid points) with periodic BCs in the directions normal to gravity, and volume penalisation in the direction of gravity to

incorporate solid boundaries. We use six grid points at both top and bottom boundaries in our volume-penalisation scheme and the following simulation parameters: $\nu = 3.5 \times 10^{-3}$, $g = 1$, $\mathcal{A}_1 = 0.132$, $\mathcal{A}_2 = 0.132$, $\rho_1 = 1.132$, $\rho_2 = 0.868$, $\rho_3 = 1$ (with ρ_3 as the reference density), and $\sigma_{12} = \sigma_{13} = 0.5$ and $\sigma_{23} = 0.01$. Figures 15(*a*) and 15(*b*) show, respectively, isosurface plots of the c_1 and c_2 fields and isocontour plots of the z component of the vorticity field, which illustrate how a c_1 droplet of the first fluid (in red), with concentration field c_1, passes through the $c_2 - c_3$ interface (light brown) between the second and third fluids. As it passes through the interface, this droplet entrains some of the heavy fluid, which forms a slender neck that collapses eventually to yield droplets of the heavy fluid that fall back onto the interface (see, e.g., Singh & Bart 2015 and Emery *et al.* 2018). In figure 15(*c*) we show that we can track the passage of this bubble through the interface by monitoring the temporal evolution of the droplet's kinetic energy [$e_d(t) \equiv \langle |\boldsymbol{u}(\boldsymbol{x})|^2 \rangle_{\boldsymbol{x} \in (c_1 \geqslant 0.5)}$ (blue line)] and the energy of the $c_2 - c_3$ interface ($e_I(t) = \langle |\boldsymbol{u}(\boldsymbol{x})|^2 \rangle_{\boldsymbol{x} \in (0.1 \leqslant c_2 \leqslant 0.9)}$ (red line)); both these quantities display maxima when the bubble passes through the interface.

7.5. *The coalescence of liquid lenses and droplets*

The coalescence of liquid droplets and lenses is a problem of fundamental importance in fluid mechanics and statistical mechanics (see, e.g., Paulsen *et al.* 2014; Pal 2016; Heinen *et al.* 2022; Padhan & Pandit 2023*b*; Scheel *et al.* 2023). Our DNS for the CHNS3 (Padhan & Pandit 2023*b*) model can be used to examine the development of liquid-lens mergers in phase-separated ternary-fluid systems as we summarise below. The coexistence of three immiscible fluids leads to three distinct interfaces with three interfacial tensions: σ_{ij} is the surface-tension coefficient for the ij interface, where the integers i and j ($= 1, 2$ or 3) label the coexisting phases. We prepare neutrally buoyant, symmetrical or asymmetrical, lenses in two dimensions by starting our DNS with the following configuration for a single circular droplet of fluid 1, with radius R_0 and centre at (π, π), placed at the interface between fluids 2 and 3 (see figure 16*a*):

$$
\begin{aligned}
c_1(x, y, 0) &= \frac{1}{2} \left[1 - \tanh \left(\frac{\sqrt{(x - \pi)^2 + (y - \pi)^2} - R_0}{2\sqrt{2}\epsilon} \right) \right]; \\
c_2(x, y, 0) &= \frac{1}{2} \left[1 - \tanh \left(\frac{y - \pi}{2\sqrt{2}\epsilon} \right) \right] - c_1(x, y, 0); \\
\omega(x, y, 0) &= 0.
\end{aligned}
\tag{7.12}
$$

The initial and equilibrium configurations in three dimensions are a sphere and a lenticular biconvex lens, respectively. As time evolves in our (2-D) DNS, the initial circular droplet relaxes to its equilibrium-lens shape as shown in figures 16(*b*) and 16(*c*) for $(\sigma_{12}, \sigma_{13}, \sigma_{23}) = (1, 1, 1)$ and $(\sigma_{12}, \sigma_{13}, \sigma_{23}) = (1.4, 0.8, 1)$, respectively. Now we verify the Young relations for liquid lenses at equilibrium (see, e.g., Boyer & Lapuerta 2006; McHale *et al.* 2022). The theoretical distance d^{th} between the two triple-phase junctions in figures 16(*b*) and 16(*c*) are given by the following Young relations:

$$
\begin{aligned}
d^{th} &= (l_1 + l_2)^{-\frac{1}{2}}; \\
l_1 &= \frac{2(\pi - \theta_3) - \sin(2(\pi - \theta_3))}{8A \sin(\pi - \theta_3)}; \\
l_2 &= \frac{2(\pi - \theta_1) - \sin(2(\pi - \theta_1))}{8A \sin(\pi - \theta_1)}.
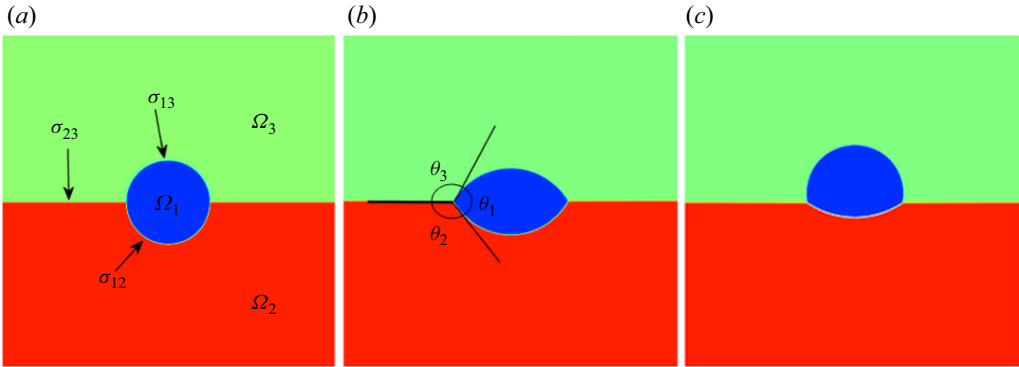\end{aligned}
\tag{7.13}
$$

Figure 16. Plots showing the three coexisting phases 1 (blue), 2 (red) and 3 (green) in regions Ω_1, Ω_2 and Ω_3, respectively. (*a*) The initial profile with a circular droplet of radius $R_0/L = 0.15$ of fluid 1 at the interface between fluids 2 and 3. ($L = 2\pi$ is the side length of the simulation domain.) (*b*) The equilibrium profile of the droplet is a symmetrical lens, because we choose $(\sigma_{12}, \sigma_{13}, \sigma_{23}) = (1, 1, 1)$; the three contact angles are θ_1, θ_2 and θ_3. (*c*) The equilibrium profile of the droplet is an asymmetrical lens if we choose $(\sigma_{12}, \sigma_{13}, \sigma_{23}) = (1.4, 0.8, 1)$.

Runs	$(\sigma_{12}, \sigma_{13}, \sigma_{23})$	d^{th}	d^{sim}	Relative error (%)
$\mathcal{R}1$	(1, 1, 1)	2.15	2.18	1.4
$\mathcal{R}2$	(1.4, 0.8, 1)	1.3	1.35	3

Table 3. The distance between two triple-phase junctions calculated from theory d^{th} (see (7.14)] and numerical simulations d^{sim} for the symmetrical lens (figure 16*b*) and the asymmentrical lens (figure 16*c*).

The contact angles are related as follows:

$$\frac{\sin \theta_1}{\sigma_{23}} = \frac{\sin \theta_2}{\sigma_{13}} = \frac{\sin \theta_3}{\sigma_{12}}. \tag{7.14}$$

We calculate the distance between the triple-phase junctions d^{sim} from our simulations (see figures 16*b* and 16*c*) and compare them with d^{th} in table 3. The agreement between these values is good. Furthermore, we can compare the results of our DNS with the prediction of the Laplace law for pressure jumps, at equilibrium; these jumps are defined as follows:

$$\frac{\sigma_{13}}{R_{13}} = P_1 - P_3 = P_1 - P_2 = \frac{\sigma_{12}}{R_{12}};$$
$$P_2 - P_3 = 0; \tag{7.15}$$

where R_{12} and R_{13} are the radii of curvatures of the interfaces between fluids 1 and 2 and between fluids 1 and 3, respectively. To calculate the radii of curvatures, we use the circle Hough transform (CHT) in MATLAB (see Atherton & Kerbyson 1999). In figure 17, we illustrate the CHT of the images in figures 16(*b*) and 16(*c*); red circles are the best-fit circles to the curves. The CHT gives the coordinates of the centres and the radii of the red circles. We calculate the theoretical values of the pressure jumps from these radii of curvatures. To compare our DNS results with these theoretical values, we evaluate the pressure jumps
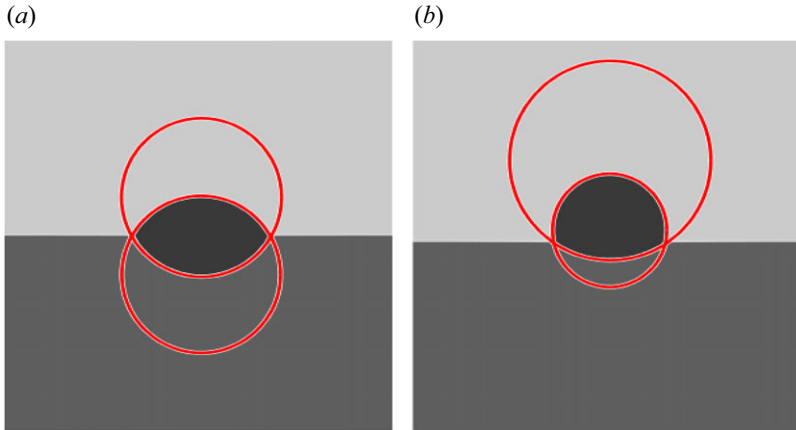
(*a*)　　　　　　　　　　　　　　　(*b*)

Figure 17. Illustrations of the CHT (see the text) that we use to fit circles for the lens interfaces for (*a*) $(\sigma_{12}, \sigma_{13}, \sigma_{23}) = (1, 1, 1)$ (run $\mathcal{R}1$) and (*b*) $(\sigma_{12}, \sigma_{13}, \sigma_{23}) = (1.4, 0.8, 1)$ (run $\mathcal{R}2$).
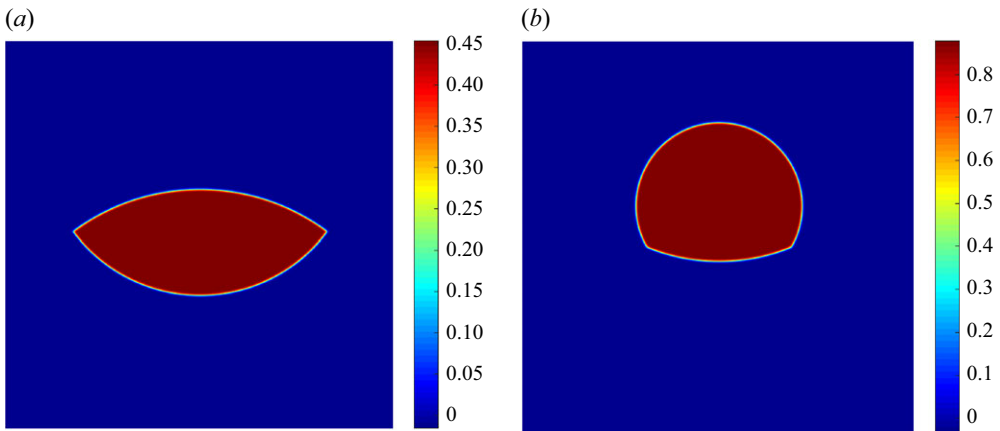
(*a*)　　　　　　　　　　　　　　　(*b*)

Figure 18. Pseudocolour plot of illustrative equilibrium-pressure profiles for (*a*) $(\sigma_{12}, \sigma_{23}, \sigma_{13}) = (0.6, 1, 0.8)$ (run RN3) and (*b*) $(\sigma_{12}, \sigma_{23}, \sigma_{13}) = (1.4, 1, 0.6)$ (run RN4).

from the following pressure-Poisson equation:

$$\nabla^2 P = \nabla \cdot \left(-\sum_{i=1}^{3} c_i \nabla \mu_i \right), \tag{7.16}$$

which we portray via pseudocolour plots of illustrative equilibrium-pressure profiles for runs RN1 and RN2 in figure 18. We present our DNS results in table 4 for various runs. These results are in good agreement with their theoretical counterparts. We obtain similar results from 3-D DNSs of the CHNS3 model: in figure 19(*a*) we give an isosurface plot, with $c_1 = 0.5$, for a 3-D lenticular biconvex lens. We then calculate its Gaussian curvature κ by implementing, in MATLAB, the algorithm described in Meyer *et al.* (2003). The isosurface plot of κ is shown in figure 19(*b*); clearly, κ is constant throughout the lens surface, except at the edges. So, in figure 19(*c*), we present the PDF of κ to find out the most probable value of κ. We consider the values of κ with the highest probability, namely, $0.59, -0.04, 1.23$; the average value is $\kappa \simeq 0.593$. The Gaussian curvature $\kappa = 1/R_G^2$ for a sphere of radius R_G (see, e.g., Nothard *et al.* 1996). The symmetric 3-D lens in figure 19(*a*)

Runs	$(\sigma_{12}, \sigma_{23}, \sigma_{13})$	R_0/L	Theory ΔP	Simulation ΔP	Relative error (%)
RN1	(1, 1, 1)	0.2	0.989	0.994	0.5
RN2	(1, 0.8, 1)	0.2	1.148	1.132	1.3
RN3	(0.6, 1, 0.8)	0.2	0.465	0.460	1
RN4	(1.4, 1, 0.6)	0.2	0.889	0.891	0.2
RN-3D	(1, 1, 1)	0.13	1.54	1.56	1.2

Table 4. Illustrative comparisons of theoretical and our DNS results for Laplace-pressure jumps for different lens shapes, $\Delta P \equiv P_1 - P_2 = P_1 - P_3$. There is good agreement between these results. While evaluating ΔP, we calculate the values of P_1, P_2 and P_3 at points that are far from the interface.
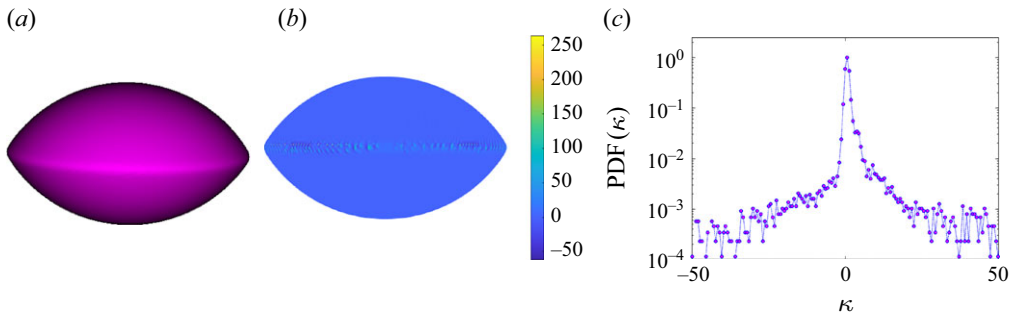

Figure 19. (*a*) The isosurface plot of $c_1 = 0.5$, at equilibrium, illustrating a lens in three dimensions. (*b*) The isosurface plot of the corresponding Gaussian curvature κ. (*c*) The PDF of the Gaussian curvature.

is a combination of two surfaces that are parts of spheres of equal radii. Then we follow the Laplace law in three dimensions to evaluate the pressure jumps,

$$\frac{2\sigma_{13}}{R_{13}} = P_1 - P_3 = P_1 - P_2 = \frac{2\sigma_{12}}{R_{12}};$$
$$P_2 - P_3 = 0; \tag{7.17}$$

where $R_{13} = R_{12} = R_G = 1/\sqrt{\kappa}$. The theoretical values of the pressure jumps are given in table 4 (see run RN-3D); we solve the pressure-Poisson equation (7.16) numerically; we find good agreement between the theoretical and numerical values of these jumps.

We turn now to an overview of our recent study (Padhan & Pandit 2023*b*) that has shown how to use DNSs of the CHNS3 system (7.7)–(7.9) and their 2-D counterparts to study the spatiotemporal evolution of the merger of liquid lenses in both two dimensions and three dimensions. In figure 20 we present illustrative results from these DNSs in two dimensions (figure 20*a*,*b*) and three dimensions (figure 20*c*,*d*). In two dimensions we give pseudocolour plots of ω, with overlaid velocity vectors in (figure 20*a*) the viscous regime and (figure 20*b*) the inertial regime; the $c_1 = 0.5$ contour (magenta line) indicates the lens interface; ω is normalised by its maximal absolute value for ease of visualisation. Isosurface plots of c_1 (green) and $|\omega|$ (brown) for (figure 20*c*) the viscous regime and (figure 20*d*) the inertial regime. In the viscous regime, i.e. at large values of the Ohnesorge number Oh, a vortex quadrupole dominates the flow in the region of the neck in both 2-D and 3-D lens mergers, shown in figures 20(*a*) and 20(*c*), respectively. In the small-Oh inertial regime (figures 20*b* and 20*d*) for two dimensions and three dimensions, respectively, this quadrupole moves away from the region of the neck with the passage
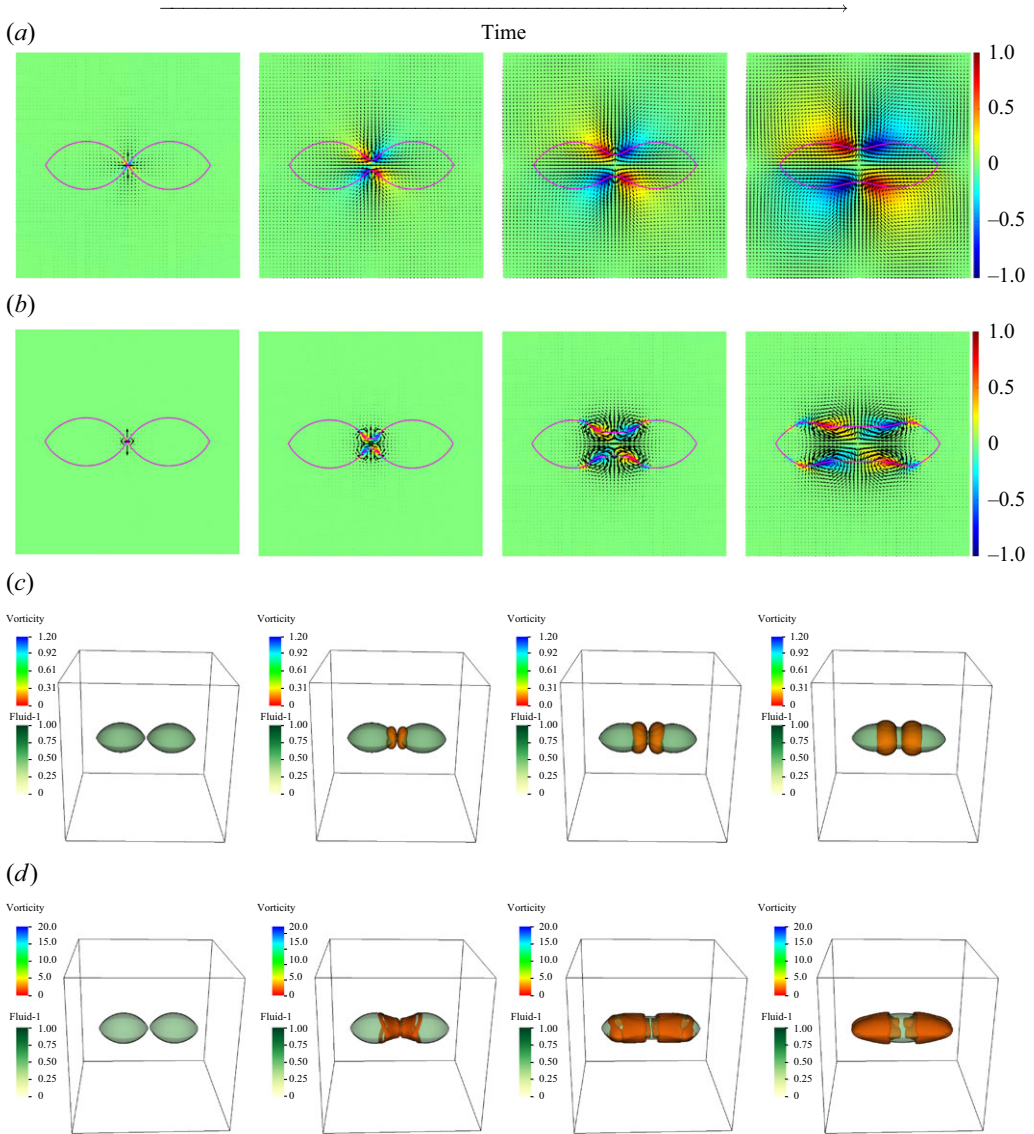
Figure 20. Illustrative results from our DNSs of liquid-lens mergers in the CHNS3 model in (a,b) two dimensions and (c,d) three dimensions: pseudocolour plots of ω, with overlaid velocity vectors in (a) the viscous regime and (b) the inertial regime; the $c_1 = 0.5$ contour (magenta line) indicates the lens interface; ω is normalised by its maximal absolute value for ease of visualisation. Isosurface plots of c_1 (green) and $|\omega|$ (brown) for (c) the viscous regime and (d) the inertial regime.

of time. We quantify the growth of the height $h(t)$ of the neck, in the low-Oh case, in figure 21 that contains a log–log plot of h versus the time t. This plot shows clearly the crossover from the viscous regime with $h(t) \sim t$, at early times, to $h(t) \sim t^{2/3}$, at late times. The exponent $2/3$ is typical of inertial-regime neck growth; the early-time growth is similar to that found in the viscous case (because the early-time quadrupolar configuration is similar to that in the viscous case). The inset shows the velocity vectors near the neck region at a representative time. In figure 21(b) we show the profile of the
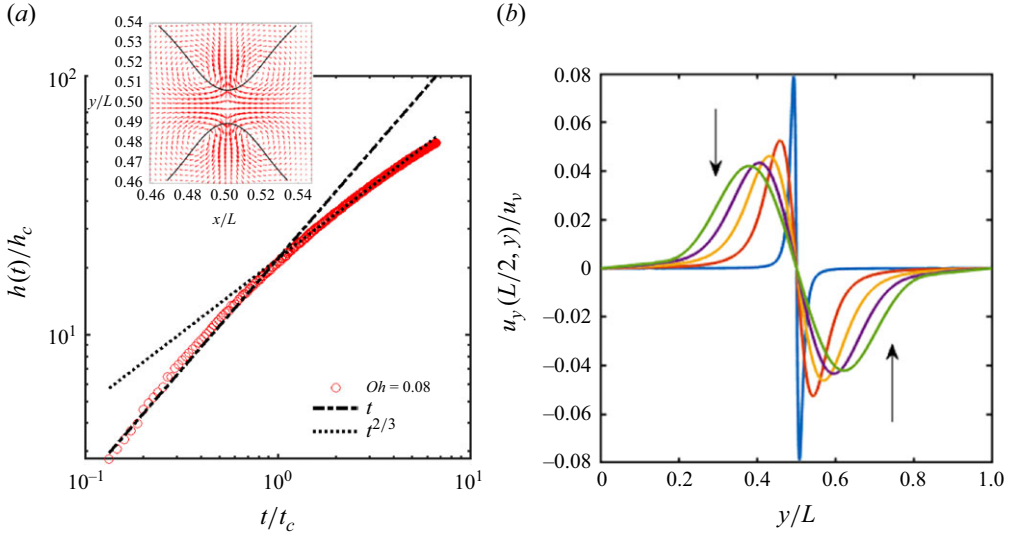
1010 P1-44

Figure 21. (*a*) Log–log plot of the neck height h versus time t. The axes are scaled by their respective viscous length scales for $Oh = 0.08$. The plot shows the crossover in the neck growth from the viscous regime with $h(t) \sim t$ to the inertial regime with $h(t) \sim t^{2/3}$. The inset shows the velocity vectors near the neck region at a representative time. (*b*) The profile of the y component of the velocity field $u_y(L/2, y)$ along the vertical direction; the arrows show the direction of the evolution of the profiles.

y-component of the velocity field $u_y(L/2, y)$, along the vertical direction; the arrows show how the profiles flatten as t increases.

7.6. *Active CHNS model*

We consider the following incompressible CHNS equations (also called active model H) to study active turbulence in systems of contractile swimmers (see, e.g., Tiribocchi *et al.* 2015; Padhan & Pandit 2023*a*; Cates & Nardini 2024; Padhan *et al.* 2024*a*; Padhan & Voigt 2025) in two spatial dimensions:

$$\partial_t \phi + (\boldsymbol{u} \cdot \nabla)\phi = M \nabla^2 \left(\frac{\delta \mathcal{F}}{\delta \phi} \right) ; \tag{7.18}$$

$$\partial_t \omega + (\boldsymbol{u} \cdot \nabla)\omega = \nu \nabla^2 \omega + \frac{3}{2} \epsilon \nabla \times (\nabla \cdot \boldsymbol{\Sigma}^A) - \alpha \omega ; \tag{7.19}$$

$$\nabla \cdot \boldsymbol{u} = 0; \tag{7.20}$$

where ω is the vorticity field; ν, α and M are the kinematic viscosity, bottom friction and mobility, respectively. Here $\mathcal{F}$ is the LG variational free-energy functional

$$\mathcal{F}[\phi, \nabla\phi] = \int_\Omega \left[\frac{3}{16} \frac{\sigma}{\epsilon} (\phi^2 - 1)^2 + \frac{3}{4} \sigma \epsilon |\nabla\phi|^2 \right], \tag{7.21}$$

in which the first term is a double-well potential with minima at $\phi = \pm 1$. The scalar order parameter ϕ is positive (negative) in regions where the microswimmer density is high (low); in the interfaces between these regions, ϕ varies smoothly, over a width ϵ. The free-energy penalty for an interface is given by the bare surface tension σ. In the inherently non-equilibrium active model H all terms in the stress tensor do not follow from $\mathcal{F}$. In particular, we must include the stress tensor $\boldsymbol{\Sigma}^A$, which has the form of a nonlinear Burnett term and has the components (see, e.g., Tiribocchi *et al.* 2015; Das, Bhattacharjee

& Kirkpatrick 2020; Bhattacharjee & Kirkpatrick 2022; Padhan & Pandit 2023*a*; Padhan *et al.* 2024*a*)

$$\Sigma_{ij}^A = -\zeta \left[\partial_i \phi \partial_j \phi - \frac{\delta_{ij}}{2} |\nabla \phi|^2 \right], \tag{7.22}$$

where ζ, the activity coefficient, can take both positive and negative values: $\zeta < 0$ ($\zeta > 0$) for contractile (extensile) swimmers. We emphasise that the free-energy functional used in this active model is a mathematical construct without a direct physical origin. The activity is introduced phenomenologically. For instance, an active-stress term with an effective negative surface tension coefficient has been incorporated into the model to capture the coarsening-arrest mechanism in contractile systems (see, e.g., Tiribocchi *et al.* 2015; Cates & Nardini 2024).

7.7. *Generalised active CHNS model for an active self-propelling droplet*

To study active, self-propelling droplets, we follow Padhan & Pandit (2023*a*) and use two scalar fields ϕ and ψ, with ψ an active scalar, in the active-matter sense (see, e.g., Marchetti *et al.* 2013). (The terminology used in active matter and conventional fluid dynamics differs slightly. In fluid dynamics, both ϕ and ψ are considered active scalars because they influence the velocity field $\boldsymbol{u}$. However, in active matter, only ψ is regarded as active, whereas ϕ is not.) We employ the following free-energy functional,

$$\mathcal{F}[\phi, \nabla\phi, \psi, \nabla\psi] = \int_{\Omega} \frac{3}{16} \left(\frac{\sigma_1}{\epsilon_1}(\phi^2 - 1)^2 + \frac{\sigma_2}{\epsilon_2}(\psi^2 - 1)^2 \right) - \beta\phi\psi$$
$$+ \frac{3}{4} \left(\sigma_1\epsilon_1|\nabla\phi|^2 + \sigma_2\epsilon_2|\nabla\psi|^2 \right) \mathrm{d}\Omega, \tag{7.23}$$

where Ω is the region we consider. This model allows for interfaces of ϕ and ψ, with (bare) positive interfacial tensions σ_1 and σ_2 and widths ϵ_1 and ϵ_2, respectively; the coupling constant $\beta > 0$, so there is an attractive coupling between ϕ and ψ. Experiments on active droplets are carried out confined planar domains, so we use the following generalisation of the 2-D active incompressible CHNS equations given in § 7.6:

$$\partial_t \phi + (\boldsymbol{u} \cdot \nabla)\phi = M_1 \nabla^2 \left(\frac{\delta\mathcal{F}}{\delta\phi} \right); \tag{7.24}$$

$$\partial_t \psi + (\boldsymbol{u} \cdot \nabla)\psi = M_2 \nabla^2 \left(\frac{\delta\mathcal{F}}{\delta\psi} \right); \tag{7.25}$$

$$\partial_t \omega + (\boldsymbol{u} \cdot \nabla)\omega = \nu\nabla^2\omega - \alpha\omega + [\nabla \times (\mathfrak{S}^\phi + \mathfrak{S}^\psi)]; \tag{7.26}$$

$$\nabla \cdot \boldsymbol{u} = 0; \quad \omega = (\nabla \times \boldsymbol{u}); \tag{7.27}$$

$$\mathfrak{S}^\phi = -(3/2)\sigma_1\epsilon_1\nabla^2\phi\nabla\phi; \tag{7.28}$$

$$\mathfrak{S}^\psi = -(3/2)\tilde{\sigma}_2\epsilon_2\nabla^2\psi\nabla\psi; \tag{7.29}$$

where, the vorticity, kinematic viscosity and the bottom friction are, respectively, ω, ν and α and we set the constant fluid density $\rho = 1$. We use the constant mobilities M_1 and M_2 for ϕ and ψ, respectively; the ϕ interfacial stress $\mathfrak{S}^\phi$ (7.28) follows from $\mathcal{F}$; in contrast, for the active stress $\mathfrak{S}^\psi$ (7.29) from ψ, we use the active-model-H formulation (see, e.g., Wittkowski *et al.* 2014; Tiribocchi *et al.* 2015; Shaebani *et al.* 2020; Padhan & Pandit 2023*a*). It is important to note that (i) both ω and $[\nabla \times (\mathfrak{S}^\phi + \mathfrak{S}^\psi)]$ are orthogonal to the 2-D plane and (ii) the mechanical surface tension $\tilde{\sigma}_2 \neq \sigma_2$, which can be either negative
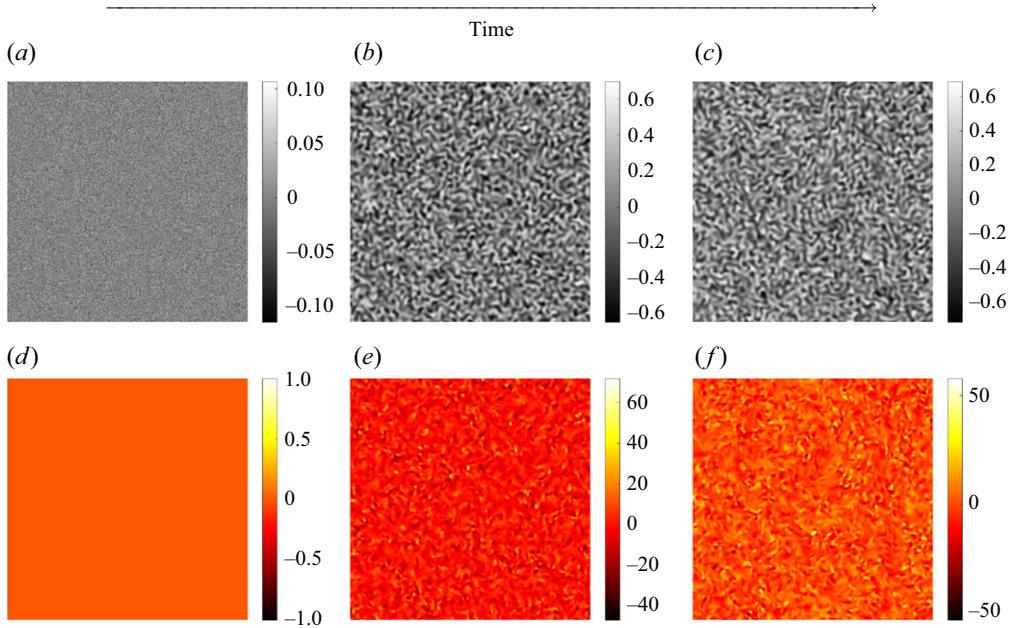
Figure 22. (*a*–*c*) Pseudocolour plots of the active-scalar field ϕ, at three representative times, which increase from left to right, for the activity parameter $\zeta = 0.1$ (see (7.18)–(7.22)); (*d*–*f*) pseudocolour plots of the vorticity ω corresponding, respectively, to the pseudocolour plots ϕ in (*a*–*c*).

or positive values, unlike σ_1 and σ_2 that are positive. For contractile swimmers $\tilde{\sigma}_2 < 0$ and for extensile swimmers $\tilde{\sigma}_2 > 0$; the former show arrested phase separation, whereas the latter display complete phase separation (see, e.g., Tiribocchi *et al.* 2015; Padhan & Pandit 2023*a*). We will show in § 7.9 that the activity

$$A = |\tilde{\sigma}_2|/\sigma_2, \tag{7.30}$$

is the most important control parameter here.

7.8. *Active CHNS turbulence*

Turbulence in active fluids, which include dense bacterial suspensions, has garnered considerable attention over the past decade (see, e.g., Wensink *et al.* 2012; Dunkel *et al.* 2013; Bratanov *et al.* 2015; Alert *et al.* 2021). Many models of active fluids consider systems of polar active swimmers (e.g., Jain *et al.* 2024; Rana *et al.* 2024) or Toner–Tu type systems and their generalisations (see, e.g., Toner & Tu 1998; Toner, Tu & Ramaswamy 2005; Rana & Perlekar 2020; Alert *et al.* 2021; Mukherjee *et al.* 2021; Gibbon *et al.* 2023; Kiran *et al.* 2023, 2024). In a recent paper, Padhan *et al.* (2024*a*) have demonstrated that a new type of active-scalar turbulence occurs in active-model H (see (7.18)–(7.22)), whose stochastic version has been studied in the context of MIPS that has been discussed at very low Reynolds numbers by Tiribocchi *et al.* (2015) and Cates & Tailleur (2015). We give an overview of the work of Padhan *et al.* (2024*a*) in figures 22 and 23, which examines activity-induced turbulence in (7.18)–(7.22) by increasing ζ in this active model H; positive values of ζ are used for contractile swimmers, whereas negative values of ζ are appropriate for extensile swimmers. Padhan *et al.* (2024*a*) concentrate on $\zeta < 0$, which yields activity-induced turbulence that suppresses phase separation. It has been suggested in Padhan *et al.* (2024*a*) that this model, with $\zeta < 0$, might be applicable to a dense suspension of *Chlamydomonas reinhardtii*.
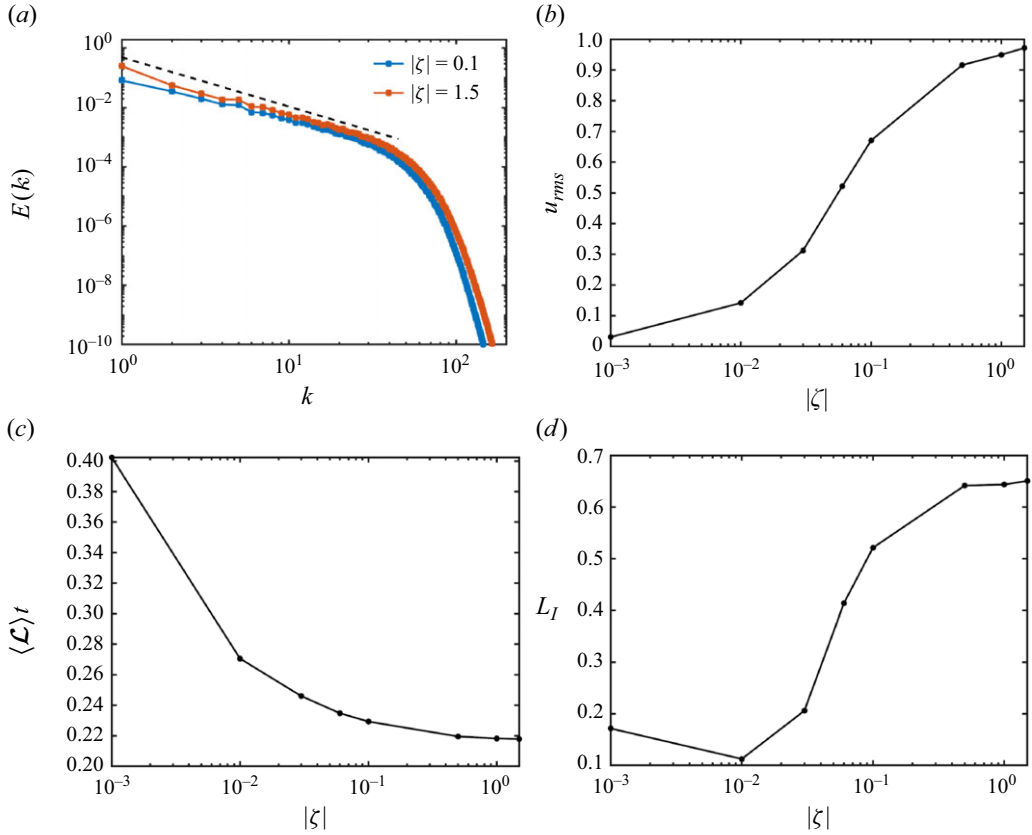
Figure 23. (*a*) Log–log plots of the energy spectra $E(k)$ versus the wavenumber k, for the activities $|\zeta| = 0.1$ and $|\zeta| = 1.5$ in (7.18)–(7.22); power-law regimes in these spectra are consistent with the dashed line $E(k) \sim k^{-5/3}$; (*b*) plot of the root-mean-squared velocity u_{rms} versus $|\zeta|$; (*c*) log–linear plots versus $|\zeta|$ of (*c*) the mean coarsening length scale $L_c \equiv \langle \mathcal{L}(t)_t \rangle$ and (*d*) the integral length scale L_I.

In figures 22(*a*) and 22(*c*) we show greyscale plots of the active-scalar field ϕ, at three representative times, which increase from left to right, for the activity parameter $|\zeta| = 0.1$ (see (7.18)–(7.22)); figures 22(*d*) and 22(*f*) contain pseudocolour plots of the vorticity ω corresponding, respectively, to the pseudocolour plots ϕ in figures 22(*a*) and 22(*c*). These plots indicate that, as time increases, the activity induces spatiotemporal chaos and turbulence; eventually the systems reaches a non-equilibrium statistically steady state in which coarsening is arrested by active turbulence (much as it is arrested by conventional fluid turbulence as we have discussed in § 6.3). We can characterise the statistical properties of this turbulence using the spectra and lengths that we have defined in (6.6) for phase separation in the binary-fluid case. In figure 23(*a*) we present log–log plots of the energy spectra $E(k)$ versus the wavenumber k, for the activities $|\zeta| = 0.1$ and $|\zeta| = 1.5$ in (7.18)–(7.22). Clearly, the energy is spread out over a large range of k as it is in fluid turbulence; furthermore, the power-law regimes in these spectra are consistent with $E(k) \sim k^{-5/3}$ (indicated by the dashed line). The root-mean-squared velocity u_{rms} grows with $|\zeta|$ (figure 23*b*). In figures 23(*c*) and 23(*d*) we present log–linear plots versus $|\zeta|$ of the mean coarsening length scale $L_c \equiv \langle \mathcal{L}(t) \rangle_t$ and the integral length scale L_I, respectively. Figures 23(*b*) and 23(*d*) quantify the enhancement of turbulence in (7.18)–(7.22) with increasing $|\zeta|$; and figure 23(*c*) characterises coarsening arrest by this form of active turbulence.
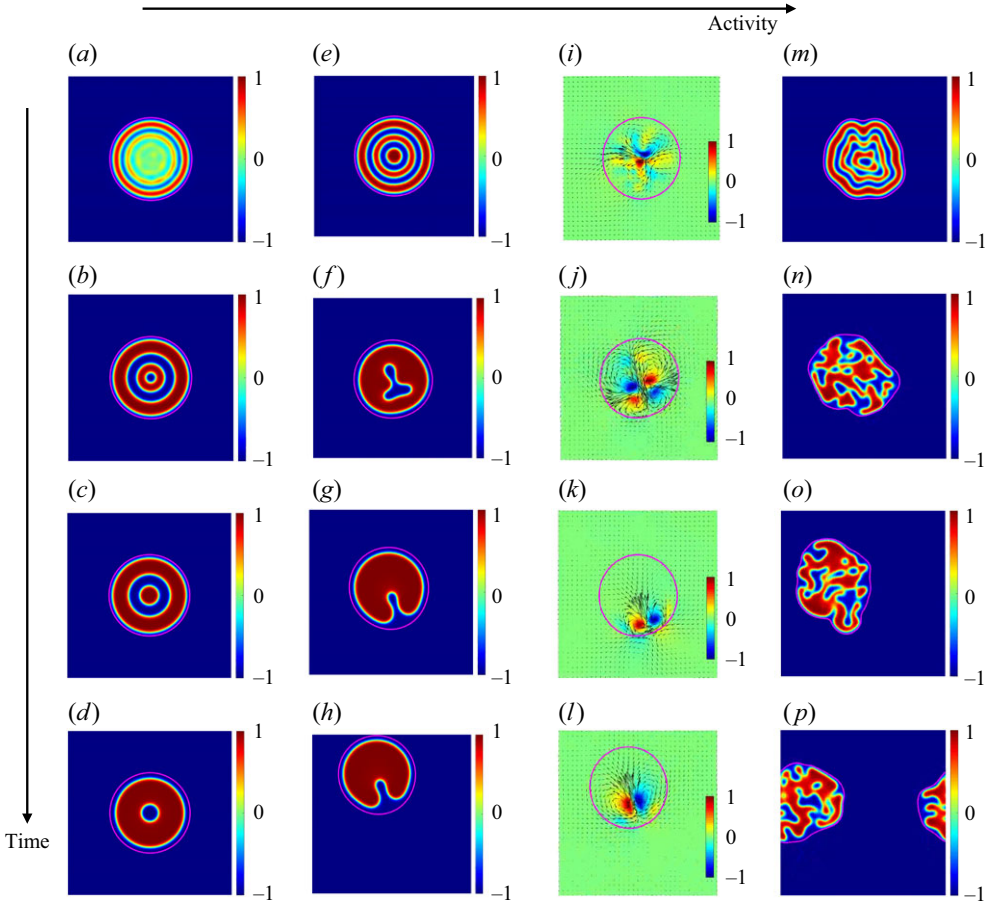
Activity

Time

Figure 24. Activity-induced droplet propulsion: pseudocolour plots of ψ (the magenta contour shows $\phi = 0$), at various times t and activities A (t increases from the top row to the bottom row): (a)–(d) $A = 0$ (complete phase separation in ψ and no droplet propulsion); (e)–(h) $A = 0.15$ (rectilinear droplet propulsion); and (m)–(p) $A = 1$ (chaotic droplet propulsion). (i)–(l) For $A = 0.15$: vector plots of $\boldsymbol{u}$, with the overlaid $\phi = 0$ contour line (magenta) and the pseudocolour plot of ω, normalised by its maximal value (velocity vectors have lengths proportional to $|\boldsymbol{u}|$).

7.9. *Activity-induced droplet propulsion*

We now use (7.23)–(7.29) (see § 7.7) to demonstrate activity-induced droplet propulsion in a model that has been studied in detail by Padhan & Pandit (2023*a*). This model employs two scalar fields ϕ and ψ; both affect the velocity field $\boldsymbol{u}$ by which they are advected; but only ψ is active in the parlance of active matter. Negative and positive values of ϕ and ψ lead, respectively, to low and high densities of these scalars. We begin with the following initial data: a circular droplet, of radius R_0 and centre at $(x_{0,1}, x_{0,2}) = (\pi, \pi)$:

$$\boldsymbol{u}(\boldsymbol{x}, t = 0) = 0;$$

$$\phi(\boldsymbol{x}, t = 0) = \tanh\left(\frac{R_0 - \sqrt{(x_1 - x_{0,1})^2 + (x_2 - x_{0,2})^2}}{\epsilon_1}\right);$$

$$\psi(\boldsymbol{x}, t = 0) = \begin{cases} \psi_0(\boldsymbol{x}) & \text{for } |\boldsymbol{x}| \leqslant R_0; \\ -1 & \text{for } |\boldsymbol{x}| > R_0; \end{cases} \qquad (7.31)$$
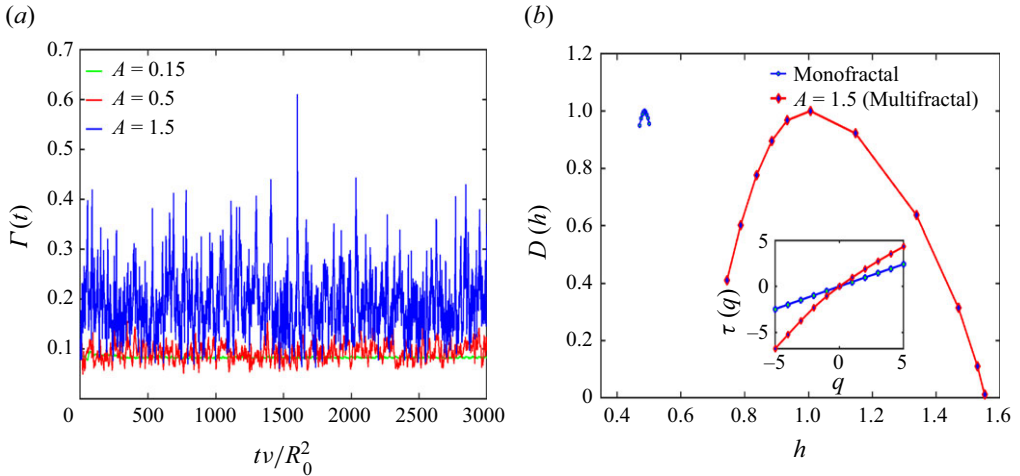
(a)

(b)

Figure 25. (a) The multifractal time series for the scaled perimeter-deformation parameter $\Gamma(t)$ for various values of the activity. (b) The multifractal spectrum for representative activity $A = 1.5$. *We* present the spectrum for a monofractal time series (given in blue) to show the robustness of the multifractal spectrum. The inset shows the plot of generalised exponent $\tau(q)$ as a function of the order q for the representative value $A = 1.5$; the deviation from the linearity suggests the multifractality of $\Gamma(t)$.

where $\psi_0(\boldsymbol{x})$ is distributed uniformly and randomly on the interval $[-0.1, 0.1]$. We then monitor the spatiotemporal evolution of ϕ, ψ and the normalised ω, which we depict in figure 24 via pseudocolour plots with an overlaid $\phi = 0$ contour; the pseudocolour plots of ω also have superimposed vector plots of the velocity field $\boldsymbol{u}$. The non-dimensional Weber numbers $We_1 = R_0 U_0^2/\sigma_1$ and $We_2 = R_0 U_0^2/\sigma_2$, Cahn numbers $Cn_1 = \epsilon_1/R_0$ and $Cn_2 = \epsilon_2/R_0$, Peclet numbers $Pe_1 = R_0 U_0 \epsilon_1/(M_1\sigma_1)$ and $Pe_2 = R_0 U_0 \epsilon_2/(M_2\sigma_2)$, Reynolds number $Re = R_0 U_0/\nu$, where $U_0 = \langle U_{CM}(t)\rangle_t$, with U_{CM}, the speed of the droplet's centre of mass (subscript CM), the order-parameter couplings $\beta_1' = \beta\epsilon_1/\sigma_1$ and $\beta_2' = \beta\epsilon_2/\sigma_2$, and the friction $\alpha' = \alpha R_0/U_0$, all affect the detailed dynamics of this initial droplet. However, most important of all these control parameters is the activity A (7.30).

In figure 24 we exhibit activity-induced droplet propulsion in this model by illustrative pseudocolour plots of ψ, with the $\phi = 0$ contour shown in magenta; we show such plots at different representative times, which increase from top to bottom, and three values of A, which move from low to high values, as we move from left to right. In figure 24(a–d) we show the spatiotemporal of this droplet for the case of vanishing activity $A = 0$; there is no droplet propulsion and the system proceeds towards complete phase separation of ψ, inside the $\phi = 0$ contour, by the formation of alternating annuli of regions with $\psi > 0$ and $\psi < 0$, which is reminiscent of the phase separation of oil and water in a microfluidic droplet (see Moerman *et al.* 2018). Figure 24(e–h) show that, when $A = 0.15$, the system displays rectilinear propulsion of an active droplet; this is driven by the formation of an oscillating dipole that is visible clearly in figure 24(i–l), where we show, for $A = 0.15$, vector plots of the velocity field $\boldsymbol{u}$, with the $\phi = 0$ contour line (magenta), overlaid on a pseudocolour plot of the vorticity ω normalised by its maximal value. Finally, we show in figure 24(m–p), where $A = 1$, chaotic droplet propulsion, which is characterised by significant fluctuations inside the droplet and on its boundary; the former suppress phase separation within the droplet and lead to diffusive or superdiffusive meandering of the centre of mass of the droplet (see Padhan & Pandit (2023a) for details). The fluctuations of the boundary can be quantified by using the scaled droplet perimeter $\Gamma(t)$ (see (7.11) and figure 14 in § 7.3). In figure 25(a) we show that $\Gamma(t)$ has multifractal time series

for various values of the activity A; we characterise this in figure 25(*b*) by showing the multifractal spectrum for the representative value $A = 1.5$; for comparison we present this spectrum for a monofractal time series in blue; the inset shows a plot of the generalised exponent $\tau(q)$ as a function of the order q; the deviation of the red curve from linearity quantifies the multifractality of $\Gamma(t)$.

8. Conclusions and perspective

We have demonstrated that the CHNS framework offers an excellent theoretical foundation for probing diverse aspects of multiphase fluid flows in binary and ternary systems and in active fluids. We have given an introduction to the statistical mechanics of systems in which two or more coexisting phases, distinguished from each other by one or more scalar order parameters, are separated by an interface. Our discussion of systems with non-conserved and conserved order parameters leads, respectively, to the TDGL and CH PDEs. We have then considered models in which the coexisting phases are fluids; in particular, we have shown that two immiscible fluids require that we use the CHNS equations. We have given generalisations of the CHNS equations for (i) coexisting phases with different viscosities, (ii) CHNS with gravity, (iii) three-component fluids (CHNS3) and (iv) CHNS for active fluids. We have provided brief discussions of the methods we use for our DNSs of these CHNS systems and, in the antibubble case, we have contrasted the CHNS diffuse-interface approach with the VOF scheme that tracks the spatiotemporal evolution of sharp fluid–fluid interfaces. Furthermore, we have discussed mathematical issues of the regularity of solutions of the CHNS PDEs. Then we have provided a survey of the rich variety of results that have been obtained by numerical studies of CHNS-type PDEs for diverse systems, including droplets in turbulent flows, antibubbles, droplet and liquid-lens mergers, turbulence in the active-CHNS model and its generalisation that can lead to a self-propelled droplet. We hope that our overall perspective of this field will lead to more studies of multiphase flows in which interfaces and their fluctuations play important roles.

There are several other exciting areas in which the CHNS system can play (or has already played) an important role. We have not been able to cover all these areas here. We give an illustrative list of such areas along with representative references.

(i) We do not cover quasicompressible CHNS models; for these we refer the reader to Lowengrub & Truskinovsky (1998) and Abels, Garcke & Giorgini (2023); and for high-order CHNS PDEs readers should consult Pan, Xing & Luo (2020), Dlotko (2022), and references therein.

(ii) There are intriguing links between the 2-D CHNS system and 2-D MHD; these have been explored in, e.g., Fan *et al.* (2016, 2017, 2018)and Ramirez & Diamond (2024).

(iii) For simplicity we have considered coexisting phases with equal viscosities and densities. This constraint can be relaxed easily by using the CHNS (see (3.4)); and then this system can be used to study a variety of laboratory experiments, such as the droplet coalescence considered in Paulsen *et al.* (2011, 2014).

(iv) There has been considerable interest in the study of the CH-type PDEs on curved surfaces; we refer the reader to Voigt & Hoffman (2002) and Rätz & Voigt (2006).

(v) There has been a lot of recent work on non-reciprocal CH systems (see, e.g., Saha, Agudo-Canalejo & Golestanian 2020; You, Baskaran & Marchetti 2020; Frohoff-Hülsmann & Thiele 2023; Suchanek, Kroy & Loos 2023; Brauns & Marchetti 2024); we expect that these models will be coupled to the NS PDEs in future studies (for a recent study, see Pisegna *et al.* 2025).

(vi) Studies of the statistics of Lagrangian tracers or heavy inertial particles in CHNS systems are in their infancy (see, e.g., Padhan & Pandit 2024); we expect that such investigations will increase in the coming years.

Declaration of interests. The authors report no conflict of interest.

REFERENCES

ABELS, H. 2009a Existence of weak solutions for a diffuse interface model for viscous, incompressible fluids with general densities. *Commun. Math. Phys.* **289** (1), 45–73.

ABELS, H. 2009b *Longtime Behavior of Solutions of a Navier–Stokes/Cahn–Hiilliard system*. Banach Centre Publications.

ABELS, H., GARCKE, H. & GIORGINI, A. 2024 Global regularity and asymptotic stabilization for the incompressible Navier–Stokes–Cahn–Hilliard model with unmatched densities. *Math. Ann.* **389** (2), 1267–1321.

ALERT, R., CASADEMUNT, J. & JOANNY, J.-F. 2022 Active turbulence. *Annu. Rev. Condens. Matter Phys.* **13** (1), 143–170.

AMIT, D.J. & MARTIN-MAYOR, V. 2005 *Field Theory, the Renormalization Group, and Critical Phenomena: Graphs to Computers*. World Scientific Publishing Company.

ANDERSON, D.M., MCFADDEN, G.B. & WHEELER, A.A. 1998 Diffuse-interface methods in fluid mechanics. *Annu. Rev. Fluid Mech.* **30** (1), 139–165.

ANGOT, P., BRUNEAU, C.-H. & FABRIE, P. 1999 A penalization method to take into account obstacles in incompressible viscous flows. *Numer. Math.* **81** (4), 497–520.

ANNA, S.L. 2016 Droplets and bubbles in microfluidic devices. *Annu. Rev. Fluid Mech.* **48** (1), 285–309.

AREF, H. & SIGGIA, E.D. 1981 Evolution and breakdown of a vortex street in two dimensions. *J. Fluid Mech.* **109**, 435–463.

ATHERTON, T.J. & KERBYSON, D.J. 1999 Size invariant circle detection. *Image Vis. Comput.* **17** (11), 795–803.

BACKOFEN, R., ALTAWIL, A.Y., SALVALAGLIO, M. & VOIGT, A. 2024 Nonequilibrium hyperuniform states in active turbulence. *Proc. Natl Acad. Sci. USA* **121** (24), e2320719121.

BADALASSI, V.E., CENICEROS, H.D. & BANERJEE, S. 2003 Computation of multiphase systems with phase field models. *J. Comput. Phys.* **190** (2), 371–397.

BALACHANDAR, S. & EATON, J.K. 2010 Turbulent dispersed multiphase flow. *Annu. Rev. Fluid Mech.* **42** (1), 111–133.

BANANI, S.F., LEE, H.O., HYMAN, A.A. & ROSEN, M.K. 2017 Biomolecular condensates: organizers of cellular biochemistry. *Nat. Rev. Mol. Cell Biol.* **18** (5), 285–298.

BANDAK, D., GOLDENFELD, N., MAILYBAEV, A.A. & EYINK, G. 2022 Dissipation-range fluid turbulence and thermal noise. *Phys. Rev. E* **105** (6), 065113.

BARDOS, C. & TITI, E. 2007 Euler equations for incompressible ideal fluids. *Russian Math. Surv.* **62** (3), 409–451.

BARRETT, J.W., BLOWEY, J.F. & GARCKE, H. 1999 Finite element approximation of the Cahn–Hilliard equation with degenerate mobility. *SIAM J. Numer. Anal.* **37** (1), 286–318.

BARRETT, J.W., BLOWEY, J.F. & GARCKE, H. 2001 On fully practical finite element approximations of degenerate Cahn–Hilliard systems. *ESAIM: Math. Model. Numer. Anal.* **35** (4), 713–748.

BASU, A., SAIN, A., DHAR, S.K. & PANDIT, R. 1998 Multiscaling in models of magnetohydrodynamic turbulence. *Phys. Rev. Lett.* **81** (13), 2687–2690.

BATCHELOR, G.K. 1967 *An Introduction to Fluid Dynamics*. Cambridge University Press.

BAXTER, R.J. 2016 *Exactly Solved Models in Statistical Mechanics*. Elsevier.

BEALE, J., KATO, T. & MAJDA, A. 1984 Remarks on the breakdown of smooth solutions for the 3-D Euler equations. *Commun. Math. Phys.* **94** (1), 61–66.

BENZI, R. & CHING, E.S. 2018 Polymers in fluid flows. *Annu. Rev. Condens. Matter Phys.* **9** (1), 163–181.

BENZI, R. & SUCCI, S. 1990 Two-dimensional turbulence with the lattice Boltzmann equation. *J. Phys. A: Math. Gen.* **23** (1), L1–L5.

BENZI, R., SUCCI, S. & VERGASSOLA, M. 1992 The lattice Boltzmann equation: theory and applications. *Phys. Rep.* **222** (3), 145–197.

BERTI, S., BISTAGNINO, A., BOFFETTA, G., CELANI, A. & MUSACCHIO, S. 2008 Two-dimensional elastic turbulence. *Phys. Rev. E* **77** (5), 055306.

BERTI, S., BOFFETTA, G., CENCINI, M. & VULPIANI, A. 2005 Turbulence and coarsening in active and passive binary mixtures. *Phys. Rev. Lett.* **95** (22), 224501.

BETCHOV, R. 1977 Transition. In *Handbook of Turbulence*, vol. 1 *Fundamentals and Applications*, pp. 147–164. Springer.

BHATTACHARJEE, J. & KIRKPATRICK, T. 2022 Activity induced turbulence in driven active matter. *Phys. Rev. Fluids* **7** (3), 034602.

BINDER, K., KALOS, M., LEBOWITZ, J. & MARRO, J. 1979 Computer experiments on phase separation in binary alloys. *Adv. Colloid Interface* **10** (1), 173–214.

BISTAFA, S.R. 2018 On the development of the Navier–Stokes equation by Navier. *Rev. Bras. Ensino Fís.* **40** (2), e2603.

BODENSCHATZ, E., MALINOWSKI, S.P., SHAW, R.A. & STRATMANN, F. 2010 Can we understand clouds without turbulence? *Science* **327** (5968), 970–971.

BOFFETTA, G. & ECKE, R.E. 2012 Two-dimensional turbulence. *Annu. Rev. Fluid Mech.* **44** (1), 427–451.

BOFFETTA, G., MAZZINO, A., MUSACCHIO, S. & VOZELLA, L. 2010*a* Rayleigh–Taylor instability in a viscoelastic binary fluid. *J. Fluid Mech.* **643**, 127–136.

BOFFETTA, G., MAZZINO, A., MUSACCHIO, S. & VOZELLA, L. 2010*b* Statistics of mixing in three-dimensional Rayleigh–Taylor turbulence at low Atwood number and Prandtl number one. *Phys. Fluids* **22** (3).

BONHOMME, R., MAGNAUDET, J., DUVAL, F. & PIAR, B. 2012 Inertial dynamics of air bubbles crossing a horizontal fluid–fluid interface. *J. Fluid Mech.* **707**, 405–443.

BORCIA, R., BORCIA, I.D., BESTEHORN, M., SHARMA, D. & AMIROUDINE, S. 2022 Phase field modeling in liquid binary mixtures: isothermal and nonisothermal problems. *Phys. Rev. Fluids* **7** (6), 064005.

BOUROUIBA, L. 2021 The fluid dynamics of disease transmission. *Annu. Rev. Fluid Mech.* **53** (1), 473–508.

BOYER, F. & LAPUERTA, C. 2006 Study of a three component Cahn–Hilliard flow model. *ESAIM: Math. Model. Numer. Anal.* **40** (4), 653–687.

BOYER, F., LAPUERTA, C., MINJEAUD, S., PIAR, B. & QUINTARD, M. 2010 Cahn–Hilliard/Navier–Stokes model for the simulation of three-phase flows. *Transp. Porous Med.* **82** (3), 463–483.

BRATANOV, V., JENKO, F. & FREY, E. 2015 New class of turbulence in active fluids. *Proc. Natl Acad. Sci. USA* **112** (49), 15048–15053.

BRAUNS, F. & MARCHETTI, M. 2024 Nonreciprocal pattern formation of conserved fields. *Phys. Rev. X* **14** (2), 021014.

BRAY, A.J. 2002 Theory of phase-ordering kinetics. *Adv. Phys.* **51** (2), 481–587.

BRENNEN, C.E. 2005 *Fundamentals of Multiphase Flow*. Cambridge University Press.

BUARIA, D. & SREENIVASAN, K.R. 2022 Intermittency of turbulent velocity and scalar fields using three-dimensional local averaging. *Phys. Rev. Fluids* **7** (7), L072601.

BUARIA, D. & SREENIVASAN, K.R. 2023 Forecasting small scale dynamics of fluid turbulence using deep neural networks. *Proc. Natl Acad. Sci. USA* **120** (30).

BUDIANA, E.P., PRANOWO, INDARTO & DEENDARLIANTO 2020 The meshless numerical simulation of Kelvin–Helmholtz instability during the wave growth of liquid–liquid slug flow. *Comput. Math. Applics.* **80** (7), 1810–1838.

CAGINALP, G. & FISHER, M.E. 1979 Wall and boundary free energies: II. General domains and complete boundaries. *Commun. Math. Phys.* **65** (3), 247–280.

CAHN, J.W. 1961 On spinodal decomposition. *Acta Metall.* **9** (9), 795–801.

CAHN, J.W. 1977 Critical point wetting. *J. Chem. Phys.* **66** (8), 3667–3672.

CAHN, J.W. & HILLIARD, J.E. 1958 Free energy of a nonuniform system. I. Interfacial free energy. *J. Chem. Phys.* **28** (2), 258–267.

CAHN, J.W. & HILLIARD, J.E. 1959 Free energy of a nonuniform system. III. Nucleation in a two-component incompressible fluid. *J. Chem. Phys.* **31** (3), 688–699.

CANUTO, C., HUSSAINI, M. & QUARTERONI, A. 1988 *Spectral Methods in Fluid Dynamics*, p. 275. Springer-Verlag.

CATES, M. & NARDINI, C. 2024 Active phase separation: new phenomenology from non-equilibrium physics. arXiv preprint arXiv: 2412.02854.

CATES, M.E. & TAILLEUR, J. 2015 Motility-induced phase separation. *Annu. Rev. Condens. Matter Phys.* **6** (1), 219–244.

CELANI, A., MAZZINO, A., MURATORE-GINANNESCHI, P. & VOZELLA, L. 2009 Phase-field model for the Rayleigh–Taylor instability of immiscible fluids. *J. Fluid Mech.* **622**, 115–134.

CELANI, A., MUSACCHIO, S. & VINCENZI, D. 2010 Turbulence in more than two and less than three dimensions. *Phys. Rev. Lett.* **104** (18), 184506.

CHAIKIN, P.M., LUBENSKY, T.C. & WITTEN, T.A. 1995 *Principles of Condensed Matter Physics*, vol. 10. Cambridge University Press.

CHARRU, F. 2011 *Hydrodynamic Instabilities*, vol. 37. Cambridge University Press.

CHEN, S. & DOOLEN, G.D. 1998 Lattice Boltzmann method for fluid flows. *Annu. Rev. Fluid Mech.* **30** (1), 329–364.

CHOI, K. & PARK, H. 2021 Interfacial phenomena of the interaction between a liquid–liquid interface and rising bubble. *Exp. Fluids* **62** (6), 126.

CHOWDHURY, I.U., MAHAPATRA, P.S. & SEN, A.K. 2022 A wettability pattern-mediated trapped bubble removal from a horizontal liquid–liquid interface. *Phys. Fluids* **34** (4), 042109.

COLAGROSSI, A. & LANDRINI, M. 2003 Numerical simulation of interfacial flows by smoothed particle hydrodynamics. *J. Comput. Phys.* **191** (2), 448–475.

CONSTANTIN, P. & FOIAŞ, C. 1988 *Navier–Stokes Equations*. University of Chicago Press.

COOLEY, J.W. & TUKEY, J.W. 1965 An algorithm for the machine calculation of complex Fourier series. *Maths Comput.* **19** (90), 297–301.

COX, S.M. & MATTHEWS, P.C. 2002 Exponential time differencing for stiff systems. *J. Comput. Phys.* **176** (2), 430–455.

CUSHMAN-ROISIN, B. 2005 Kelvin–Helmholtz instability as a boundary-value problem. *Environ. Fluid Mech.* **5** (6), 507–525.

DARRIGOL, O. 2005 *Worlds of Flow: A History of Hydrodynamics From the Bernoullis to Prandtl*. Oxford University Press.

DARRIGOL, O. & FRISCH, U. 2008 From Newton's mechanics to Euler's equations. *Phys. D: Nonlinear Phenom.* **237** (14-17), 1855–1869.

DAS, A., BHATTACHARJEE, J. & KIRKPATRICK, T. 2020 Transition to turbulence in driven active matter. *Phys. Rev. E* **101** (2), 023103.

DELAMERE, P.A., BARNES, N.P., MA, X. & JOHNSON, J.R. 2021 The Kelvin–Helmholtz instability from the perspective of hybrid simulations. *Front. Astron. Space Sci.* **8**, 801824.

DEVENISH, B. *et al.*et al. 2012 Droplet growth in warm turbulent clouds. *Q. J. R. Meteorol. Soc.* **138** (667), 1401–1429.

DÍAZ-DAMACILLO, L., SIGALOTTI, L.D.G., ALVARADO-RODRÍGUEZ, C.E. & KLAPP, J. 2023 Smoothed particle hydrodynamics simulations of the evaporation of suspended liquid droplets. *Phys. Fluids* **35** (12), 122111.

DIETRICH, N., PONCIN, S., PHEULPIN, S. & LI, H.Z. 2008 Passage of a bubble through a liquid–liquid interface. *AIChE J.* **54** (3), 594–600.

DLOTKO, T. 1994 Global attractor for the Cahn–Hilliard equation in h2 and h3. *J. Differ. Equ.* **113** (2), 381–393.

DLOTKO, T. 2022 Navier–Stokes–Cahn–Hilliard system of equations. *J. Math. Phys.* **63** (11), 111511.

DOERING, C.R. 2009 The 3D Navier–Stokes problem. *Annu. Rev. Fluid Mech.* **41** (1), 109–128.

DOERING, C.R. & GIBBON, J.D. 1995 *Applied Analysis of the Navier–Stokes Equations*. Cambridge University Press.

DONZIS, D.A., GIBBON, J.D., GUPTA, A., KERR, R.M., PANDIT, R. & VINCENZI, D. 2013 Vorticity moments in four numerical simulations of the 3D Navier–Stokes equations. *J. Fluid Mech.* **732**, 316–331.

DORBOLO, S., VANDEWALLE, N., REYSSAT, E. & QUÉRÉ, D. 2006 Vita brevis of antibubbles. *Europhys. News* **37** (4), 24–25.

DRAZIN, P.G. 2002 *Introduction to Hydrodynamic Stability*, vol. 32. Cambridge University Press.

DRITSCHEL, D.G. & TOBIAS, S.M. 2012 Two-dimensional magnetohydrodynamic turbulence in the small magnetic Prandtl number limit. *J. Fluid Mech.* **703**, 85–98.

DRIVAS, T.D. & ELGINDI, T.M. 2023 Singularity formation in the incompressible Euler equation in finite and infinite time. *EMS Surv. Math. Sci.* **10** (1), 1–100.

DUNKEL, J., HEIDENREICH, S., BÄR, M. & GOLDSTEIN, R.E. 2013 Minimal continuum theories of structure formation in dense active fluids. *New J. Phys.* **15** (4), 045016.

EBENBECK, M., GARCKE, H. & NÜRNBERG, R. 2020 Cahn–Hilliard–Brinkman systems for tumour growth. arXiv preprint arXiv: 2003.08314.

ELLIOTT, C.M. & FRENCH, D.A. 1987 Numerical studies of the Cahn–Hilliard equation for phase separation. *IMA J. Appl. Maths* **38** (2), 97–128.

ELLIOTT, C.M. & MIKELIĆ, A. 1991 Existence for the Cahn–Hilliard phase separation model with a nondifferentiable energy. *Ann. Mat. Pura Appl.* **158** (1), 181–203.

ELLIOTT, C.M. & SONGMU, Z. 1986 On the Cahn–Hilliard equation. *Archive Ration. Mech. Anal.* **96** (4), 339–357.

EMERY, T.S. & KANDLIKAR, S.G. 2019 Modeling bubble collisions at liquid-liquid and compound interfaces. *Langmuir* **35** (25), 8294–8307.

EMERY, T.S., RAGHUPATHI, P.A. & KANDLIKAR, S.G. 2018 Flow regimes and transition criteria during passage of bubbles through a liquid–liquid interface. *Langmuir* **34** (23), 6766–6776.

ENGELS, T., KOLOMENSKIY, D., SCHNEIDER, K. & SESTERHENN, J. 2016 Flusi: a novel parallel simulation tool for flapping insect flight using a Fourier method with volume penalization. *SIAM J. Sci. Comput.* **38** (5), S3–S24.

ENGELS, T., TRUONG, H., FARGE, M., KOLOMENSKIY, D. & SCHNEIDER, K. 2022 Computational aerodynamics of insect flight using volume penalization. *C. R. Méc.* **350** (S1), 1–20.

EULER, L. 1761, Principia motus fluidorum. *Novi Commentarii Academiae Scientiarum Petropolitanae*, 271–311.

FALK, H. 1970 Inequalities of J. W. Gibbs. *Am. J. Phys.* **38** (7), 858–869.

FAN, X., DIAMOND, P. & CHACÓN, L. 2017 Formation and evolution of target patterns in Cahn–Hilliard flows. *Phys. Rev. E* **96** (4), 041101.

FAN, X., DIAMOND, P. & CHACÓN, L. 2018 CHNS: a case study of turbulence in elastic media. *Phys. Plasmas* **25** (5), 055702.

FAN, X., DIAMOND, P., CHACÓN, L. & LI, H. 2016 Cascades and spectra of a turbulent spinodal decomposition in two-dimensional symmetric binary liquid mixtures. *Phys. Rev. Fluids* **1** (5), 054403.

FARWIG, R. 2021 From Jean Leray to the millennium problem: the Navier–Stokes equations. *J. Evol. Equ.* **21** (3), 3243–3263.

FAUCHER-GIGUERE, C.-A. & OH, S. 2023 Key physical processes in the circumgalactic medium. *Annu. Rev. Astron. Astrophys.* **61** (1), 131–195.

FENG, J., MURADOGLU, M., KIM, H., AULT, J. T. & STONE, H.A. 2016 Dynamics of a bubble bouncing at a liquid/liquid/gas interface. *J. Fluid Mech.* **807**, 324–352.

FISHER, M.E., BARBER, M.N. & JASNOW, D. 1973 Helicity modulus, superfluidity, and scaling in isotropic systems. *Phys. Rev. A* **8** (2), 1111–1124.

FISHER, M.E. & CAGINALP, G. 1977 Wall and boundary free energies: I. Ferromagnetic scalar spin systems. *Commun. Math. Phys.* **56** (1), 11–56.

FISHER, M.P. & WORTIS, M. 1984 Curvature corrections to the surface tension of fluid drops: Landau theory and a scaling hypothesis. *Phys. Rev. B* **29** (11), 6252–6260.

FIXMAN, M. 1967 Transport coefficients in the gas critical region. *J. Chem. Phys.* **47** (8), 2808–2818.

FOGEDBY, H.C. & MOURITSEN, O.G. 1988 Lifshitz–Allen–Cahn domain-growth kinetics of Ising models with conserved density. *Phys. Rev. B* **37** (10), 5962–5965.

FOIAS, C., MANLEY, O., ROSA, R. & TEMAM, R. 2001 *Navier–Stokes Equations and Turbulence*, vol. 83. Cambridge University Press.

FORBES, L.K., TURNER, R.J. & WALTERS, S.J. 2022 An extended Boussinesq theory for interfacial fluid mechanics. *J. Engng Maths* **133** (1), 10.

FRIGO, M. & JOHNSON, S.G. 1998 FFTW: An adaptive software architecture for the FFT. In *Proceedings of the 1998 IEEE International Conference on Acoustics, Speech and Signal Processing, ICASSP'98 (Cat. No. 98CH36181)*, vol. 3, pp. 1381–1384. IEEE.

FROHOFF-HÜLSMANN, T. & THIELE, U. 2023 Nonreciprocal Cahn–Hilliard model emerges as a universal amplitude equation. *Phys. Rev. Lett.* **131** (10), 107201.

FURIHATA, D. 2001 A stable and conservative finite difference scheme for the Cahn–Hilliard equation. *Numer. Math.* **87** (4), 675–699.

FURUKAWA, H. 2000 Spinodal decomposition of two-dimensional fluid mixtures: a spectral analysis of droplet growth. *Phys. Rev. E* **61** (2), 1423–1431.

GAL, C.G. & GRASSELLI, M. 2010 Asymptotic behavior of a Cahn–Hilliard–Navier–Stokes system in 2D. *Annales De l'IHP Analyse Non Linéaire* **27**, 401–436.

GALDI, G.P. 2000 An introduction to the Navier–Stokes initial-boundary value problem. In *Fundamental Directions in Mathematical Fluid Mechanics*, pp. 1–70. Springer.

GAO, T. & LI, Z. 2017 Self-driven droplet powered by active nematics. *Phys. Rev. Lett.* **119** (10), 108002.

GARCKE, H., LAM, K.F. & SIGNORI, A. 2021 On a phase field model of Cahn–Hilliard type for tumour growth with mechanical effects. *Nonlinear Anal: Real World Applics.* **57**, 103192.

GAROOSI, F. & MAHDI, T.-F. 2022 Numerical simulation of three-fluid Rayleigh–Taylor instability using an enhanced Volume-Of-Fluid (VOF) model: new benchmark solutions. *Comput. Fluids* **245**, 105591.

GIBBON, J.D. 2008 The three-dimensional Euler equations: where do we stand? *Phys. D: Nonlinear Phenom.* **237** (14-17), 1894–1904.

GIBBON, J.D., DONZIS, D.A., GUPTA, A., KERR, R.M., PANDIT, R. & VINCENZI, D. 2014 Regimes of nonlinear depletion and regularity in the 3D Navier–Stokes equations. *Nonlinearity* **27** (10), 2605–2625.

GIBBON, J.D., GUPTA, A., KRSTULOVIC, G., PANDIT, R., POLITANO, H., PONTY, Y., POUQUET, A., SAHOO, G. & STAWARZ, J. 2016*a* Depletion of nonlinearity in magnetohydrodynamic turbulence: Insights from analysis and simulations. *Phys. Rev. E* **93** (4), 043104.

GIBBON, J.D., GUPTA, A., PAL, N. & PANDIT, R. 2018 The role of BKM-type theorems in 3D Euler, Navier–Stokes and Cahn–Hilliard–Navier–Stokes analysis. *Physica D: Nonlinear Phenom.* **376**, 60–68.

GIBBON, J.D., KIRAN, K.V., PADHAN, N.B. & PANDIT, R. 2023 An analytical and computational study of the incompressible Toner–Tu equations. *Phys. D: Nonlinear Phenom.* **444**, 133594.

GIBBON, J.D., PAL, N., GUPTA, A. & PANDIT, R. 2016*b* Regularity criterion for solutions of the three-dimensional Cahn–Hilliard–Navier–Stokes equations and associated computations. *Phys. Rev. E* **94** (6), 063103.

GIORGINI, A. 2021 Well-posedness of the two-dimensional Abels–Garcke–Grün model for two-phase flows with unmatched densities. *Calc. Varation Partial Differ Equ.* **60** (3), 100.

GIORGINI, A., MIRANVILLE, A. & TEMAM, R. 2019 Uniqueness and regularity for the Navier–Stokes–Cahn–Hilliard system. *SIAM J. Math. Anal.* **51** (3), 2535–2574.

GIORGINI, A. & TEMAM, R. 2020 Weak and strong solutions to the nonhomogeneous incompressible Navier–Stokes–Cahn–Hilliard system. *J. Math. Pures Appl.* **144**, 194–249.

GIRARDEAU, M. & MAZO, R. 1973 Variational methods in statistical mechanics. *Adv. Chem. Phys.* **140**, 187–255.

GLAUBER, R.J. 1963 Time-dependent statistics of the Ising model. *J. Math. Phys.* **4** (2), 294–307.

GOLDENFELD, N. 2018 *Lectures On Phase Transitions and the Renormalization Group*. CRC Press.

GÓMEZ, D.O., MININNI, P.D. & DMITRUK, P. 2005 Parallel simulations in turbulent MHD. *Phys. Scr.* **2005** (T116), 123–127.

GONZALEZ-GUTIÉRREZ, L.M. & DE ANDREA GONZÁLEZ, A. 2019 Numerical computation of the Rayleigh–Taylor instability for a viscous fluid with regularized interface properties. *Phys. Rev. E* **100** (1), 013101.

GOULD, H., TOBOCHNIK, J., MEREDITH, D.C., KOONIN, S.E., MCKAY, S.R. & CHRISTIAN, W. 1996 An introduction to computer simulation methods: applications to physical systems. *Comput. Phys.* **10** (4), 349–349.

GOUVEIA, B., KIM, Y., SHAEVITZ, J.W., PETRY, S., STONE, H.A. & BRANGWYNNE, C.P. 2022 Capillary forces generated by biomolecular condensates. *Nature* **609** (7926), 255–264.

GREGG, M.C., D'ASARO, E.A., RILEY, J.J. & KUNZE, E. 2018 Mixing efficiency in the ocean. *Annu. Rev. Mar. Sci.* **10** (1), 443–473.

GRIFFITHS, R.B. 1972 Rigorous results and theorems. *Phase Transitions Crit. Phenom.* **1**, 7–109.

GROISMAN, A. & STEINBERG, V. 2000 Elastic turbulence in a polymer solution flow. *Nature* **405** (6782), 53–55.

GUNTON, J., SAN MIGUEL, M. & SAHNI, P. 1983 The dynamics of first order phase transitions. In *Phase Transitions and Critical Phenomena* (eds. Domb, C & Lebowitz, J.L.), vol. 8. Academic Press.

GUO, Z., YU, F., LIN, P., WISE, S. & LOWENGRUB, J. 2021 A diffuse domain method for two-phase flows with large density ratio in complex geometries. *J. Fluid Mech.* **907**, A38.

GUPTA, A. & PANDIT, R. 2017 Melting of a nonequilibrium vortex crystal in a fluid film with polymers: elastic versus fluid turbulence. *Phys. Rev. E* **95** (3), 033119.

GUPTA, A., PERLEKAR, P. & PANDIT, R. 2015 Two-dimensional homogeneous isotropic fluid turbulence with polymer additives. *Phys. Rev. E* **91** (3), 033013.

GURTIN, M.E., POLIGNONE, D. & VINALS, J. 1996 Two-phase binary fluids and immiscible fluids described by an order parameter. *Math. Models Meth. Appl. Sci.* **6** (06), 815–831.

HEINEN, M., HOFFMANN, M., DIEWALD, F., SECKLER, S., LANGENBACH, K. & VRABEC, J. 2022 Droplet coalescence by molecular dynamics and phase-field modeling. *Phys. Fluids* **34** (4), 042006.

HERTEL, T., BESSE, N. & FRISCH, U. 2022 The Cauchy–Lagrange method for 3D-axisymmetric wall-bounded and potentially singular incompressible Euler flows. *J. Comput. Phys.* **449**, 110758.

HESTER, E.W., CARNEY, S., SHAH, V., ARNHEIM, A., PATEL, B., DI CARLO, D. & BERTOZZI, A.L. 2023 Fluid dynamics alters liquid–liquid phase separation in confined aqueous two-phase systems. *Proc. Natl Acad. Sci. USA* **120** (49), e2306467120.

HESTER, E.W., VASIL, G.M. & BURNS, K.J. 2021 Improving accuracy of volume penalised fluid-solid interactions. *J. Comput. Phys.* **430**, 110043.

HILHORST, D., KAMPMANN, J., NGUYEN, T.N., VAN DER, Z. & GEORGE, K. 2015 Formal asymptotic limit of a diffuse-interface tumor-growth model. *Math. Models Meth. Appl. Sci.* **25** (06), 1011–1043.

HILL, J.D. & MILLETT, P.C. 2017 Numerical simulations of directed self-assembly in diblock copolymer films using zone annealing and pattern templating. *Sci. Rep.* **7** (1), 5250.

HOHENBERG, P.C. & HALPERIN, B.I. 1977 Theory of dynamic critical phenomena. *Rev. Mod. Phys.* **49** (3), 435–479.

HOSHOUDY, G. & CAVUS, H. 2018 Kelvin–Helmholtz instability of two finite-thickness fluid layers with continuous density and velocity profiles. *J. Astrophys. Astron.* **39** (3), 1–10.

HOU, T., WEI, X., IQBAL, A., YANG, X., WANG, J., REN, Y. & YAN, S. 2024 Advances in biomedical fluid–structure interaction: methodologies and applications from an interfacing perspective. *Phys. Fluids* **36** (2), 021301.

HOU, T.Y. & LI, R. 2007 Computing nearly singular solutions using pseudo-spectral methods. *J. Comput. Phys.* **226** (1), 379–397.

HUANG, C., DE LA CRUZ, M. & SWIFT, B. 1995 Phase separation of ternary mixtures: symmetric polymer blends. *Macromolecules* **28** (24), 7996–8005.

HUANG, K. 2008 *Statistical Mechanics*. John Wiley & Sons.

HUANG, Q. & YANG, J. 2022 Linear and energy-stable method with enhanced consistency for the incompressible Cahn–Hilliard–Navier–Stokes two-phase flow model. *Mathematics* **10** (24), 4711.

HUAT, T.C. 2015 *Fluid-Structure Interaction of Multiphase Flow Within a Pipe Bend*. IRC.

HUGHES, W. & HUGHES, A.R. 1932 Liquid drops on the same liquid surface. *Nature* **129** (3245), 59.

JAIN, P., RANA, N., RAMASWAMY, S. & PERLEKAR, P. 2024 Inertia drives concentration-wave turbulence in swimmer suspensions. *Phys. Rev. Lett.* **133** (15), 158302.

JESKE, S.R., WESTHOFEN, L., LÖSCHNER, F., FERNÁNDEZ-FERNÁNDEZ, J.A. & BENDER, J. 2023 Implicit surface tension for sph fluid simulation. *ACM Trans. Graph.* **43** (1), 1–14.

JIA, B.-Q., XIE, L., DENG, X.-D., HE, B.-S., YANG, L.-J. & FU, Q.-F. 2023 Experimental study on the oscillatory Kelvin–Helmholtz instability of a planar liquid sheet in the presence of axial oscillating gas flow. *J. Fluid Mech.* **959**, A18.

JOHANSEN, K., KOTOPOULIS, S., POORTINGA, A.T. & POSTEMA, M. 2015*a* Nonlinear echoes from encapsulated antibubbles. *Phys. Procedia* **70**, 1079–1082.

JOHANSEN, K., KOTOPOULIS, S. & M., POSTEMA, 2015*b* Ultrasonically driven antibubbles encapsulated by Newtonian fluids for active leakage detection. *Lecture Notes Engng. Comput. Sci.* **2216**, 750–754.

JOHNSON, R.E. & SADHAL, S. 1985 Fluid mechanics of compound multiphase drops and bubbles. *Annu. Rev. Fluid Mech.* **17** (1), 289–320.

KADANOFF, L.P., GÖTZE, W., HAMBLEN, D., HECHT, R., LEWIS, E., PALCIAUSKAS, V., RAYL, M., SWIFT, J., ASPNES, D. & KANE, J. 1967 Static phenomena near critical points: theory and experiment. *Rev. Mod. Phys.* **39** (2), 395–431.

KADAU, K., GERMANN, T.C., HADJICONSTANTINOU, N.G., LOMDAHL, P.S., DIMONTE, G., HOLIAN, B.L. & ALDER, B.J. 2004 Nanohydrodynamics simulations: an atomistic view of the Rayleigh–Taylor instability. *Proc. Natl. Acad. Sci.* **101** (16), 5851–5855.

KADOCH, B., KOLOMENSKIY, D., ANGOT, P. & SCHNEIDER, K. 2012 A volume penalization method for incompressible flows and scalar advection–diffusion with moving obstacles. *J. Comput. Phys.* **231** (12), 4365–4383.

KALELKAR, C. 2017 The inveterate tinkerer: 7. Antibubbles. *Resonance* **22** (9), 873–878.

KARDAR, M. 2007 *Statistical Physics of Fields*. Cambridge University Press.

KAWASAKI, K. 1966 Diffusion constants near the critical point for time-dependent Ising models. I. *Phys. Rev.* **145** (1), 224–230.

KAWASAKI, K. 1970 Kinetic equations and time correlation functions of critical fluctuations. *Ann. Phys.* **61** (1), 1–56.

KHAN, S.A. & SHAH, A. 2019 Simulation of the two-dimensional Rayleigh–Taylor instability problem by using diffuse-interface model. *AIP Adv.* **9** (8), 085312.

KHOMENKO, E., DÍAZ, A., DE, V., ANGEL, C., M, & LUNA, M. 2014 Rayleigh–Taylor instability in prominences from numerical simulations including partial ionization effects. *Astron. Astrophys.* **565**, A45.

KIM, J. 2007 Phase field computations for ternary fluid flows. *Comput. Meth. Appl. Mech. Engng* **196** (45-48), 4779–4788.

KIM, J. 2012 Phase-field models for multi-component fluid flows. *Commun. Comput. Phys.* **12** (3), 613–661.

KIM, J. & KANG, K. 2009 A numerical method for the ternary Cahn–Hilliard system with a degenerate mobility. *Appl. Numer. Maths* **59** (5), 1029–1042.

KIM, J., LEE, S., CHOI, Y., LEE, S.-M. & JEONG, D. 2016 Basic principles and practical applications of the Cahn–Hilliard equation. *Math. Prob. Engng* **2016**, 1–11.

KIM, J. & LOWENGRUB, J. 2005 Phase field modeling and simulation of three-phase flows. *Interface Free Bound.* **7** (4), 435–466.

KIM, P. & VOGEL, J. 2006 Antibubbles: factors that affect their stability. *Colloids Surf. A: Physicochem. Engng Aspects* **289** (1-3), 237–244.

KIRAN, K.V., GUPTA, A., VERMA, A.K. & PANDIT, R. 2023 Irreversibility in bacterial turbulence: insights from the mean-bacterial-velocity model. *Phys. Rev. Fluids* **8** (2), 023102.

KIRAN, K.V., KUMAR, K., GUPTA, A., PANDIT, R. & RAY, S.S. 2025 Onset of intermittency and multiscaling in active turbulence. *Phys. Rev. Lett.* **134** (8), 088302.

KOLLURU, S.S.V., SHARMA, P. & PANDIT, R. 2022 Insights from a pseudospectral study of a potentially singular solution of the three-dimensional axisymmetric incompressible Euler equation. *Phys. Rev. E* **105** (6), 065107.

KOLOMENSKIY, D. & SCHNEIDER, K. 2009 A Fourier spectral method for the Navier–Stokes equations with volume penalization for moving solid obstacles. *J. Comput. Phys.* **228** (16), 5687–5709.

KOTOPOULIS, S., DELALANDE, A., POPA, M., MAMAEVA, V., DIMCEVSKI, G., GILJA, O. H., POSTEMA, M., GJERTSEN, B.T. & MCCORMACK, E. 2014 Sonoporation-enhanced chemotherapy significantly reduces primary tumour burden in an orthotopic pancreatic cancer xenograft. *Mol. Imaging Biol.* **16** (1), 53–62.

KOTOPOULIS, S., JOHANSEN, K., GILJA, O.H., POORTINGA, A.T. & POSTEMA, M. 2015 Acoustically active antibubbles. *Acta Phys. Polonica A* **127** (1), 99–102.

KUMAR, K., BANDYOPADHYAY, P., SINGH, S., DHARODI, V.S. & SEN, A. 2023 Kelvin–Helmholtz instability in a compressible dust fluid flow. *Sci. Rep.* **13** (1), 3979.

KUMAR, R., ROHILLA, L. & DAS, A.K. 2019 Passage of a Taylor bubble through a stratified liquid–liquid interface. *Ind. Engng Chem. Res.* **59** (9), 3757–3771.

LAFAURIE, B., NARDONE, C., SCARDOVELLI, R., ZALESKI, S. & ZANETTI, G. 1994 Modelling merging and fragmentation in multiphase flows with surfer. *J. Comput. Phys.* **113** (1), 134–147.

LANDAU, L.D. & LIFSHITZ, E.M. 2013 *Statistical Physics*, vol. 5. Elsevier.

LANJEWAR, S. & RAMJI, S. 2024 Dynamics of a deformable compound droplet under pulsatile flow. *Phys. Fluids* **36** (8), 083301.

LEBOWITZ, J.L. & KALOS, M. 1976 Computer simulation of phase separation in a quenched binary alloy. *Scripta Metall.* **10** (1), 9–12.

LEE, H.G. & KIM, J. 2013 Numerical simulation of the three-dimensional Rayleigh–Taylor instability. *Comput. Math. Appl.* **66** (8), 1466–1474.

LEE, H.G. & KIM, J. 2015 Two-dimensional Kelvin–Helmholtz instabilities of multi-component fluids. *Eur. J. Mech. B/Fluids* **49**, 77–88.

LEMARIÉ-RIEUSSET, P.G. 2018 *The Navier–Stokes Problem in the 21st Century*. Chapman and Hall/CRC.

LERAY, J. 1934 Essai sur les mouvements plans d'un liquide visqueux que limitent des parois. *J. Math. Pures Appl.* **13**, 331–418.

LEVANT, M. & STEINBERG, V. 2014 Complex dynamics of compound vesicles in linear flow. *Phys. Rev. Lett.* **112** (13), 138106.

LHERM, V., DEGUEN, R., ALBOUSSIÈRE, T. & LANDEAU, M. 2021 Rayleigh–Taylor instability in drop impact experiments. *Phys. Rev. Fluids* **6** (11), 110501.

LHERM, V., DEGUEN, R., ALBOUSSIÈRE, T. & LANDEAU, M. 2022 Rayleigh–Taylor instability in impact cratering experiments. *J. Fluid Mech.* **937**, A20.

LI, E., AL-OTAIBI, S., VAKARELSKI, I.U. & THORODDSEN, S.T. 2014 Satellite formation during bubble transition through an interface between immiscible liquids. *J. Fluid Mech.* **744**, R1.

LI, G. & KOCH, D.L. 2022 Dynamics of a self-propelled compound droplet. *J. Fluid Mech.* **952**, A16.

LI, T. 2023 Molecular dynamics simulations of droplet coalescence and impact dynamics on the modified surfaces: a review. *Comput. Mater. Sci.* **230**, 112547.

LIFSHITZ, I. 1962 Kinetics of ordering during second-order phase transitions. *Sov. Phys. JETP* **15**, 939.

LIFSHITZ, I.M. & SLYOZOV, V.V. 1961 The kinetics of precipitation from supersaturated solid solutions. *J. Phys. Chem. Solids* **19** (1-2), 35–50.

LINKMANN, M., BOFFETTA, G., MARCHETTI, M. & ECKHARDT, B. 2019 Phase transition to large scale coherent structures in two-dimensional active matter turbulence. *Phys. Rev. Lett.* **122** (21), 214503.

LIU, C.C., QI, Y.W. & YIN, J.X. 2006 Regularity of solutions of the Cahn–Hilliard equation with non–constant mobility. *Acta Math. Sin.* **22** (4), 1139–1150.

LIU, H., LU, Y., LI, S., YU, Y. & SAHU, K.C. 2021 Deformation and breakup of a compound droplet in three-dimensional oscillatory shear flow. *Intl J. Multiphase Flow* **134**, 103472.

LIVESCU, D., WEI, T. & PETERSEN, M. 2011 Direct numerical simulations of Rayleigh–Taylor instability. *J. Phys.: Conf. Ser.* **318**, 082007.

LOTHE, J. & POUND, G.M. 1962 Reconsiderations of nucleation theory. *J. Chem. Phys.* **36** (8), 2080–2085.

LOWENGRUB, J. & TRUSKINOVSKY, L. 1998 Quasi–incompressible Cahn–Hilliard fluids and topological transitions. *Poc. R. Soc. Lond A: Math. Phys. Engng Sci.* **454**(1978), 2617–2654.

LOWENGRUB, J.S., RÄTZ, A. & VOIGT, A. 2009 Phase-field modeling of the dynamics of multicomponent vesicles: spinodal decomposition, coarsening, budding, and fission. *Phys. Rev. E* **79** (3), 031926.

LUO, G. & HOU, T.Y. 2014 Potentially singular solutions of the 3D axisymmetric Euler equations. *Proc. Natl Acad. Sci. USA* **111** (36), 12968–12973.

MA, S.-K. 2018 *Modern Theory of Critical Phenomena*. Routledge.

MAGNAUDET, J. & EAMES, I. 2000 The motion of high-Reynolds-number bubbles in inhomogeneous flows. *Annu. Rev. Fluid Mech.* **32** (1), 659–708.

MAGNAUDET, J. & MERCIER, M.J. 2020 Particles, drops, and bubbles moving across sharp interfaces and stratified layers. *Annu. Rev. Fluid Mech.* **52** (1), 61–91.

MAJDA, A.J., BERTOZZI, A.L. & OGAWA, A. 2002 Vorticity and incompressible flow. Cambridge texts in applied mathematics. *Appl. Mech. Rev.* **55** (4), B77–B78.

MAJUMDAR, S. & SOOD, A. 2011 Universality and scaling behavior of injected power in elastic turbulence in wormlike micellar gel. *Phys. Rev. E* **84** (1), 015302.

MANGA, M. & STONE, H. 1995 Low Reynolds number motion of bubbles, drops and rigid spheres through fluid–fluid interfaces. *J. Fluid Mech* **287**, 279–298.

MARCHETTI, M., JOANNY, J.-F., RAMASWAMY, S., LIVERPOOL, T. B., PROST, J., RAO, M. & SIMHA, R. 2013 Hydrodynamics of soft active matter. *Rev. Mod. Phys.* **85** (3), 1143–1189.

MARTINELLI, F. 2004 *Lectures on Glauber Dynamics for Discrete Spin Models*. Lecture on Probability Theory and Statistics (Saint-Flour 1997), p. 93. Springer.

MATHAI, V., LOHSE, D. & SUN, C. 2020 Bubbly and buoyant particle-laden turbulent flows. *Annu. Rev. Condens. Matter Phys.* **11** (1), 529–559.

MCHALE, G., AFIFY, N., ARMSTRONG, S., WELLS, G. G. & LEDESMA-AGUILAR, R. 2022 The liquid Young's law on slips: liquid–liquid interfacial tensions and zisman plots. *Langmuir* **38** (32), 10032–10042.

MCWILLIAMS, J.C. 1984 The emergence of isolated coherent vortices in turbulent flow. *J. Fluid Mech.* **146**, 21–43.

MERCADO, J.M., GOMEZ, D.C., VAN, D., SUN, C.& LOHSE, D. 2010 On bubble clustering and energy spectra in pseudo-turbulence. *J. Fluid Mech.* **650**, 287–306.

MEYER, M., DESBRUN, M., SCHRÖDER, P. & BARR, A.H. 2003 Discrete differential-geometry operators for triangulated 2-manifolds. In *Visualization and Mathematics III*, pp. 35–57. Springer.

MIRANVILLE, A. 2021 The Cahn–Hilliard equation: recent advances and applications. *Jahresber. Dtsch. Math. Ver.* **123**, 57–62.

MIRJALILI, S., IVEY, C.B. & MANI, A. 2019 Comparison between the diffuse interface and volume of fluid methods for simulating two-phase flows. *Intl J. Multiphase Flow* **116**, 221–238.

MISHIN, V. & TOMOZOV, V. 2016 Kelvin–Helmholtz instability in the solar atmosphere, solar wind and geomagnetosphere. *Solar Phys.* **291** (11), 3165–3184.

MITTAL, R. & IACCARINO, G. 2005 Immersed boundary methods. *Annu. Rev. Fluid Mech.* **37** (1), 239–261.

MITTAL, R. & SEO, J.H. 2023 Origin and evolution of immersed boundary methods in computational fluid dynamics. *Phys. Rev. Fluids* **8** (10), 100501.

MOERMAN, P.G., HOHENBERG, P.C., VANDEN-EIJNDEN, E. & BRUJIC, J. 2018 Emulsion patterns in the wake of a liquid–liquid phase separation front. *Proc. Natl Acad. Sci. USA* **115** (14), 3599–3604.

MOHAN, A. & TOMAR, G. 2024 Volume of fluid method: a brief review. *J. Indian Inst. Sci.* **104** (1), 1–20.

MOIN, P. & MAHESH, K. 1998 Direct numerical simulation: a tool in turbulence research. *Annu. Rev. Fluid Mech.* **30** (1), 539–578.

MOKBEL, D., ABELS, H. & ALAND, S. 2018 A phase-field model for fluid–structure interaction. *J. Comput. Phys.* **372**, 823–840.

MORALES, J.A., LEROY, M., BOS, W.J. & SCHNEIDER, K. 2014 Simulation of confined magnetohydrodynamic flows with dirichlet boundary conditions using a pseudo-spectral method with volume penalization. *J. Comput. Phys.* **274**, 64–94.

MUKHERJEE, S., SINGH, R.K., JAMES, M. & RAY, S.S. 2021 Anomalous diffusion and Lévy walks distinguish active from inertial turbulence. *Phys. Rev. Lett.* **127** (11), 118001.

MUKHERJEE, S., SINGH, R.K., JAMES, M. & RAY, S.S. 2023 Intermittency, fluctuations and maximal chaos in an emergent universal state of active turbulence. *Nat. Phys.* **19** (6), 1–7.

MÜLLER, W.-C. & BISKAMP, D. 2000 Scaling properties of three-dimensional magnetohydrodynamic turbulence. *Phys. Rev. Lett.* **84** (3), 475–478.

MÜNKEL, C. 1993 Large scale simulations of the kinetic ising model. *Intl J. Mod. Phys. C* **4** (06), 1137–1145.

NATSUI, S., TAKAI, H., KUMAGAI, T., KIKUCHI, T. & SUZUKI, R. O. 2014 Multiphase particle simulation of gas bubble passing through liquid/liquid interfaces. *Mater. Trans.* **55** (11), 1707–1715.

NAVIER, C. 1823 Mémoire sur les lois du mouvement des fluides. *Mémoires De l'Académie Royale Des Sciences De l'Institut De France* **6**(1823), 389–440.

NOTHARD, S., MCKENZIE, D., HAINES, J. & JACKSON, J. 1996 Gaussian curvature and the relationship between the shape and the deformation of the Tonga slab. *Geophys. J. Intl.* **127** (2), 311–327.

OKI, K., SAGANE, H. & EGUCHI, T. 1977 Separation and domain structure . . . in Fe-Al alloys. *J. Phys. Colloques* **38-38** (C7), 414–417.

ONSAGER, L. 1944 Crystal statistics. i. a two-dimensional model with an order-disorder transition. *Phys. Rev.* **65** (3-4), 3–4,117.

ONUKI, A. 2002 *Phase Transition Dynamics*. Cambridge University Press.

ORSZAG, S. A. 1971 On the elimination of aliasing in finite-difference schemes by filtering high-wavenumber components. *J. Atmos. Sci.* **28** (6), 1074–1074.

ORSZAG, S.A. & PAO, Y.-H. 1975 Numerical computation of turbulent shear flows. In *Advances in Geophysics*, vol. 18, pp. 225–236. Elsevier.

PADHAN, N.B., KIRAN, K.V. & PANDIT, R. 2024*a* Novel turbulence and coarsening arrest in active-scalar fluids. *Soft Matter* **20** (17), 3620–3627.

PADHAN, N.B. & PANDIT, R. 2023*a* Activity-induced droplet propulsion and multifractality. *Phys. Rev. Res.* **5** (3), L032013.

PADHAN, N.B. & PANDIT, R. 2023*b* Unveiling the spatiotemporal evolution of liquid-lens coalescence: self-similarity, vortex quadrupoles, and turbulence in a three-phase fluid system. *Phys. Fluids* **35** (11), 112105.

PADHAN, N.B. & PANDIT, R. 2024 Interfaces as transport barriers in two-dimensional Cahn–Hilliard–Navier–Stokes turbulence. arXiv preprint arXiv: 2404.17770.

PADHAN, N.B., VINCENZI, D. & PANDIT, R. 2024*b* Interface-induced turbulence in viscous binary fluid mixtures. *Phys. Rev. Fluids* **9** (12), L122401.

PADHAN, N.B. & VOIGT, A. 2025 Suppression of hyperuniformity in hydrodynamic scalar active field theories. *J. Phys.: Condens. Matter* **37** (10), 105101.

PAL, N. 2016 Cahn–Hilliard–Navier–Stokes investigations of binary-fluid turbulence and droplet dynamics. PhD thesis. Indian Institute of Science, Bangalore, India.

PAL, N., PERLEKAR, P., GUPTA, A. & PANDIT, R. 2016 Binary-fluid turbulence: signatures of multifractal droplet dynamics and dissipation reduction. *Phys. Rev. E* **93** (6), 063115.

PAL, N., RAMADUGU, R., PERLEKAR, P. & PANDIT, R. 2022 Ephemeral antibubbles: spatiotemporal evolution from direct numerical simulations. *Phys. Rev. Res.* **4** (4), 043128.

PAN, J., XING, C. & LUO, H. 2020 Uniform regularity of the weak solution to higher-order Navier–Stokes–Cahn–Hilliard systems. *J. Math. Anal. Applics.* **486** (2), 123925.

PANDEY, V., MITRA, D. & PERLEKAR, P. 2023 Kolmogorov turbulence coexists with pseudo-turbulence in buoyancy-driven bubbly flows. *Phys. Rev. Lett.* **131** (11), 114002.

PANDEY, V., RAMADUGU, R. & PERLEKAR, P. 2020 Liquid velocity fluctuations and energy spectra in three-dimensional buoyancy-driven bubbly flows. *J. Fluid Mech.* **884**, R6.

PANDIT, R. *et al.* 2017 An overview of the statistical properties of two-dimensional turbulence in fluids with particles, conducting fluids, fluids with polymer additives, binary-fluid mixtures, and superfluids. *Phys. Fluids* **29** (11), 111112.

PANDIT, R., FORGACS, G. & RUJAN, P. 1981 Finite-size calculations for the kinetic Ising model. *Phys. Rev. B* **24** (3), 1576–1578.

PANDIT, R., PERLEKAR, P. & RAY, S.S. 2009 Statistical properties of turbulence: an overview. *Pramana* **73** (1), 157–191.

PANDIT, R., SCHICK, M. & WORTIS, M. 1982 Systematics of multilayer adsorption phenomena on attractive substrates. *Phys. Rev. B* **26** (9), 5112–5140.

PANDIT, R. & WORTIS, M. 1982 Surfaces and interfaces of lattice models: mean-field theory as an area-preserving map. *Phys. Rev. B* **25** (5), 3226–3241.

PANDYA, G. & SHKOLLER, S. 2023 Interface models for three-dimensional Rayleigh–Taylor instability. *J. Fluid Mech.* **959**, A10.

PATTERSON, G.S.Jr. & ORSZAG, S.A. 1971 Interface models for three-dimensional Rayleigh–Taylor instability. *Phys. Fluids* **14** (11), 2538–2541.

PAULSEN, J.D., BURTON, J.C. & NAGEL, S.R. 2011 Viscous to inertial crossover in liquid drop coalescence. *Phys. Rev. Lett.* **106** (11), 114501.

PAULSEN, J.D., CARMIGNIANI, R., KANNAN, A., BURTON, J.C. & NAGEL, S.R. 2014 Coalescence of bubbles and drops in an outer fluid. *Nat. Commun.* **5** (1), 3182.

PAVULURI, S., HOLTZMAN, R., KAZEEM, L., MOHAMMED, M., SEERS, T.D. & RABBANI, H.S. 2023 Interplay of viscosity and wettability controls fluid displacement in porous media. *Phys. Rev. Fluids* **8** (9), 094002.

PERLEKAR, P., BENZI, R., CLERCX, H.J., NELSON, D.R. & TOSCHI, F. 2014 Spinodal decomposition in homogeneous and isotropic turbulence. *Phys. Rev. Lett.* **112** (1), 014502.

PERLEKAR, P., MITRA, D. & PANDIT, R. 2006 Manifestations of drag reduction by polymer additives in decaying, homogeneous, isotropic turbulence. *Phys. Rev. Lett.* **97** (26), 264501.

PERLEKAR, P., MITRA, D. & PANDIT, R. 2010 Direct numerical simulations of statistically steady, homogeneous, isotropic fluid turbulence with polymer additives. *Phys. Rev. E* **82** (6), 066313.

PERLEKAR, P., PAL, N. & PANDIT, R. 2017 Two-dimensional turbulence in symmetric binary-fluid mixtures: coarsening arrest by the inverse cascade. *Sci. Rep.* **7** (1), 44589.

PERLEKAR, P. & PANDIT, R. 2010 Turbulence-induced melting of a nonequilibrium vortex crystal in a forced thin fluid film. *New J. Phys.* **12** (2), 023033.

PISEGNA, G., RANA, N., GOLESTANIAN, R. & SAHA, S. 2025 Can hydrodynamic interactions destroy travelling waves formed by non-reciprocity? arXiv preprint arXiv: 2501.01330.

PLAN, E.L.C.IV, GUPTA, A., VINCENZI, D. & GIBBON, J.D. 2017 Lyapunov dimension of elastic turbulence. *J. Fluid Mech.* **822**, R4.

PLISCHKE, M. & BERGERSEN, B. 1994 *Equilibrium Statistical Physics*. World Scientific.

POPINET, S. & ZALESKI, S. 1999 A front-tracking algorithm for accurate representation of surface tension. *Intl J. Numer. Meth. Fluids* **30** (6), 775–793.

PRAMANIK, R., VERSTAPPEN, R. & ONCK, P. 2024 Computational fluid–structure interaction in biology and soft robots: a review. *Phys. Fluids* **36** (10), 101302.

PROSPERETTI, A. 2017 Vapor bubbles. *Annu. Rev. Fluid Mech.* **49** (1), 221–248.

PROSPERETTI, A. & TRYGGVASON, G. 2007 Introduction: a computational approach to multiphase flow. *Comput. Meth. Multiphase Flow* 1–19.

LEONARDO, P., GUIDO, B. & STEFANO, M. 2023 Flocking turbulence of microswimmers in confined domains. *Phys. Rev. E* **107** (5), 055107.

PURI, S. 2004 Kinetics of phase transitions. *Phase Transition* **77** (5-7), 407–431.

PURI, S. & WADHAWAN, V. 2009 *Kinetics of Phase Transitions*. CRC Press.

RABBANI, G. & RAY, B. 2024 Interaction of inline bubbles with immiscible liquids interface. *Chem. Engng Sci.* **286**, 119647.

RAMADUGU, R., PERLEKAR, P. & GOVINDARAJAN, R. 2022 Surface tension as the destabiliser of a vortical interface. *J. Fluid Mech.* **936**, A45.

RAMIREZ, F. & DIAMOND, P. 2024 Staircase resiliency in a fluctuating cellular array. *Phys. Rev. E* **109** (2), 025209.

RANA, N., CHATTERJEE, R., RO, S., LEVINE, D., RAMASWAMY, S. & PERLEKAR, P. 2024 Defect turbulence in a dense suspension of polar, active swimmers. *Phys. Rev. E* **109** (2), 024603.

RANA, N. & PERLEKAR, P. 2020 Coarsening in the two-dimensional incompressible Toner–Tu equation: Signatures of turbulence. *Phys. Rev. E* **102** (3), 032617.

RÄTZ, A. & VOIGT, A. 2006 PDE's on surfaces—a diffuse interface approach. *Commun. Math. Sci.* **4** (3), 575–590.

ROBINSON, J.C. 2020 The Navier–Stokes regularity problem. *Phil. Trans. R. Soc. Lond. A* **378** (2174), 20190526.

ROBINSON, J.C., RODRIGO, J.L. & SADOWSKI, W. 2016 The three-dimensional Navier–Stokes equations. In *Classical Theory*, vol. 157, Cambridge University Press.

ROTTMAN, C. & WORTIS, M. 1984 Statistical mechanics of equilibrium crystal shapes: interfacial phase diagrams and phase transitions. *Phys. Rep.* **103** (1-4), 59–79.

ROWLINSON, J.S. & WIDOM, B. 2013 *Molecular Theory of Capillarity*. Courier Corporation.

RUBINSTEIN, M. & COLBY, R. 2003 *Polymer Physics*. Oxford University Press.

SAHA, S., AGUDO-CANALEJO, J. & GOLESTANIAN, R. 2020 Scalar active mixtures: the nonreciprocal Cahn–Hilliard model. *Phys. Rev. X* **10** (4), 041009.

SAHOO, G., PADHAN, N.B., BASU, A. & PANDIT, R. 2020 Direct numerical simulations of three-dimensional magnetohydrodynamic turbulence with random, power-law forcing. arXiv preprint arXiv: 2011.04277.

SAHOO, G., PERLEKAR, P. & PANDIT, R. 2011 Systematics of the magnetic-Prandtl-number dependence of homogeneous, isotropic magnetohydrodynamic turbulence. *New J. Phys.* **13** (1), 013036.

SAN, O. & STAPLES, A.E. 2012 High-order methods for decaying two-dimensional homogeneous isotropic turbulence. *Comput. Fluids* **63**, 105–127.

SANTRA, S., PANIGRAHI, D.P., DAS, S. & CHAKRABORTY, S. 2020 Shape evolution of compound droplet in combined presence of electric field and extensional flow. *Phys. Rev. Fluids* **5** (6), 063602.

SCARBOLO, L. & SOLDATI, A. 2013 Turbulence modulation across the interface of a large deformable drop. *J. Turbul.* **14** (11), 27–43.

SCHEEL, T., XIE, Q., SEGA, M. & HARTING, J. 2023 Viscous to inertial coalescence of liquid lenses: a lattice Boltzmann investigation. *Phys. Rev. Fluids* **8** (7), 074201.

SCHEID, B., DORBOLO, S., ARRIAGA, L.R. & RIO, E. 2012 Antibubble dynamics: the drainage of an air film with viscous interfaces. *Phys. Rev. Lett.* **109** (26), 264502.

SETHIAN, J.A. & SMEREKA, P. 2003 Level set methods for fluid interfaces. *Annu. Rev. Fluid Mech.* **35** (1), 341–372.

SHAEBANI, M.R., WYSOCKI, A., WINKLER, R.G., GOMPPER, G. & RIEGER, H. 2020 Computational models for active matter. *Nat. Rev. Phys.* **2** (4), 181–199.

SHAH, A., SAEED, S. & YUAN, L. 2017 An artificial compressibility method for 3D phase-field model and its application to two-phase flows. *Intl. J. Comp. Meth-Sing.* **14** (05), 1750059.

SHAN, X. & CHEN, H. 1993 Lattice Boltzmann model for simulating flows with multiple phases and components. *Phys. Rev. E* **47** (3), 1815–1819.

SHAN, X. & CHEN, H. 1994 Simulation of nonideal gases and liquid-gas phase transitions by the lattice Boltzmann equation. *Phys. Rev. E* **49** (4), 2941–2948.

SHARMA, P., MCCOURT, M., QUATAERT, E. & PARRISH, I.J. 2012 Thermal instability and the feedback regulation of hot haloes in clusters, groups and galaxies. *Mon. Not. R. Astron. Soc.* **420** (4), 3174–3194.

SHAW, R.A. 2003 Particle-turbulence interactions in atmospheric clouds. *Annu. Rev. Fluid Mech.* **35** (1), 183–227.

SHEK, A.C.M. & KUSUMAATMAJA, H. 2022 Spontaneous phase separation of ternary fluid mixtures. *Soft Matter* **18** (31), 5807–5814.

SIGGIA, E.D. 1977 Pseudospin formulation of kinetic Ising models. *Phys. Rev. B* **16** (5), 2319–2320.

SIGGIA, E.D. 1979 Late stages of spinodal decomposition in binary mixtures. *Phys. Rev. A* **20** (2), 595–605.

SINGH, A. & PURI, S. 2015 Phase separation in ternary fluid mixtures: a molecular dynamics study. *Soft Matter* **11** (11), 2213–2219.

SINGH, K. & BART, H.-J. 2015 Passage of a single bubble through a liquid–liquid interface. *Ind. Engng Chem. Res.* **54** (38), 9478–9493.

SINGH, R.K., PERLEKAR, P., MITRA, D. & ROSTI, M.E. 2024 Intermittency in the not-so-smooth elastic turbulence. *Nat. Commun.* **15** (1), 4070.

SINHA, K.P. & THAOKAR, R.M. 2019 A theoretical study on the dynamics of a compound vesicle in shear flow. *Soft Matter* **15** (35), 6994–7017.

SINHABABU, A. & BHATTACHARYA, A. 2022 A pseudo-spectral based efficient volume penalization scheme for Cahn–Hilliard equation in complex geometries. *Math. Comput. Simul.* **199**, 1–24.

SINHABABU, A., BHATTACHARYA, A. & AYYALASOMAYAJULA, S. 2021 An efficient pseudo-spectral based phase field method for dendritic solidification. *Comput. Mater. Sci.* **186**, 109967.

SOB'YANIN, D.N. 2015 Theory of the antibubble collapse. *Phys. Rev. Lett.* **114** (10), 104501.

SOLIGO, G., ROCCON, A. & SOLDATI, A. 2019 Coalescence of surfactant-laden drops by phase field method. *J. Comput. Phys.* **376**, 1292–1311.

STEINBERG, V. 2021 Elastic turbulence: an experimental view on inertialess random flow. *Annu. Rev. Fluid Mech.* **53** (1), 27–58.

STOKES, G.G. 1901 *Mathematical and Physical Papers*, vol. 3. Cambridge University Press.

STONE, H.A. 1994 Dynamics of drop deformation and breakup in viscous fluids. *Annu. Rev. Fluid Mech.* **26** (1), 65–102.

STONE, H. & LEAL, L. 1990 Breakup of concentric double emulsion droplets in linear flows. *J. Fluid Mech.* **211**, 123–156.

SUCHANEK, T., KROY, K. & LOOS, S.A. 2023 Entropy production in the nonreciprocal Cahn–Hilliard model. *Phys. Rev. E* **108** (6), 064610.

SUZUKI, M. & KUBO, R. 1968 Dynamics of the ising model near the critical point. i. *J. Phys. Soc. Japan* **24** (1), 51–60.

TALAT, N., MAVRIČ, B., HATIĆ, V., BAJT, S. & ŠARLER, B. 2018 Phase field simulation of Rayleigh–Taylor instability with a meshless method. *Engng Anal. Bound. Elem.* **87**, 78–89.

TÄUBER, U.C. 2013 *Critical Dynamics: A Field Theory Approach to Equilibrium and Non-Equilibrium Scaling Behavior*. Cambridge University Press.

TEIGEN, K.E., SONG, P., LOWENGRUB, J. & VOIGT, A. 2011 A diffuse-interface method for two-phase flows with soluble surfactants. *J. Comput. Phys.* **230** (2), 375–393.

THOMPSON, C.J. 2015 *Mathematical Statistical Mechanics*. Princeton University Press.

TIAN, C. & CHEN, Y. 2016 Numerical simulations of Kelvin–Helmholtz instability: a two-dimensional parametric study. *Astrophys. J.* **824** (1), 60.

TIMM, K., KUSUMAATMAJA, H., KUZMIN, A., SHARDT, O., SILVA, G. & VIGGEN, E. 2016 *The Lattice Boltzmann Method: Principles and Practice*. Springer International Publishing AG.

TIRIBOCCHI, A., WITTKOWSKI, R., MARENDUZZO, D. & CATES, M.E. 2015 Active model h: scalar active matter in a momentum-conserving fluid. *Phys. Rev. Lett.* **115** (18), 188302.

TONER, J. & TU, Y. 1998 Flocks, herds, and schools: a quantitative theory of flocking. *Phys. Rev. E* **58** (4), 4828–4858.

TONER, J., TU, Y. & RAMASWAMY, S. 2005 Hydrodynamics and phases of flocks. *Ann. Phys.* **318** (1), 170–244.

TÓTH, G.I., ZARIFI, M. & KVAMME, B. 2016 Phase-field theory of multicomponent incompressible Cahn–Hilliard liquids. *Phys. Rev. E* **93** (1), 013126.

TREERATANAPHITAK, T. & ABUKHDEIR, N.M. 2023 Diffuse-interface blended method for imposing physical boundaries in two-fluid flows. *ACS Omega* **8** (17), 15518–15534.

TRYGGVASON, G. 1988 Numerical simulations of the Rayleigh–Taylor instability. *J. Comput. Phys.* **75** (2), 253–282.

TRYGGVASON, G., SCARDOVELLI, R. & ZALESKI, S. 2011 *Direct Numerical Simulations of Gas–liquid Multiphase Flows*. Cambridge University Press.

VALLE, N., TRIAS, F.X. & CASTRO, J. 2020 An energy-preserving level set method for multiphase flows. *J. Comput. Phys.* **400**, 108991.

VAN KAMPEN, N. 2007 *Stochastic Processes in Chemistry and Physics*, 3rd edn. Elsevier.

VEERAPANENI, S.K., YOUNG, Y.-N., VLAHOVSKA, P.M. & BŁAWZDZIEWICZ, J. 2011 Dynamics of a compound vesicle in shear flow. *Phys. Rev. Lett.* **106** (15), 158103.

VELA-MARTÍN, A. & AVILA, M. 2021 Deformation of drops by outer eddies in turbulence. *J. Fluid Mech.* **929**, A38.

VELA-MARTÍN, A. & AVILA, M. 2022 Memoryless drop breakup in turbulence. *Sci. Adv.* **8** (50), eabp9561.

VERMA, M.K. 2004 Statistical theory of magnetohydrodynamic turbulence: recent results. *Phys. Rep.* **401** (5-6), 229–380.

VEY, S. & VOIGT, A. 2007 Amdis: adaptive multidimensional simulations. *Comput. Vis. Sci.* **10** (1), 57–67.

VIOLEAU, D. & ROGERS, B.D. 2016 Smoothed particle hydrodynamics (SPH) for free-surface flows: past, present and future. *J. Hydraul. Res.* **54** (1), 1–26.

VITRY, Y., DORBOLO, S., VERMANT, J. & SCHEID, B. 2019 Controlling the lifetime of antibubbles. *Adv. Colloid Interface* **270**, 73–86.

VOIGT, A. & HOFFMAN, K.-H. 2002 Asymptotic behavior of solutions to the Cahn–Hilliard equation in spherically symmetric domains. *Appl. Anal.* **81** (4), 893–903.

WANG, F., ALTSCHUH, P., RATKE, L., ZHANG, H., SELZER, M. & NESTLER, B. 2019 Progress report on phase separation in polymer solutions. *Adv. Mater.* **31** (26), 1806733.

WANG, Z.-B., CHEN, R., WANG, H., LIAO, Q., ZHU, X. & LI, S.-Z. 2016 An overview of smoothed particle hydrodynamics for simulating multiphase flow. *Appl. Math. Model* **40** (23-24), 9625–9655.

WENSINK, H.H., DUNKEL, J., HEIDENREICH, S., DRESCHER, K., GOLDSTEIN, R.E., LÖWEN, H. & YEOMANS, J.M. 2012 Meso-scale turbulence in living fluids. *Proc. Natl Acad. Sci.* **109** (36), 14308–14313.

WITTKOWSKI, R., TIRIBOCCHI, A., STENHAMMAR, J., ALLEN, R.J., MARENDUZZO, D. & CATES, M.E. 2014 Scalar Φ 4 field theory for active-particle phase separation. *Nat. Commun.* **5** (1), 4351.

WU, H. 2021 A review on the Cahn–Hilliard equation: classical results and recent advances in dynamic boundary conditions. arXiv preprint arXiv: 2112.13812.

YADAV, S.K., MIURA, H. & PANDIT, R. 2022 Statistical properties of three-dimensional Hall magnetohydrodynamics turbulence. *Phys. Fluids* **34** (9), 095135.

YILMAZ, I., DAVIDSON, L., EDIS, F. & SAYGIN, H. 2011 Numerical simulation of Kelvin–Helmholtz instability using an implicit, non-dissipative dns algorithm. *J. Phys.: Conf. Ser.* **318**, 032024.

YOKOI, K. 2007 Efficient implementation of thinc scheme: a simple and practical smoothed VoF algorithm. *J. Comput. Phys.* **226** (2), 1985–2002.

YOU, Z., BASKARAN, A. & MARCHETTI, M. 2020 Nonreciprocity as a generic route to traveling states. *Proc. Natl. Acad. Sci. USA* **117** (33), 19767–19772.

YOUNG, Y.-N., TUFO, H., DUBEY, A. & ROSNER, R. 2001 On the miscible Rayleigh–Taylor instability: two and three dimensions. *J. Fluid Mech.* **447**, 377–408.

YOUNGS, D. 1992 Rayleigh–Taylor instability: numerical simulation and experiment. *Plasma Phys. Control. Fusion* **34** (13), 2071–2076.

YUAN, H.-Z., SHU, C., WANG, Y. & SHU, S. 2018 A simple mass-conserved level set method for simulation of multiphase flows. *Phys. Fluids* **30** (4), 040908.

ZANELLA, R., TEGZE, G., TELLIER, L., ROMAIN, & HENRY, H. 2020 Two- and three-dimensional simulations of Rayleigh–Taylor instabilities using a coupled Cahn–Hilliard/Navier–Stokes model. *Phys. Fluids* **32** (12), 124115.

ZHENG, X., WANG, Z., TRIANTAFYLLOU, M. & KARNIADAKIS, G. 2021 Fluid-structure interactions in a flexible pipe conveying two-phase flow. *Intl J. Multiphase Flow* **141**, 103667.

ZHOU, X., DONG, B. & LI, W. 2020 Phase-field-based LBM analysis of KHI and RTI in wide ranges of density ratio, viscosity ratio, and Reynolds number. *Intl J. Aerospace Engng* **2020**, 1–14.

ZHU, C.-S., MA, F.-L., LEI, P., HAN, D. & FENG, L. 2021 Comparison between level set and phase field method for simulating bubble movement behavior under electric field. *Chin. J. Phys.* **71**, 385–396.

ZIA, R., NAZIR, A., POORTINGA, A.T., VAN, N. & CORNELUS, F. 2022 Advances in antibubble formation and potential applications. *Adv. Colloid Interface* **305**, 102688.

ZINN-JUSTIN, J. 2021 *Quantum Field Theory and Critical Phenomena*, vol. 171. Oxford University Press.

ZOU, J., JI, C., YUAN, B., RUAN, X. & FU, X. 2013 Collapse of an antibubble. *Phys. Rev. E* **87** (6), 061002.